



Dipl.-Ing. Claudia Ramskogler

Surface modification of titanium alloys for orthopaedic implants

DISSERTATION

Submitted to the
Faculty of Mechanical Engineering and Economic Sciences at
Graz University of Technology
In Partial Fulfillment of the Requirements for the Degree of
“Doktor der technischen Wissenschaften”

Institute of Materials Science, Joining and Forming

Graz, April 2018

Supervisor: Univ.-Prof. Dipl.-Ing. Dr. techn. Christof Sommitsch
Dr. techn. Fernando Warchomicka

Reviewer: Univ.-Prof. Dipl.-Ing. Dr. techn. Christof Sommitsch
Assoc. Prof. Dr. med. Annelie-Martina Weinberg

Table of contents

| | |
|---|------------|
| Table of contents | I |
| Preface | IV |
| Acknowledgements | V |
| Abstract | VI |
| Kurzfassung | VII |
| Abbreviations / Symbols | IX |
| 1 Introduction | 1 |
| 2 Literature review | 2 |
| 2.1 Conventional biomaterials for permanent orthopaedic implants..... | 2 |
| 2.1.1 Polymers | 3 |
| 2.1.2 Ceramics | 3 |
| 2.1.3 Metals | 3 |
| 2.1.4 High corrosion and wear resistance..... | 4 |
| 2.1.5 Mechanical properties | 5 |
| 2.2 Titanium alloys for orthopaedic application..... | 6 |
| 2.2.1 Alloying elements and classification of titanium alloys..... | 8 |
| 2.2.2 Processing of titanium alloys..... | 11 |
| 2.2.2.1 Processing route for cp Ti..... | 11 |
| 2.2.2.2 Bimodal processed microstructure in $\alpha+\beta$ alloy | 11 |
| 2.2.2.3 β annealed processed microstructure in metastable β alloy..... | 12 |
| 2.2.3 Phase transformations in titanium alloys..... | 13 |
| 2.2.3.1 Martensitic transformation in α and $\alpha+\beta$ alloys | 13 |
| 2.2.3.2 ω phase formation in metastable β alloys..... | 15 |
| 2.2.3.3 Precipitation of the α phase in metastable β alloys | 16 |
| 2.3 Surface modification technique of metallic biomaterials and its effect on cell viability..... | 18 |
| 2.4 Electron beam technology for surface structuring..... | 21 |
| 2.4.1 Electron beam structuring technique | 23 |
| 2.5 Solidification and microstructure behaviour after EB process..... | 26 |
| 2.6 Objectives | 31 |
| 3 Description of methodology | 32 |
| 3.1 Investigated materials | 32 |
| 3.1.1 α alloy | 32 |
| 3.1.2 $\alpha+\beta$ alloy..... | 34 |
| 3.1.3 Near β alloy | 35 |

| | | |
|----------|--|-----------|
| 3.2 | Electron beam process | 37 |
| 3.2.1 | Electron beam welding machine | 37 |
| 3.2.2 | Electron beam positioning | 38 |
| 3.2.3 | Design of surface geometries | 39 |
| 3.2.4 | EB parameters (bead on plate and structuring) | 39 |
| 3.3 | Dilatometry..... | 42 |
| 3.3.1 | Heat treatments of $\alpha+\beta$ alloy Ti6Al4V | 42 |
| 3.3.2 | Dilatometry and heat treatments of near β titanium alloy Ti15Mo | 42 |
| 3.4 | Metallography..... | 44 |
| 3.4.1 | Sample preparation..... | 44 |
| 3.4.2 | Light optical microscope | 45 |
| 3.4.3 | Scanning electron microscope | 45 |
| 3.4.4 | Electron backscattered diffraction | 46 |
| 3.4.5 | Transmission electron microscope | 46 |
| 3.5 | Hardness | 46 |
| 3.6 | Surface characterization | 46 |
| 3.7 | Cell investigations | 47 |
| 3.7.1 | Cell culture | 47 |
| 3.7.2 | Scanning electron microscope | 47 |
| 4 | Results..... | 49 |
| 4.1 | EB bead on plate..... | 49 |
| 4.1.1 | Modification of MZ (depth and width) after different EB parameter | 49 |
| 4.1.2 | Microstructure investigations of cp TiGr2 after EB bead on plate | 52 |
| 4.1.3 | Microstructure investigations of Ti6Al4V after EB bead on plate..... | 52 |
| 4.1.4 | Microstructure investigations of Ti15Mo after EB bead on plate | 53 |
| 4.2 | EB structuring..... | 53 |
| 4.2.1 | EB parameter combinations | 53 |
| 4.2.2 | Surface roughness measurement | 59 |
| 4.3 | Microstructure evolution after EB structuring process and additional heat and aging treatments | 60 |
| 4.3.1 | Commercial pure TiGr2 | 60 |
| 4.3.2 | Ti6Al4V..... | 61 |
| 4.3.3 | Ti15Mo..... | 65 |
| 4.3.3.1 | Investigation on the base material Ti15Mo | 65 |
| 4.3.3.2 | EB structuring on Ti15Mo..... | 71 |
| 4.4 | Biological response by in vitro investigations..... | 76 |
| 4.4.1 | Cell morphology | 76 |
| 4.4.2 | Distribution of cells | 80 |
| 5 | Discussion | 86 |
| 5.1 | EB process as a structuring technique | 86 |

| | | |
|----------|---|------------|
| 5.2 | Solidification of cp TiGr2, Ti6Al4V and Ti15Mo during EB structuring process and change of the mechanical properties..... | 87 |
| 5.2.1 | Cp TiGr2..... | 87 |
| 5.2.2 | Ti6Al4V..... | 88 |
| 5.2.3 | Ti15Mo..... | 90 |
| 5.3 | Age response and phase evolution of Ti15Mo..... | 91 |
| 5.4 | Surface structure after EB process for biomedical application..... | 95 |
| 5.5 | Biological response on EB structured surfaces..... | 97 |
| 6 | Conclusion..... | 99 |
| 7 | Outlook..... | 101 |
| 8 | Bibliography..... | 104 |

Preface

This PhD thesis is submitted for the degree “Doktor der technischen Wissenschaft” at the Faculty of Mechanical Engineering and Economic Science at Graz University of Technology. Prof. Christof Sommitsch conducted this work at the Institute of Materials Science, Joining and Forming between June 2014 and March 2018. This work was funded by the “Steirische Wirtschaftsförderungsgesellschaft mbH (SFG)” through the project HTI_Tech for Med research program “Oberflächenveränderung von Titanlegierungen zur Verbesserung der Biokompatibilität von Implantaten”.

I declare that I have authored this thesis independently, that I have not used other than the declared sources / resources, and that I have explicitly marked all material which has been quoted either literally, or by content, from the used source.

Claudia Ramskogler

Graz, April 2018

Acknowledgements

I would like to thank the director of the Institute of Materials Science, Joining and Forming, Prof. Christof Sommitsch, for the supervision of this work and for giving me the opportunity to work at the institute.

I owe particular thanks to my second supervisor, Dr. Fernando Warchomicka, for his patience and pressure in the right moments.

Thanks to Prof. Weinberg from the Department of Orthopaedics at Medical University Graz for accepting to read this work, and also for her valuable support during the whole project.

Furthermore, I would like to thank the “Steirische Wirtschaftsförderungsgesellschaft mbH (SFG)” for funding the project through the HTL_Tech for Med research program “Oberflächenveränderung von Titanlegierungen zur Verbesserung der Biokompatibilität von Implantaten”. The Electron Beam equipment is sponsored by the European fond for Regional Development (EFRE), government of Styria and Graz University of Technology.

In addition, thanks to Prof. Boccaccini for giving me the opportunity to work at his institute at the Institute of Biomaterials, Department of Materials Science and Engineering, University of Erlangen-Nürnberg, Germany, and the KMM VIN for funding me throughout this time.

Moreover, I have to say thank you to the people from FELMI and the Institute of Physics of Materials from the Charles University of Prague for their support regarding SEM and TEM investigations.

Furthermore, I am very grateful to my colleagues and members of IMAT, and to all people who supported me throughout this work.

Last but not least, I would like to express my gratitude to my partner, my family and friends for supporting me with encouraging words and deeds throughout my studies.

Danke

Gracias

Mercie

Abstract

Titanium and titanium alloys are standard materials for permanent orthopaedic devices because of their low elastic modulus, high corrosion resistance and excellent biological response. Moreover, the design of particular multi-scale surface topographies on titanium alloys can result in fast osseointegration. This work highlights the use of a promising surface structuring technique by the use of an electron beam (EB) in order to design different surface topographies, and to improve the interaction between implant and biological environment of cp TiGr2, Ti6Al4V and the metastable β titanium Ti15Mo alloys. In addition, the microstructural changes of Ti15Mo due to the melting and fast cooling were deeply investigated to gain a better understanding of the phase transformation kinetics. The biological response was characterized with osteoblastic cells (MC 3T3-E1) after several cultivation times on different surface structures of cp TiGr2, Ti6Al4V and Ti15Mo.

The rapid deflection of the electron beam led to a movement of molten material, which enabled the creation of structures on the surface. Different roughness values were achieved by utilisation of specific process and structure parameters for cp TiGr2, Ti6Al4V and Ti15Mo. The generated surface structures appeared homogeneous and showed no pores or defects.

The in vitro investigations revealed a positive cell behaviour on all structured titanium alloys for each cultivation time. The osteoblastic cells were evenly distributed with a polygonal morphology, and built connections through elongated actin filaments (filopodia). A significant increase of cell spreading area on surface structure with a finer canal shape was found after 48 h cultivation time.

Surface structuring by the EB process led to a change in the microstructure for all investigated titanium alloys. Due to the heat input, the microstructure was distinguished in different zones. Therefore, cp TiGr2 and Ti15Mo were divided into a molten zone and base material, where Ti6Al4V revealed an additional heat affected zone. The development of the microstructure for the base material, Ti15Mo, and the structured material for Ti6Al4V and Ti15Mo, were investigated by different heat treatments and aging temperatures. In Ti15Mo, the heat treatment parameters and the heterogeneities in the element portioning in the molten zone had a strong influence on the amount, distribution and size of ω_{iso} and α plates phases, affecting the hardness values.

Kurzfassung

Titan und seine Legierungen finden aufgrund ihrer hohen Korrosionsbeständigkeit, ausgezeichneten Biokompatibilität, hohen spezifischen Festigkeit und der relativ niedrigen E-Module Anwendung im Bereich der orthopädischen Implantate. Das Interface Implantatmaterial und Gewebe stellt die Schlüsselrolle für die Osteointegration einer Osteosynthese dar. Wobei die Osteointegration in direktem Zusammenhang mit der Oberflächentopographie des Implantatmaterials steht. In der vorliegenden Arbeit wird eine neuartige Oberflächenstrukturierungstechnik mittels Elektronenstrahl (electron beam, EB) auf unterschiedlichen Titanlegierungen (Reintitan (cp) TiGr2, Ti6Al4V und Ti15Mo) durchgeführt. Ziel ist mit unterschiedlichen Oberflächenstrukturierungen die Interaktion zwischen Implantat und Osteozyten und damit den Anbau von Knochen an das Implantat zu verbessern um höchste Stabilität für den Patienten zu erreichen. Des Weiteren wird ein besseres Verständnis für die mikrostrukturellen Veränderungen einer metastabilen β Titanlegierung Ti15Mo erzielt. Die biologische Reaktion wurde nach unterschiedlicher Kultivierungszeit durch die Verwendung von Osteoblastzellen (Zelllinie: MC3T3-E1) auf unterschiedlichen Oberflächenstrukturen (cp TiGr2, Ti6Al4V und Ti15Mo) beurteilt.

Durch die rasche Ablenkung des Elektronenstrahls auf der Materialoberfläche konnten das geschmolzene Material bewegt und Oberflächenstrukturen erzeugt werden. Die Verwendung von unterschiedlichen Parameterkombinationen ermöglichte die Erzeugung von unterschiedlicher Rauheit auf cp TiGr2, Ti6Al4V und Ti15Mo. Die unterschiedlichen Strukturen waren homogen und zeigten weder Poren noch andere Defekte.

Die in vitro Untersuchungen wiesen ein positives Verhalten der Zelle in Bezug auf die strukturierten Titanoberflächen nach. Es konnte eine polygonale Morphologie gezeigt werden, indem die Zellen die typischen langen fadenförmigen Aktinfilamente (Filopodia) produzierten, die mit einander verankert und gleichmäßig verteilt waren. Ein erheblicher Anstieg der Zellausbreitungsfläche wurde nach 48 h auf einer fein strukturierten Oberfläche gemessen.

Die untersuchten Titanlegierungen zeigten nach dem Strukturierungsvorgang mittels Elektronenstrahl eine Veränderung der Mikrostruktur. Durch den Wärmeeintrag kam es zur Ausbildung von unterschiedlichen Bereichen im Material. Cp TiGr2 und Ti15Mo wiesen einen aufgeschmolzenen Bereich und Grundmaterial auf, dagegen zeigte Ti6Al4V einen aufgeschmolzenen Bereich, eine Wärmeeinflusszone und das Grundmaterial. Die Entwicklung der Mikrostruktur für das Grundmaterial von Ti15Mo und des aufgeschmolzenen Bereiches von Ti6Al4V und Ti15Mo wurde unter Einfluss unterschiedlicher Wärmebehandlungen und Auslagerungszeiten untersucht. Ti15Mo zeigte hinsichtlich unterschiedlicher Wärmebehandlungsparameter eine starke

Abhängigkeit in Bezug auf die Anzahl, die Verteilung und die Größe der ω_{iso} Phase und α Platten, was sich wiederum auf die Härte des Materials auswirkte.

Abbreviations / Symbols

| Abbreviation Symbol | Meaning |
|------------------------------|---|
| α | Hexagonal closed packed crystal structure of titanium (hcp) |
| β | Body centred cubic crystal structure of titanium (bcc) |
| ω | Hexagonal closed packed crystal structure of titanium (hcp) |
| $\epsilon_{\text{fracture}}$ | Fracture strain |
| σ_Y | Yield strength |
| AM | Additive manufacturing |
| cp | Commercially pure |
| BM | Base material |
| BSE | Backscattered electrons |
| EBSD | Electron backscattered diffraction |
| EB | Electron beam |
| EBM | Electron beam melting |
| EBW | Electron beam welding |
| EDS | Energy-dispersive X-ray spectroscopy |
| FIB | Focused Ion Beam |
| GROD | Grain reference orientation deviation |
| HAZ | Heat affected zone |
| I_B | Beam current |
| IPF | Inverse pole figure |
| LOM | Light optical microscope |
| LBW | Laser beam welding |
| MZ | Molten zone |
| RT | Room temperature |
| SAD | Selected area diffraction |

| | |
|-------------|----------------------------------|
| SLM | Selective laser melting |
| SEM | Scanning electron microscope |
| SE | Secondary electrons |
| T_{β} | β transus Temperature |
| TEM | Transmission electron microscope |
| U_A | Acceleration voltage |
| UTS | Ultimate tensile strength |

1 Introduction

Since the early 1960s when the first hip replacement was done, new materials and complex implant designs have been investigated [1], some of them with successful performance. On the other hand, the rate of failure and loss of implants are still undesirably high, and improvements in this field are urgently required. These improvements shall decrease the morbidity of the patients, and additionally reduce losses in the health care system. Therefore, the elastic modulus of the material and a fast integration of the implant with the bone is essential. The effect of surface topography at the micrometre scale on bone integration and cell behaviour was already shown in previous studies [2], [3].

This work concerns a novel surface structuring technique by an electron beam (EB), in order to improve the interaction between implant and biological environment of titanium alloys, and also to gain an understanding of microstructural changes of new biomaterials (e.g. metastable β titanium alloy). The Chapter 2 literature review gives an overview of conventional biomaterials for permanent implants, and a more detailed description of titanium alloys to establish a basic understanding. Furthermore, the electron beam (EB) process and the surface modification with this technique are explained. At the end of the literature review, the aim of this work is described. The Chapter 3 description of the methodology depicts the characterization of the investigated titanium alloys (cp TiGr2, Ti6Al4V and Ti15Mo) and describe the experimental work. In the fourth chapter, the most relevant results for all investigated titanium alloys and their behaviour after EB structuring are shown and described. Therefore, this chapter is subdivided into: EB bead on plates, EB structuring, microstructure evolution after EB structuring process and additional heat treatments, and biological response by in vitro investigations. The Chapter 6 discussion section is subdivided into the following sub-sections: parameter optimization for EB structuring, microstructure evolution of cp TiGr2, Ti6Al4V and Ti15Mo after EB structuring, age response on hardness and phase evolution of Ti15Mo and EB structured Ti15Mo, surface structuring after EB process for biomedical application, and biological response on EB structured surfaces.

In the Chapter 7 conclusions, the work is summarized and a final statement of this work is given. The Chapter 8 outlook shows potential further research investigations, based on preliminary results obtained during the development of this work.

2 Literature review

This chapter introduces an overview and relevant literature related to the study of biomaterials, titanium alloys and surface modification techniques for orthopaedic application.

2.1 Conventional biomaterials for permanent orthopaedic implants

Williams [4] defined biomaterials as “*a nonviable material in a medical device, intended to interact with biological systems*”. Hence, “biomaterial” is a generic term that covers a broad field of different applications, different materials as well as different requirement profiles. No matter of material type or the application, the direct interaction between the biomaterial and the biological system is the common thread.

The three generations of biomaterials, as illustrated in Figure 1, should be interpreted as conceptual and not chronological. Each generation represents an evolution of the properties and requirements of the involved material. Therefore, the first-generation biomaterials achieve the requirements for the material properties and biological properties, such as foreign body reaction. The second generation is defined by biomaterials with the ability to interact with the biological environment, which undergo a progressive degradation while new tissue regenerates. The third, and last, generation of biomaterials are able to stimulate cellular response at the molecular level, where the bioactivity and degradation are combined (e.g. scaffolds and tissue engineering) [5].

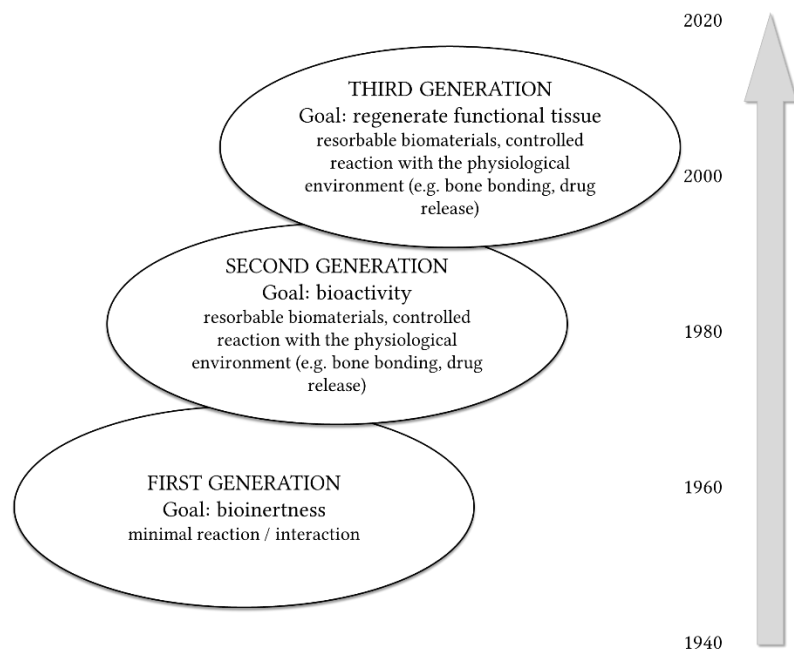


Figure 1. Evolution of biomaterial adapted from [6].

The term “biocompatibility” has only a qualitative delineation of how the body environment interacts with the biomaterial, with some expectations of certain

implantation site and purpose [7]. Williams [4] defined the biocompatibility as “*the ability of a material to perform with an appropriate host response in a specific application*”.

Biomaterials of orthopaedic implants are necessary to replace, or repair, surgical human bone provoked by diseases, trauma or degeneration. Implants used to replace diseased bone must remain in the body permanently [8]; to facilitate healing, implants remain in the body only temporarily, until completion of the healing process [9]. Selection of biomaterials used for orthopaedic implants that remain in the body permanently has to deal with several considerations that can be grouped as material, structural design, manufacturing, regulatory and patient-related factors [10]. In general, biomaterials can be grouped into three major categories: (1) polymers, (2) ceramics and (3) metals [11].

2.1.1 Polymers

Polymers are the largest group of materials used in medicine. Polymers can be natural (e.g. cellulose) or synthetic (e.g. silicone), and used for soft and hard tissue application. They are also used for drug delivery applications (coatings). For example: ultra-high molecular weight polyethylene (UHMWPE) or poly(etheretherketone) are used for orthopaedic application. They offer good bioactivity and biocompatibility, but, due to their insufficient mechanical properties and their long-term failure associated with environmental aging mechanism and stress cracking, they cannot be considered as suitable material in orthopaedic application [7], [12].

2.1.2 Ceramics

Ceramics, glasses and glass ceramics as biomaterial include a wide range of inorganic /non-metallic compositions. The applications of bioglasses and glass ceramics include acting as bone substitutes and bioactive coatings on metallic implants. Coatings are used to promote rapid bone growth, and are not used directly as load bearing elements. The most popular ceramics are alumina (Al_2O_3) and zirconia (ZrO_2), usually used as femoral heads for hip replacement and wear plates for knee replacement. The main concerns related to ceramic orthopaedic implants are the limited lifetime due to inferior fracture toughness and their brittle nature [5], [7], [12].

2.1.3 Metals

Metallic biomaterials are mostly used as a permanent substitution, or to repair seriously damaged human bones. Metals like stainless steels, cobalt base alloys, titanium and titanium alloys are used. Because of its lower costs, availability, accepted biocompatibility, excellent fabrication properties and toughness, stainless steel remains popular for implant applications. In general, cobalt-base alloys are superior in terms of

resistance to corrosion, wear and fatigue compared to stainless steels. However, due to corrosion of cobalt-based alloys and stainless steel alloys in the hostile body environment, ions or particles of Ni, Co and Cr can be released. The biological toxicity of these elements have been reviewed [13], [14]. Titanium and its alloys are suitable for biomedical implants due to their excellent biocompatibility associated with distinguished corrosion resistance in the hostile human environment, high strength and low density (compared to other metallic implant materials) [15]. Metallic implant material properties must possess key properties, including high wear resistance, suitable mechanical properties in air and simulate body fluid [12], [16]. The materials must also possess excellent biocompatibility [12], high corrosion resistance [11] and a favourable platform to provide new bone formation [13].

2.1.4 High corrosion and wear resistance

No matter which materials are used for permanent replacement or joint implants, a low wear and corrosion resistance are inevitable problems in the human body environment. The release of non-compatible metal ions by the implant material can cause inflammation or allergic reactions in the human body. Corrosion resistance for permanent implants determines the long-term success in human body fluids. The human body fluid consists mainly of proteins and chloride ions, and has a nearly neutral pH value (at 37 °C 7.2 – 7.4). The presently used metallic materials (stainless steel, cobalt-based alloys and titanium alloys) are subject to corrosion, although they form a passive surface film. Nevertheless, due to inflammatory cell secretions (caused by injury or surgery), the pH of human fluids can fall up to 3-4. Due to the low pH value, combined with unstable ionic strength or ion deposition, the human body presents an aggressive environment for any implant material. Therefore, corrosion damage can include: (1) crevice attack, which refers to shielded sites and the presence of chlorides (e.g. screw/plate interface), (2) pitting corrosion, which appears predominant in oxygen and acidic environments, such as the oral cavity and (3) fretting corrosion, which can occur due to relative small-scale motion between implant components and is induced by cycle load, where fracture and abrasion of the protective oxide layers are generated. The fretting in combination with the wear process causes the generation of wear debris, which can cause severe adverse responses, such as inflammation or immunological disease reactions [17].

The choice of material type, or surface treatment, is not only determined by the tribological properties, also by the type of joints. Therefore, two types of mobile joints can be categorized: (1) congruent, where joints are close to the opposed bone and the stress is distributed evenly (e.g. hip, as shown in Figure 2(a)), and (2) incongruent, where joints are not close to the opposed bone, and the stress is highly concentrated (e.g. ankle, as shown in Figure 2(b)). For incongruent joints, the brittle and hard ceramic materials

cannot stand such high stress impact, so metallic materials are preferred in these case [13], [14].

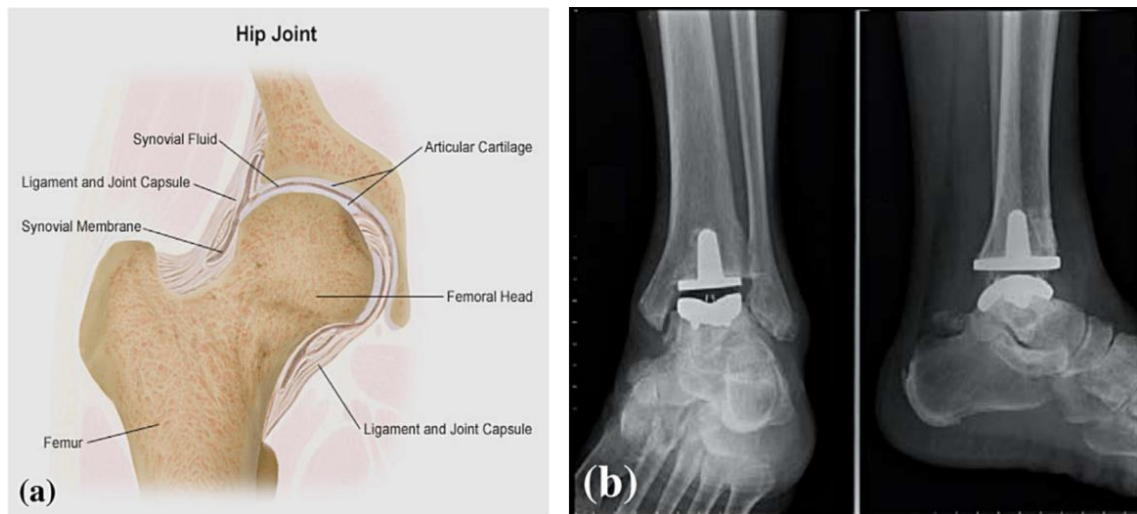


Figure 2. Type of joints in human body a) congruent joint and b) artificial incongruent joint [14].

Several surface treatment techniques have been investigated to overcome the poor wear resistance behaviour. Celik et al. [18] reported an improved wear resistance of plasma oxidized ultrafine grained TiGr2, and attributed it to the formation of a hard and adherent rutile TiO_2 layer, compared to untreated, anodized, thermal and micro arc oxidized samples. The formation of the rutile TiO_2 layer was also performed on Ti6Al4V/10% TiC composites (TMCs) by thermal oxidation to increase the wear resistance [19]. Laser surface melting of Ti6Al4V resulted in the lowest in vitro wear rate due to the formation of an acicular martensite layer on the top surface, where the hardness increased to ~ 420 HV0.3, as compared to ~ 360 HV0.3 for the base material [20].

2.1.5 Mechanical properties

The mechanical properties for metallic biomaterials must match the mechanical performance of the replaced bone. Young's modulus and tensile characteristics are, in general, important for metallic biomaterials. It is desirable that the Young's modulus of the implant material be similar to bone to avoid the "stress-shielding effect". The "stress-shielding effect" is the biological response of atrophy, particularly around the implant caused by the takeover of the total load by the implant material, due to its higher Young's modulus compared to the bone. Therefore, stress concentration and bone loss can lead to cracking of plates or screw pull out. Table 1 shows the comparison of Young's modulus and ultimate tensile strength (UTS) of metallic implant materials compared to cortical bone.

Table 1. Young's modulus and Ultimate tensile strength of metallic implant materials compared to cortical bone [14], [21].

| Materials | Young's modulus [GPa] | Ultimate tensile strength [MPa] |
|----------------------|-----------------------|---------------------------------|
| CoCrMo alloys | 240 | 900 – 1540 |
| 316L stainless steel | 200 | 540 – 1000 |
| Ti alloys | 78 – 125 | 900 |
| Cortical bone | 10 – 30 | 130 – 150 |

The ability to bear loads, to undergo plastic deformation and a Young's modulus similar to bone, are insufficient to fulfil the required mechanical properties. After implantation, the implants suffer from fatigue due to cyclic loading (e.g. hip joints experience several thousand steps a day at a rate of 1 Hz). Therefore, another aspect to enable the reliability for implants after implantation is determined by the fatigue strength [14], [16]. Table 2 summarizes the advantages and disadvantages of the main metallic implant materials.

Table 2. Advantages and disadvantages of the main orthopaedic metallic implant materials, adapted from [22].

| | Stainless steel | Co base alloys | Ti and its alloys |
|----------------|---|---|---|
| Advantages | <ul style="list-style-type: none"> • Cost, availability • Processing | <ul style="list-style-type: none"> • Wear resistance • Corrosion resistance • Fatigue strength | <ul style="list-style-type: none"> • Biocompatibility • Corrosion resistance • Minimum modulus • Fatigue strength |
| Dis-advantages | <ul style="list-style-type: none"> • Long term behaviour • High modulus | <ul style="list-style-type: none"> • High modulus • Bio-compatibility | <ul style="list-style-type: none"> • Poor wear resistance • Low shear strength |

2.2 Titanium alloys for orthopaedic application

In England in 1791, William Gregor first identified a new metallic element. Four years later and inspired from the name of the Titans of Greek mythology, the Berlin chemist Klapproth named this metallic element Titanium. Titanium is found in many different mineral deposits: ilmenite (FeTiO_3), rutile (TiO_2), titanomagnetite, anatase and brookite. Until the middle of 20th century, the production of ductile, high purity titanium was difficult due to the high reactivity of titanium with oxygen and nitrogen. In 1938, Kroll

developed a process, which involves the reduction of titanium tetrachloride with magnesium in an inert-gas atmosphere. The Kroll process remained essentially unchanged, and is still the dominant method for titanium production. The first satisfactory results with titanium as implants were already achieved in 1940. In 1952, the orthopaedic surgeon Per Ingvar Branemark discovered the osseointegration by the use of titanium for bony tissue implants. This was the major breakthrough in the use of titanium for implant materials [14], [15], [23].

Titanium is an allotropic element, which means it can exist in more than one crystallographic form. Titanium and most of its alloys can basically exist in two allotropic modifications: slightly distorted hexagonal close-packed (hcp), also referred to as “ α ” phase in titanium, and body centred cubic crystal structure (bcc) “ β ” phase, as shown in Figure 3 [23].

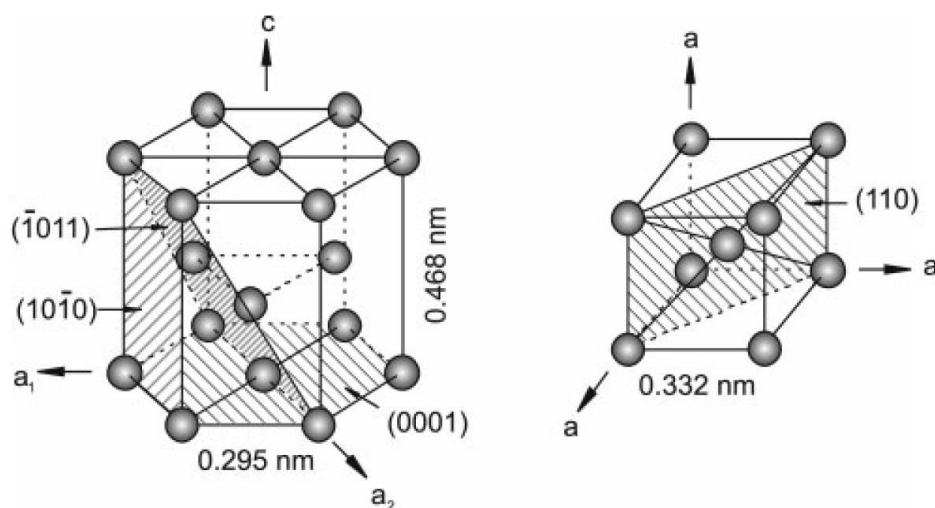


Figure 3. Unit cell of the α phase and β phase [24].

The transformation from one crystal structure into another occurs at a transus temperature, also known as β -transus (T_β), which is defined as the lowest equilibrium temperature where the material consists of 100% β phase. During the transformation process, the (110) planes of the β phase (bcc) transform into a (0001) alpha phase (hcp, as schematically shown in Figure 4). The T_β temperature can be altered, and is dependent on the purity of the materials (interstitial elements) and on the presence of alloying elements.

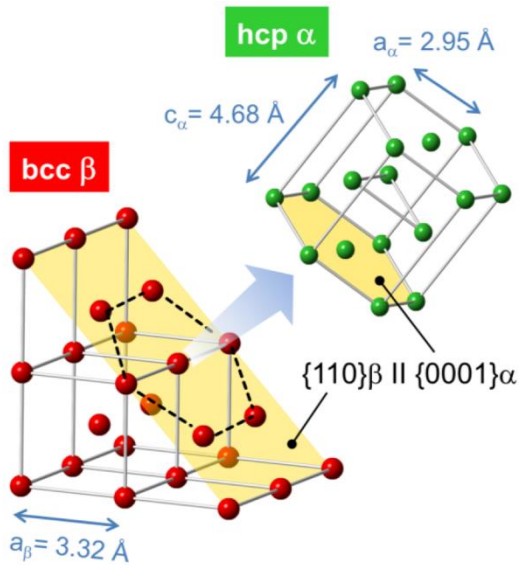


Figure 4. Lattice correspondence between the unit cells of hcp α phase and bcc β phase (parameters belong to pure titanium at room temperature for α and at 900 °C for β phase) [25].

2.2.1 Alloying elements and classification of titanium alloys

With respect to the effect of alloying elements in the solubility of α and β phases, the alloying elements are classified as: α -stabilizer, β -stabilizer, and neutral elements, as shown in Figure 5. They are classified according to whether they decrease, or increase, the T_{β} .

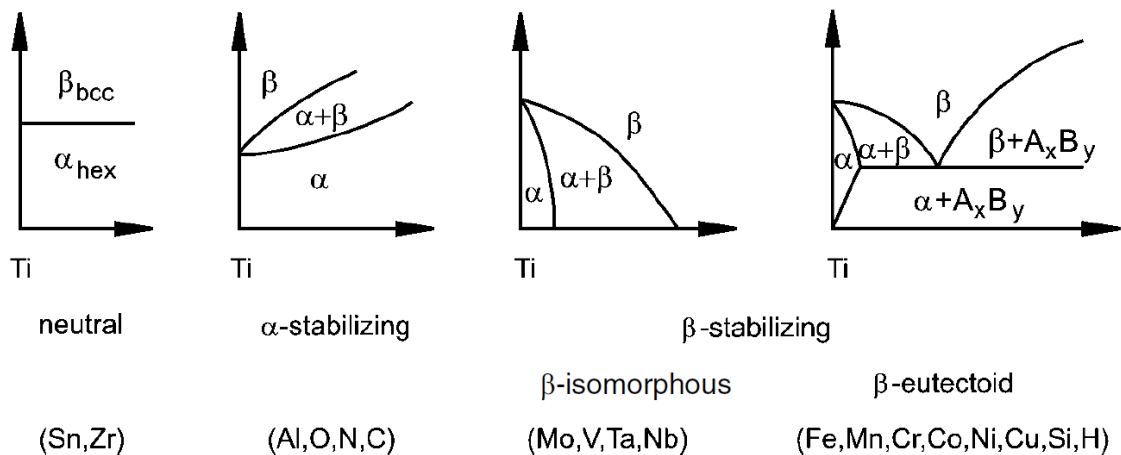


Figure 5. Schematically representation of the influence of alloying elements on the T_{β} and phase diagrams of titanium alloys [24].

Neutral elements (Sn, Zr and Hf) have only a minor influence on the T_{β} .

The α stabilizing elements extend the α phase field to a higher temperature, i.e. they increase T_{β} . Al is the most used alloying element because it stabilizes the α phase field to higher temperatures, and has a large solubility in the α and β phases. In terms of

biocompatibility, Al is acutely toxic to the human body in very high doses. The interstitial elements O, N and C are usual elements in this group. The biological performance of O, C, H and N in the human body are the building blocks of water and proteins. They consist of approximately 96 % of their weight in the body [23], [24], [14].

The influence of α stabilizing elements like Al, Sn, Zr, O, C and N are included and established in the following equation:

$$\text{Al eq.} = \text{wt. \% Al} + 0.33 \text{ wt. \% Sn} + 0.17 \text{ wt. \% Zr} + 10 \text{ wt. \% [O + C + 2N]} \quad (1)$$

To avoid embrittlement by precipitation of Ti_3Al , the Al eq. content is limited to 9 wt% [23], [24].

β stabilizing elements are subdivided in β isomorphous and β eutectoid forming elements, depending on their influence on the binary phase diagram, as shown in Figure 5. They shift the β phase field to lower temperatures, i.e. they decrease the T_β . The elements V, Mo, Nb and Ta are the most important β isomorphous alloying elements due to their high solubility in titanium. Mo is an essential trace element in the human body, and important for a cell metabolism and a number of enzymes. Vanadium plays a less defined role in the human body, but can have positive and negative effects on the cellular response. Nevertheless, acute toxicity of Mo, V and Nb have not been reported yet, but direct ingestion or inhalation of these elements, its oxides and compounds (niobates, niobium chloride) should be avoided. In contrast, Ta shows excellent biocompatibility. The most important β eutectic alloying elements are Fe, Mn, Cr, Co Ni, Cu, Si and H, and to avoid embrittlement H is restricted to $\sim 125 - 150$ ppm (biological response is explained in α stabilizing elements). Concerning their biological performance Fe, Mn, Cr, Co Ni, Cu are trace elements and essential in the human body. Nonetheless, a high exposure level of these elements, or their compounds, can cause allergy related dermatitis and adverse serious health problems [14], [23], [24].

The Mo-equivalent describes the stability of the β phase by including the influence of the individual β stabilizing elements like Mo, Ta, Nb, W, etc. The calculation is as follows:

$$\text{Mo eq.} = \text{wt. \% Mo} + 0.2 \text{ wt. \% Ta} + 0.28 \text{ wt. \% Nb} + 0.4 \text{ wt. \% W} + 0.67 \text{ wt. \% V} + 1.25 \text{ wt. \% Cr} + 1.25 \text{ wt. \% Ni} + 1.7 \text{ wt. \% Mn} + 1.7 \text{ wt. \% Co} + 2.5 \text{ wt. \% Fe} \quad (2)$$

To require a stable β phase at RT, the Mo equivalent has to be at least ≥ 10 wt% [23], [24].

Titanium itself is not found and does not play any essential role in the human body, and does not show any toxic reactions even in large doses [14].

Titanium alloys are classified on the basis of the amount of α or β stabilising elements, and their subsequent position in the β isomorphous phase diagram, as shown in Figure 6.

Therefore, they are categorized in α alloys, near α alloys, $\alpha+\beta$ alloys, metastable β alloys and stable β alloys.

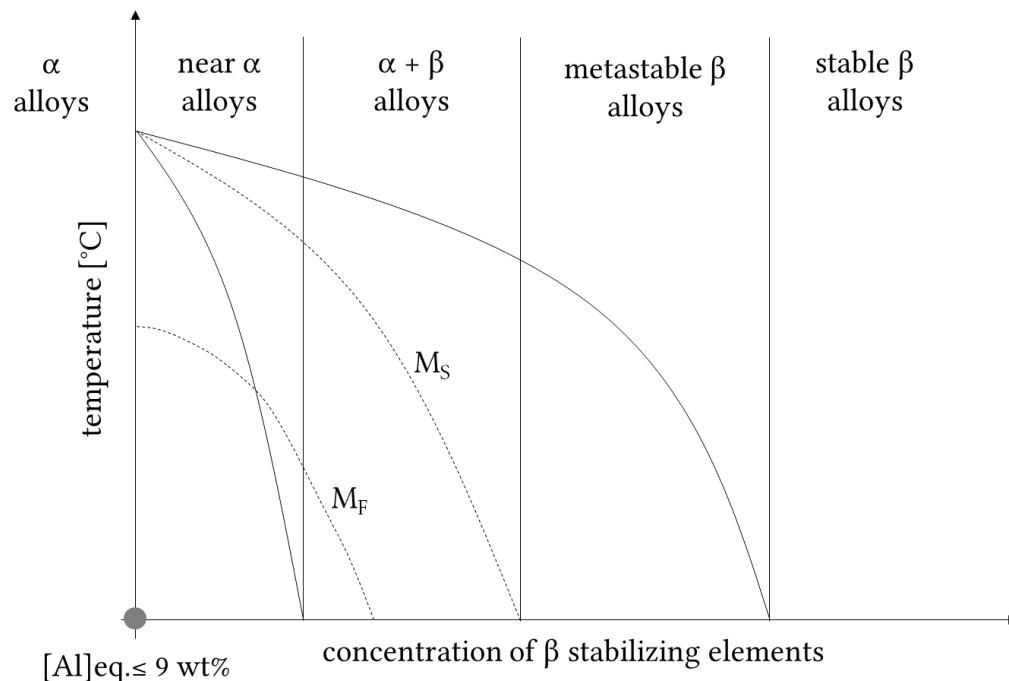


Figure 6. The classification of titanium alloys in a β isomorphous phase diagram (pseudo-binary section). [Adapted from Ref [15] page 224.]

The α alloy includes four grades of commercially pure (cp) Ti alloys from 1 to 4 (O varies between 0.18 – 0.40 wt%) and Ti alloys which contain only α stabilizing or neutral elements. Cp Ti alloys are used for biomedical applications that include maxillofacial and craniofacial implants, screws and staples for spinal surgery, dental implants, pacemaker cases, housing for ventricular-assist devices and implantable infusion drug pumps. If minor fractions of β stabilizing elements are present (up to 2 wt%), and form less than 10 vol.% of β phase, they are denoted as *near α alloy*. The α (except cp Ti alloys) and near α alloys have not been used for biomedical application due to their low ambient temperature strength, no strengthening by heat treatments, poor forge ability and narrow forging temperature compared to $\alpha+\beta$ and β alloys [15], [24].

The most widely used alloy group is the $\alpha+\beta$ alloys. The volume fraction of β phase ranges from 5 to 40 % at room temperature. The microstructure of these alloys can occur in different forms, ranging from acicular to equiaxed or combinations of both. One can change mechanical properties by applying different thermal and thermomechanical treatments. Non-equilibrium phases, such as martensite or metastable beta, can occur in $\alpha+\beta$ alloys. The most popular $\alpha+\beta$ alloy is by far Ti6Al4V, as around 50% of the total titanium production is of this composition for biomedical implants. They are used mainly for hip and knee replacements [15], [24].

In *metastable β alloys*, the β phase contains more than 25 vol.%. Therefore, metastable β alloys contain 10 -15 wt% of β stabilizers, which also suppresses the non-equilibrium martensitic phase and forms either a metastable, or stable β phase, at room temperature. The mechanical properties, i.e. microstructure, are strongly related to thermal and thermomechanical treatments. For biomedical implant applications, the metastable β alloys offer enhanced biocompatibility (alloying elements exhibit good or excellent biocompatibility) and a lower elastic modulus (compared to $\alpha+\beta$ alloy) mainly used for surgical implants. *Stable β alloys* have no possibility of precipitation hardening, and therefore have rather poor mechanical properties. They have no commercial or practical use. Therefore, metastable β alloys are also known as β alloys [15], [24], [26].

2.2.2 Processing of titanium alloys

The properties of titanium alloys are, in general, based on the chemical composition and the microstructure. The chemical composition regulates the volume fraction of phases, as explained in section 2.2.1 (page 8). Therefore, the balance of their individual properties and the microstructure define the arrangement of phases in the alloy. The microstructure of α , $\alpha+\beta$ and metastable β alloys can be developed by thermomechanical processing routes. The processing route to generate the microstructure of cp titanium, bimodal $\alpha+\beta$ and metastable β alloy will be discussed.

2.2.2.1 Processing route for cp Ti

A typical processing route for cp Ti alloys is shown in Figure 7, and basically consists of: (1) homogenization, (2) deformation and (3) annealing. Low solute elements in cp Ti require a short homogenization time. The deformation degree defines the texture intensity and grain size of the microstructure. In the last step, the annealing determines the α grain size. The microstructure of cp Ti grade 2 consists of α grains.

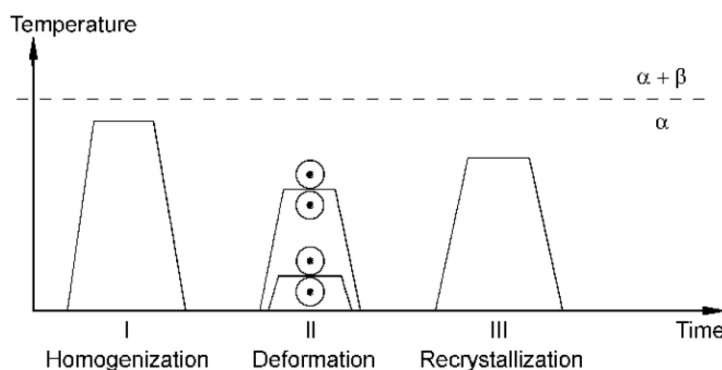


Figure 7. Schematic illustration of a process routine for cp Ti [23].

2.2.2.2 Bimodal processed microstructure in $\alpha+\beta$ alloy

Three different types of microstructure can be obtained by changing the thermomechanical process routine in $\alpha+\beta$ alloys: fully lamellar, fully equiaxed, bimodal

(duplex) and a less relevant mill-annealed structure. The bimodal structure will further be discussed. The process routine to obtain a bimodal structure is divided into four steps, as shown in Figure 8: (1) homogenization above T_{β} , i.e. the β phase field, (2) deformation below T_{β} , i.e. the $\alpha+\beta$ phase field, (3) recrystallization below T_{β} , i.e. the $\alpha+\beta$ field and (4) stress relief or final aging. The homogenization will be carried out in the β phase field. The cooling rate from the homogenization temperature is a critical parameter in the process route, where the width of the α lamellae is determined. Subsequently, the α lamellae microstructure is deformed plastically in $\alpha+\beta$ phase field to generate the crystallographic texture and on the other hand, to guarantee a high stored energy after the deformation (dislocations). The high stored energy should be high enough to obtain a complete recrystallization in the last step. The annealing temperature in the last step also defines the grain size and the cooling rate the width of the α lamellae.

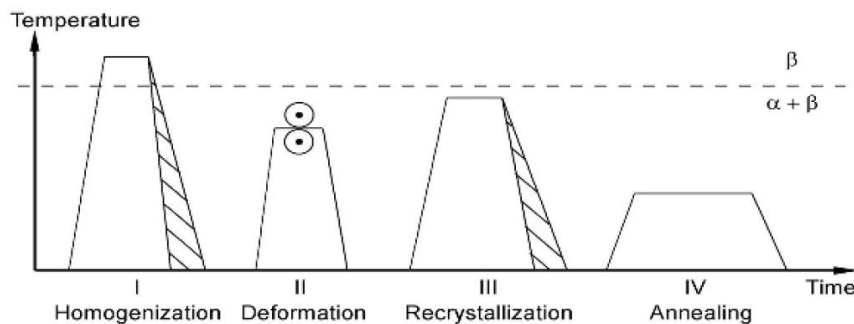


Figure 8. Schematic illustration of a process routine of $\alpha+\beta$ (e.g. Ti6Al4V) alloy for a bimodal microstructure [23].

2.2.2.3 β annealed processed microstructure in metastable β alloy

The basic processing route to generate a β annealed microstructure with homogeneously distributed secondary α (α_s) plates of a metastable β titanium alloy, is shown in Figure 9. The thermomechanical treatments consist of different steps: (1) homogenization above T_{β} , i.e. in the β phase field, (2) deformation below or above T_{β} , i.e. in the $\alpha+\beta$ phase field, (3) recrystallization above T_{β} , i.e. in the β phase field, and (4) aging. The cooling rate from the homogenization temperature is a critical parameter due to the formation of a α film-like precipitation at the grain boundaries, which is detrimental to the mechanical properties. The deformation can be carried out either below, or above, the T_{β} , whereby the deformation below the T_{β} creates small β grain size, and the deformation above the T_{β} leads to the opposite during the next recrystallization process. The additional aging treatment (typically 500 °C – 600 °C) results in a matrix of β grains with homogeneously distributed fine α_s plates.

The precipitation of the detrimental α film at the homogenization step can be suppressed by rapid cooling from the homogenization temperature, or adding a thermomechanical processing to break up the α grain boundary film [23], [24].

To avoid fine intergranular α_s plates, and to generate retained β in a metastable state, the processing route needs to be aborted after the recrystallization step, and a fast cooling from the recrystallization temperature needs to be carried out [23].

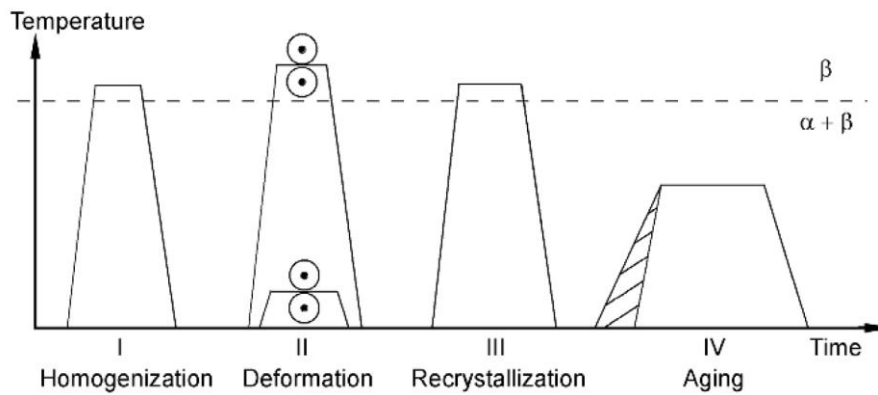


Figure 9. Schematic illustration of a process routine of a β alloy (e.g. Ti15Mo) for β processed microstructure [23].

2.2.3 Phase transformations in titanium alloys

Many phase transformations occur in titanium and titanium alloys during thermal and thermomechanical treatments. This literature review will concentrate on: (1) $\beta \rightarrow \alpha'$ transformation in α and $\alpha + \beta$ titanium alloys, (2) $\beta \rightarrow \omega$ transformation in metastable β titanium alloys, and (3) $\beta \rightarrow \alpha$ transformation in metastable β titanium alloys.

2.2.3.1 Martensitic transformation in α and $\alpha + \beta$ alloys

For adequately fast cooling rates from bcc β phase to hcp α phase, the transformation is diffusionless and martensitic. The displacement transformation of martensite is initiated by the formation of nuclei of the product phase. The growth of these nuclei occurs by the movement of a shear front at a speed that reaches the speed of sound in the material. This transformation of titanium alloys, with a low amount of β stabilizing elements, requires the shear of the $\{110\}$ β planes to the basal planes of the hcp α' martensite. The orientation relationship between the parent bcc β phase and hcp α' phase has been determined as [27]:

$$(011)_{\beta} \parallel (0002)_{\alpha'}$$

$$\langle 11\bar{1} \rangle_{\beta} \parallel \langle 11\bar{2}0 \rangle_{\alpha'}$$

For titanium alloys with a high amount of β stabilizing elements, the orientation relation is incomplete; the hexagonal symmetry is not reached, and an orthorhombic α'' martensite is formed. Figure 10 shows the description of the lattice correspondence of the martensitic transformation from the parent bcc β phase to the hexagonal or orthorhombic martensite.

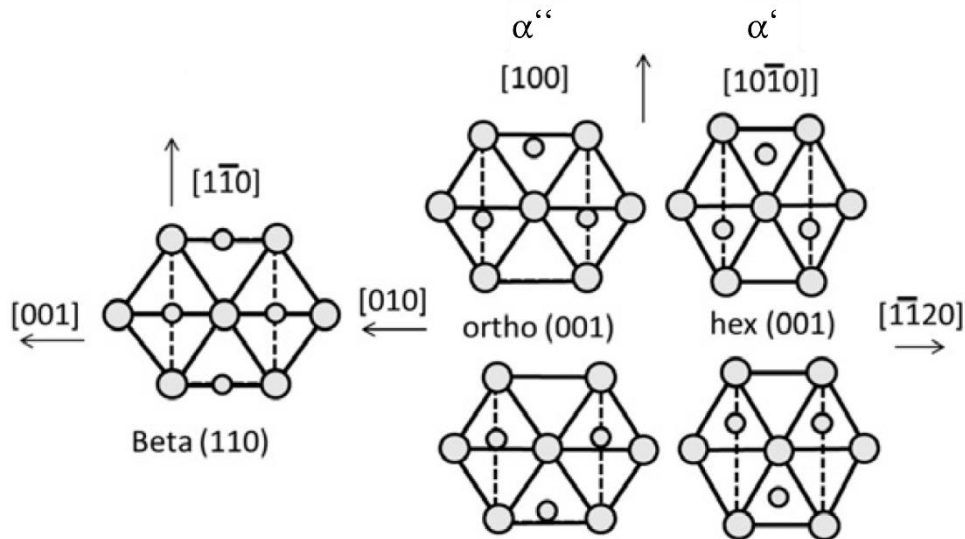


Figure 10. Lattice correspondence from bcc β phase to orthorhombic (α'') or hexagonal (α') martensite projected perpendicular to $[110]_{\beta}$ [28].

Two martensite morphologies can be observed: (1) massive martensite and (2) acicular martensite. The massive martensite is detected in alloys with a low amount of alloying elements, and titanium alloys with a high martensitic transformation temperature, e.g. pure titanium. The microstructure consists of large and irregular colonies (50 -100 μm) with fine martensite laths (0.1 – 1 μm), where they all have similar crystal orientation. In contrast, the acicular martensite is observed in alloys with a higher amount of alloying elements, i.e. titanium alloys with low martensitic transformation temperature. The microstructure of acicular martensite presents individual martensite laths (e.g. plates), each with different crystal orientation [23], [27], [28], [29].

Figure 11 (a) displays the continuous cooling diagram for Ti4Al4V, with a T_{β} of 1050 $^{\circ}\text{C}$ and a martensitic start temperature (M_s) of 575 $^{\circ}\text{C}$. For a cooling rate between 525 $^{\circ}\text{C}/\text{s}$ and 410 $^{\circ}\text{C}/\text{s}$, acicular martensite is formed, and for lower cooling rates between 410 $^{\circ}\text{C}/\text{s}$ and 20 $^{\circ}\text{C}/\text{s}$, massive α (α_m) [29]. The continuous cooling transformation curve for grade-4 cp titanium in Figure 11 (b) shows three different transformation modes, depending on the cooling rate [30]. Therefore, lath type martensite is observed after cooling rates of around 1200 $^{\circ}\text{C}$.

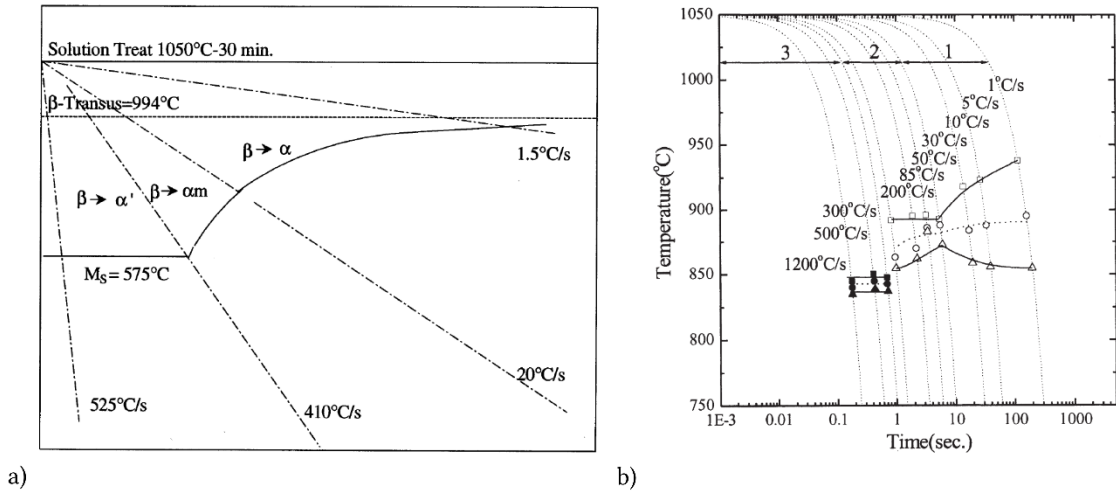


Figure 11. a) Schematic continuous cooling diagram for Ti6Al4V [29] b) continuous cooling transformation curve for grade-4 cp Ti. 1: platelike alpha + acicular alpha, 2: acicular alpha + massive alpha, and 3: lath type martensite. The filled circles represents the M_S temperature [30].

2.2.3.2 ω phase formation in metastable β alloys

The non-equilibrium ω phase appears in Ti alloys which contain a required level of β stabilizing elements. The unit cell of the ω phase has either a trigonal structure in low concentrated alloys, or hexagonal structure in highly concentrated alloys. In metastable β titanium alloys, it has been indicated that the ω phase can be obtained by: (1) fast quenching from the parent β phase (ω_{ath}) and (2) during thermal aging decomposition of β phase (ω_{iso}). The lattice correspondence between the parent bcc β phase is valid for both the ω_{ath} and ω_{iso} phase. Therefore, the orientation relationship between the parent bcc β phase and the ω_{ath} and ω_{iso} can be determined by [27]:

$$\{111\}_{\beta} \parallel (0001)_{\omega}$$

$$\langle \bar{1}\bar{1}0 \rangle_{\beta} \parallel \langle \bar{1}\bar{2}10 \rangle_{\omega}$$

The sketch in Figure 12 shows the stacking sequence ABCABC... for the $(222)_{\beta}$ planes of the parent bcc β phase. The most common model to describe the formation of ω phase is based on the collapse of planes in the $(222)_{\beta}$ (layers 1 and 2 in Figure 12) to the intermediate position (layer 1.5 in Figure 12). The next planes remain unaffected (layers 0 and 3 in Figure 12), and the following pair of planes collapse, and so on. If the collapse is complete, a six fold rotation symmetry arises around the $[111]_{\beta}$ direction, along which a lattice collapse occurs, and a hexagonal ω phase is obtained. An incomplete collapse generates a trigonal structure. During the transformation of ω phase, the composition of the parent bcc matrix is retained. Because of the $[111]_{\beta}$ direction, the ω phase has four possible crystallographic variants in a parent bcc β crystal.

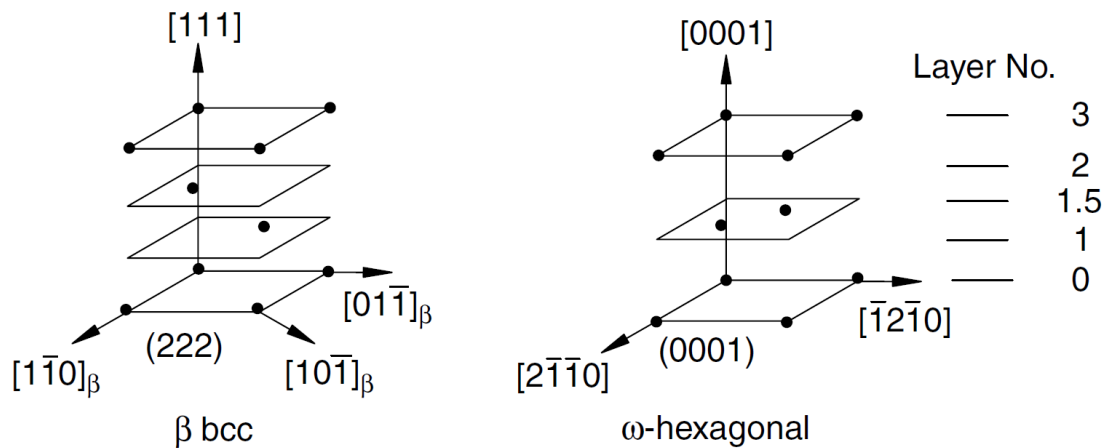


Figure 12. Arrangement of the planar atomic planes of the bcc lattice $\{222\}_{\beta}$ and the hcp lattice $(0001)_{\omega}$ [27].

The formation of ω_{ath} occurs in metastable β titanium alloys during quenching from the parent β phase. This shuffle transformation does not involve any macroscopic shape strain. The athermal nature of transformation of ω_{ath} has been established through ultrahigh quenching rates. Subsequently, it can be suggested that the transformation occurs without any thermal activation. Additional evidence of its athermal nature is the reversible transformation. The ω particles formed during quenching have an ellipsoidal shape, and no plate-like morphology or surface relief results, which would be typical for a martensitic transformation. Therefore, the athermal transformation is not categorized as a martensitic transformation, even though the transformation was mentioned as athermal with a composition independent character [27].

The ω_{iso} formation is diffusion controlled, and therefore thermal and/or mechanical (pressure, deformation) activations are necessary for its growth. The exact transformation temperatures vary from one system to another. The lattice collapse mechanism to form ω_{iso} precludes a thermally activated compositional partitioning process in the parent β phase. As a consequence, the ω_{ath} phase could be replaced and serve as nucleation sites for the formation of ω_{iso} . The amount and volume fraction of ω_{iso} phase are strongly related to the heating rate, isothermal holding time and the chemical composition of the β phase. The morphology of the ω particles depends on the ω/β (precipitate/matrix) misfit. For systems with a low misfit ($< 0.5\%$), e.g. Ti-Mo [31], ω can precipitate with an ellipsoidal morphology. For a large misfit system ($>1\%$), e.g. Ti-Fe or Ti-V [23] [27], the ω phase precipitates with a cuboidal shape [32].

2.2.3.3 Precipitation of the α phase in metastable β alloys

There are typically two classifications for α phase precipitation in a retained β matrix (whole β phase can be retained upon fast cooling to room temperature): (1) continuous cooling from the β phase field and (2) ω assisted nucleation of α phase in retained β phase by subsequent low temperature aging. Therefore, the nucleation of alpha phase depends

on the heating rate. Settefrati et al. [33] described how the evolution of the α phase depends on the heating rate. Heating rates of 0.14 °C/s, 1.4 °C/s and 3 °C/s were evaluated after isothermal ageing for 2 h at 675 °C, and revealed a finer α phase formation at lower heating rates, as shown in Figure 13.

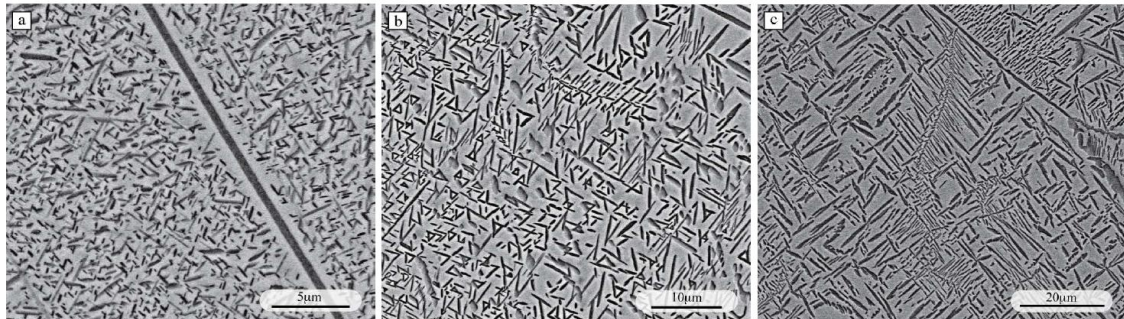


Figure 13. Microstructure containing α phase after isothermal aging for 2 h at 675 °C with different heating rates a) 0.14 °C/s b) 1.4 °C and c) 3 °C/s [33].

The nucleation of the α phase occurred at boundaries or dislocations and developed into ω phase with high β/ω misfits (ω morphology is cuboidal) [34]. For ω phase with low β/ω misfits (ω morphology is ellipsoidal), there were various arguments whether the α laths nucleated at the β/ω misfits, or the ω phase transformed itself to α laths. Therefore, theories from some authors included: α laths appearing at some distances from the β/ω interface; α laths nucleating and growing, while consuming the ω phase; and ω phase transforming into α laths, while keeping the coherent interface between them [34]–[36].

First, α nucleated preferentially at β grain boundaries as more, or less, a continuous grain boundary α layer (α_{GB}), as shown in Figure 14 (b). Further, α plates nucleated on the interfaces of α_{GB} or at the β grain boundaries. The α plates grew as parallel plates, separated with layers of β matrix, and often with only one crystallographic orientation until they reached other colonies. Accordingly, as metastable β alloys, they were able to arrange a Widmanstätten structure. Therefore, they are often indicated as Widmanstätten grain boundary α plates (α_{WGB}), as shown in Figure 14. Teixeira et al. [37] observed between 550 °C – 700 °C, the third form of α phase in a metastable β alloy were acicular α precipitates in basket wave patterns inside the β grain, or α intragranular Widmanstätten (α_{WI}), as shown in Figure 14 (b) [23], [24], [37].

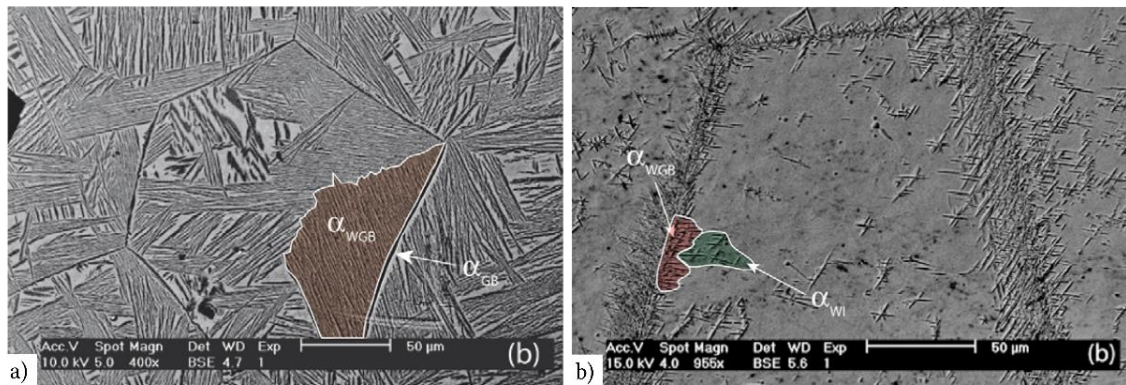


Figure 14. Nucleation of α phase a) example of α_{GB} layer (marked with white arrow) and α_{WGB} (highlighted in brown) and b) example of α_{WI} (highlighted in green) and α_{WGB} (highlighted in red) [37].

2.3 Surface modification technique of metallic biomaterials and its effect on cell viability

Bone is a dynamic tissue, which roughly means it undergoes continual adaption during its lifetime to regulate mineral homeostasis, and to attain and preserve skeletal size, shape and structural integrity. After a bone fractures, it can regenerate by new osseous tissue. Several processes are involved in the bone healing procedure. The first reaction is the emanation of blood from the ruptured vessels. Inflammatory cells, osteoclasts, lymphocytes and plasma cells are therefore attracted. Macrophages, who differentiate from hematopoietic stem cells, play an important role due to the removal of dead tissue (release of inflammatory) and release granulation tissue. The disposal of these factors facilitates the transport of mesenchymal stem cells from the periosteum and bone marrow. Depending on the biological and mechanical condition, the mesenchymal stem cells prompt their differentiation into chondrocytes, osteoblasts or fibroblasts, to name a few. Figure 15 shows processes which are essential for tissue reconstruction and regeneration [38]–[40].

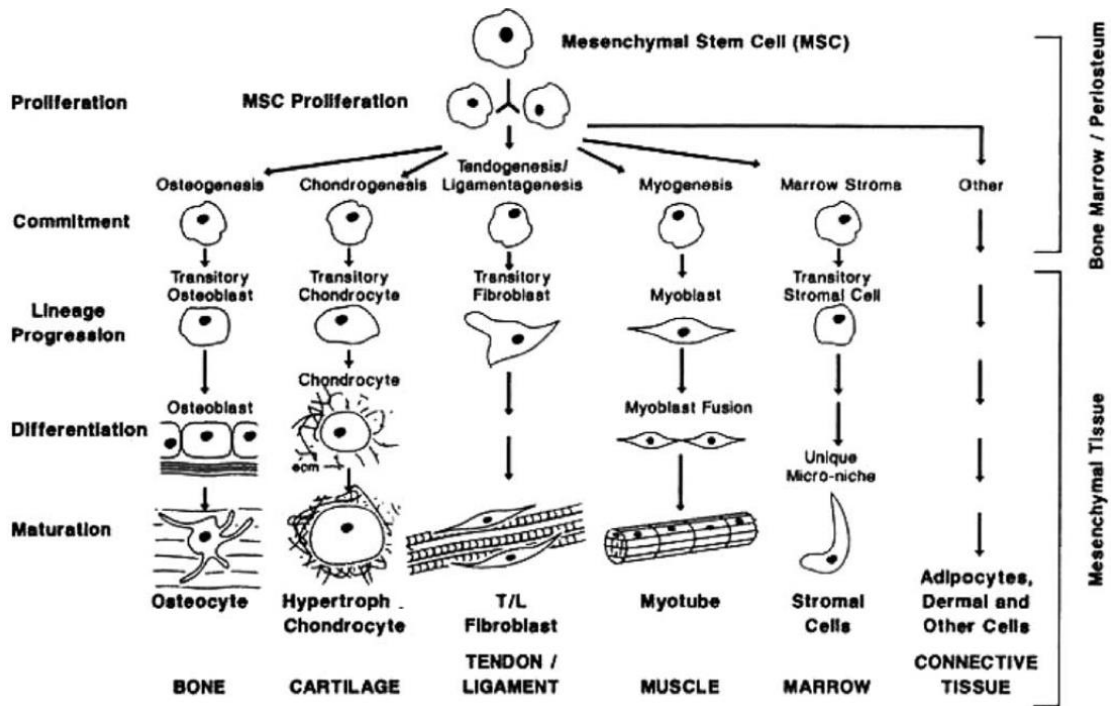


Figure 15. Differentiation of MSC depending on biological and mechanical conditions [40].

At the repair stage, complex sequences of cellular events occur, including cartilage maturation and degradation, vascularity and osteogenesis. At the final stage, the calcification of the cartilage matrix is substituted by woven bone. This summarizes a rough description of bone fracture healing, where important stages were highlighted. The evolution depends on many factors, such as type of fracture, blood supply, hormones, growth factor etc. [38]–[40]. The MC3T3 E1 (pre-osteoblastic) cell line from a new born mouse calvarias was used to evaluate the cell behaviour in the present study.

The success or failure of many biomaterials depends on the physical and chemical characteristics of their surface [41]. Therefore, implant-tissue interaction can be classified regarding the biological behaviour when in contact with living tissue. Wintermantel et al. [42] defined four categories according to the material induced tissue reaction phenomenon: (1) a toxic material causes death to surrounding tissue and cells; (2) a bioinert material is nontoxic, but biologically inactive; (3) a bioactive material is nontoxic and biologically active; and (4) a material is bioresorbable if it is nontoxic, dissolves *in vivo* and the surrounding tissue can be replaced by the synthetic material. The metallic biomaterials stainless steel, Co-based alloys, titanium and its alloys are classified as bioinert materials. A great deal of research has been undertaken to improve the surface characteristics for biomedical applications.

Therefore, different coating techniques [41] are applied to facilitate the process of bone healing. For example, the use of the sol-gel technique enables a homogeneous coating of bioactive bioglass (57.44% CaO, 35.42% SiO₂ and 7.15% P₂O₅) on metallic biomaterial

316L stainless steel [43]. Chen et al. [44] proposed a layer-by-layer deposition on 316L stainless steel by electrophoretic deposition of hydroxyapatite and antibacterial lysozyme embedded in biopolymer coatings to generate a bioactive surface, and inhibit the growth of gram-positive bacteria. An atmospheric pressure plasma jet was utilised to deposit carboxylic/esteric (COOH/R) and amine (NH₂) polymers on a titanium grade 1 substrate to enhance cell adhesion and improve cell differentiation [45].

A huge number of reports propose the influence of implant surface topography on the bone response (osseointegration). This brings another way for a faster and stronger bone formation, which may confer a better stability during the healing process [3], [46]. Different techniques are used to change the surface morphology in a desired way. For example, mechanical grinding with conventional SiC paper was used to change the surface morphology, and it has effected the total human serum protein and fibronectin, as well as on the cellular attachment [45]. The combination of three different surface modification techniques, namely EDM, chemical milling and shot peening, showed positive effects on growth and viability of bone cells [47]. A laser textured surface of titanium alloy controlled the cellular alignment of murine mesenchymal stem cells [48].

Also, combinations of surface treatment techniques have been proposed to improve the interaction between the bone and implant material. For example, the surface topography is changed and additional coatings are applied [49], [50].

There are several characterisation methods to give a 2D, as well as 3D, quantitative characterisation of surface structures. De Chifree et al. [51] published in 2000 that there are 57 different ISO standard parameters to describe the surface in 2D, 14 different ISO standard parameters for 3D, and many more national and company standards. They proposed a guideline for the classification of parameters into categories according to what they describe, followed by an analytical analysis of the correlation. Crawford et al. [52] described the limitation of the most cited parameters Ra and Rq (Sa and Sq for 3D). There, a random surface may show strong correlations, whereas the periodic surface would show incorrect values. For example, Figure 16 displays the limitation of Ra by comparing two sinusoidal profiles with an identical Ra value. Therefore, conflicts have arisen by reported investigations regarding the cell-substratum interactions. They arose because of different types of surface morphology (e.g. irregular, random or hierarchical surface pattern) and inadequate surface characterization conditions. Hence, it is still difficult to compare and recommend a particular surface. The surface characterization conditions vary widely and present an inadequate understanding [3], [46]. Therefore, Wennerberg et al. [3] proposed standardizing the evaluation techniques, and to describe the surface as spatial and hybrid.

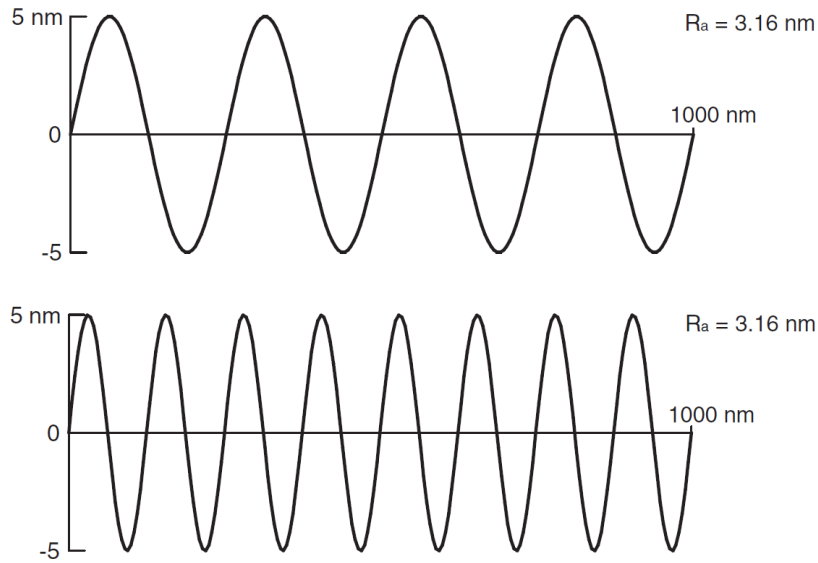


Figure 16. Sinusoidal profiles with identical R_a value [52].

2.4 Electron beam technology for surface structuring

An increasing number of researchers are looking for new technological solutions to optimise the surface of implant materials, and resulting enhanced biocompatibility and osseointegration. Beam processing technique (e.g. electron or laser beam) are promising techniques to control the surface modification of implant materials [53],[54].

Using an electron or a laser beam as a power source brings several options for process control and process environment. The electron beam offers a higher beam power and faster scan speed/beam deflection due to the guiding of electrons by the magnetic field. However, the laser can process in protective gas and vacuum, where for the electron beam a vacuum is necessary (electron beam welding in an atmosphere is possible, but difficult to implement). There are even more differences for additive manufacturing for electron or laser beam concerning process control [55]. The electron beam technique was used for the present study.

The heating source for the electron beam technique is the kinetic energy of electrons shooting on the workpiece. Due to their electric charge, the electrons can be accelerated by an electric field (\vec{E}) and their orbit can be controlled with a magnetic field (\vec{B}). The Coulomb force is the responsible force for acceleration (Figure 17 (a)), while the movement of the electrons is affected by the Lorentz force (Figure 17 (b)).

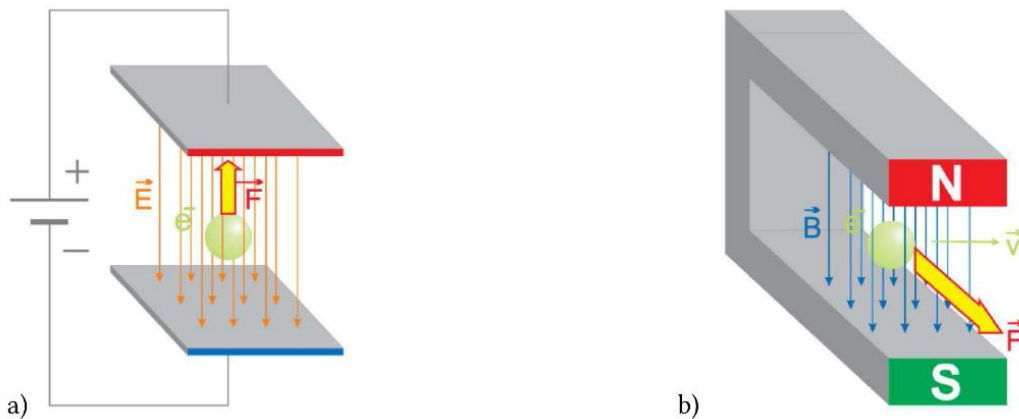


Figure 17. Orientation of the forces due to a) electric field, Coulomb force and b) magnetic field, Lorentz force [56].

Figure 18 shows a schematic illustration of the main components of an electron beam generator for an EBW machine. The cathode is usually made of tantalum, a tungsten-rhenium alloy or less commonly, lanthanum hexaboride, and acts as the electron source. By heating up the cathode, free electrons gain enough energy to leave the surface of the material due to thermal emission. A negative voltage in the bias cup (also known as Wehnelt cylinder) controls the beam current (I_B) impinging on the workpiece. Due to the control of the negative voltage, the electrons can be pushed off by the control electrode back towards the cathode, despite the applied acceleration voltage (U_A), and the effective emitting surface of the cathode can be reduced. The electric field between the anode and cathode is responsible for the acceleration of the electrons. After the anode, a set of magnetic lenses are required to shape and position the electron beam accurately, and are referred to as the beam optics. There, the Lorentz force manipulates the path of the electrons to keep the electrons in the centre (centring coil) and to correct the shape of the beam (stigmator). The lens alters the focus of the beam, so as to place the crossover in the right position on the surface of the workpiece, and for the divergence of the beam. The divergence is thereby responsible for the minimum beam diameter on the workpiece surface, which is equal to the beam intensity in this spot. The bottom part, the deflection system, can deflect the electron beam in the magnetic field (equal working principle to the centring coil) instantaneously and very precisely, because the electron beam is almost without inertia. Several special techniques can be applied due to the quasi simultaneous creation of two or more weld beads. Additionally, a light optical viewing system (CCD camera) and an electron optical viewing system (ELO camera) are equipped in the EB generator to control the process [56], [57].

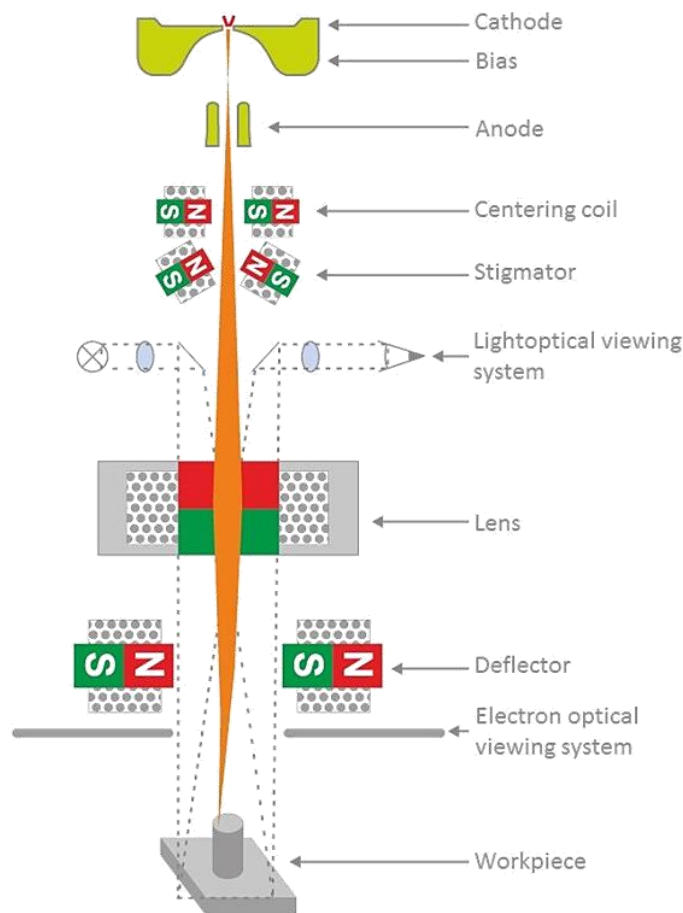


Figure 18. Schematic illustration of an electron beam generator [56].

2.4.1 Electron beam structuring technique

Whenever a beam (electron or laser beam) is used on a material, and the beam power exceeds the order of 10^6 W/cm^2 , the highly focused energy causes an evaporation of the material. A small vapour cavity, the so called “keyhole”, is created and surrounded by molten material, as illustrated in Figure 19 (a). The high vapour pressure in the centre of the keyhole pushes the molten material against the sidewalls of the cavity. When the beam is moved across the work piece, the vapour pressure of the keyhole causes the material to flow around the keyhole to the back of the weld, which results in a protrusion at the beginning and an intrusion at the end of the movement, as shown in Figure 19 (b) [57], [58].

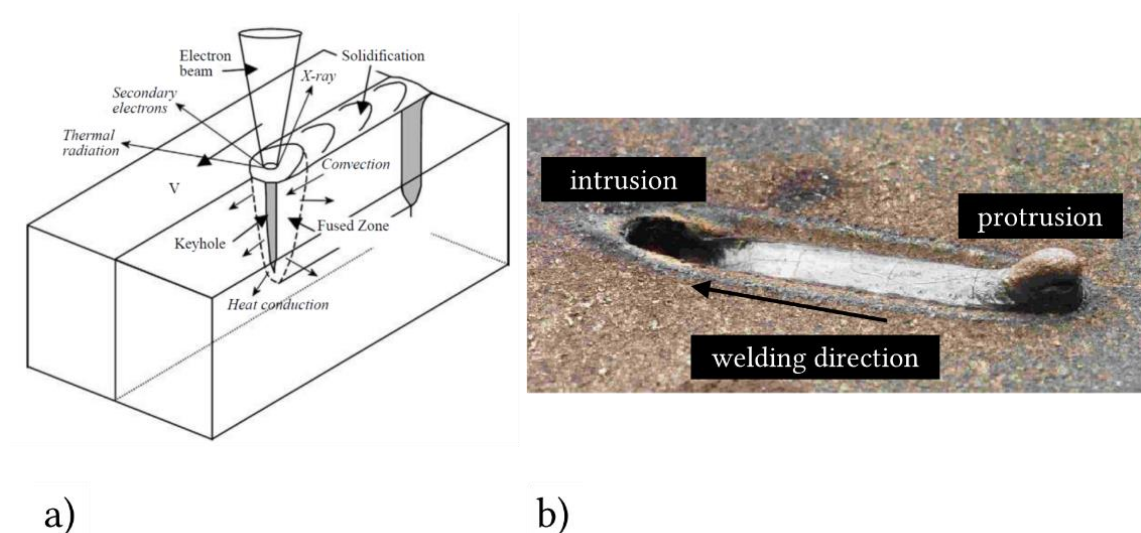


Figure 19. a) Schematic illustration of the moving "keyhole" [59] and b) Protrusion and intrusion effects on stainless steel using laser technology [58].

Therefore, the EB or LB structuring process is based on the effect of creating a protrusion and intrusion. The schematic in Figure 20 illustrates the effect of a repetition of beam movements on the same path. In this case, the protrusion is raised and the intrusion is lowered.

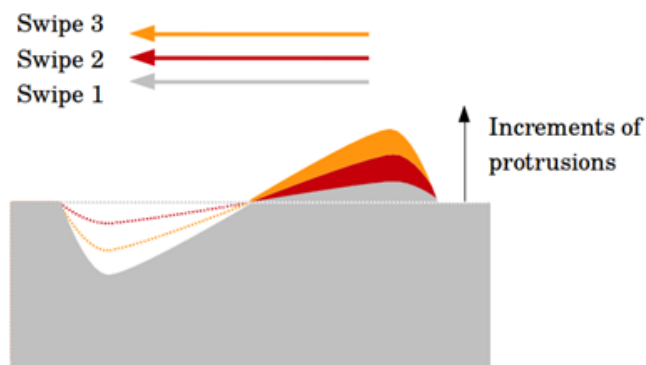


Figure 20. Repetition of beam movement on the same path [60].

Figure 19 (a) shows an example of a deflection approach to design a pin like structure. The beam moves from the centre to the perimeter eight times, as shown in Figure 19 (b). This effect of this type of surface modification was first described by Dance et al., and was referred to as the *Surfi Sculpt*® process [58]. The three dimensional surface modification can be carried out by an electron or laser beam technique [61]–[63]. The application area includes pinning of aluminium sheets for automotive industry [64] and surface structuring of Ti6Al4V for biomedical application [53], among others.

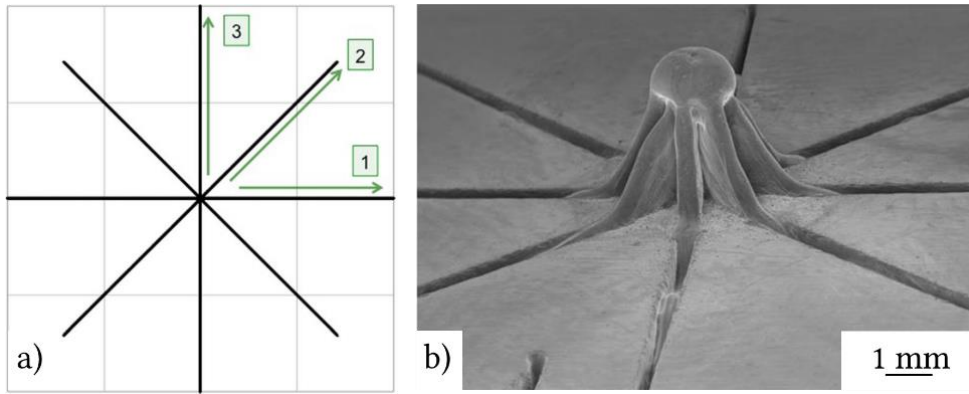


Figure 21. a) Beam deflection figure to design a single pin structure and b) SEM image of pin structure. Adapted from Taendl et al. [64].

The illustration in Figure 22 shows two examples of how to design a deflection figure in an electron beam machine, programmed by Stütz [60].

Therefore, the design consists of four main steps, as displayed in Figure 22:


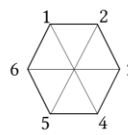
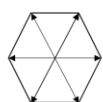
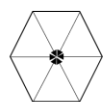
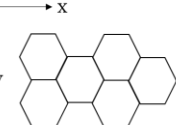

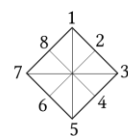
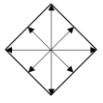
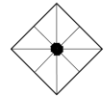
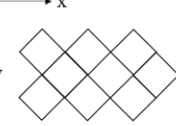

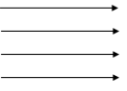
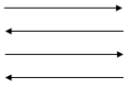

| | 1) figure | 2) electron beam turns | 3) beam travel direction | | 4) array arrangement |
|-----------|--|--|--|---|--|
| example 1 | polygon number of corners: six; hexagon  | arm number: 6  | from the centre to the perimeter:  | from the perimeter to the centre:  | number of polygon figures arranged in x and y direction to an array. x = 2 figures y = 2 figures array 2/2  |
| example 2 | polygon number of corners: four; square  | arm number: 8  | from the centre to the perimeter:  | from the perimeter to the centre:  | number of polygon figures arranged in x and y direction to an array. x = 3 figures y = 3 figures array 3/3  |
| example 3 | line  | number of lines (4) and line spacing (1 mm): 1 _____ 2 _____ 3 _____ 4 _____ | beam travel direction:   | | number of figures arranged in x and y direction to an array. x = 2 figures y = 2 figures array 2/2  |

Figure 22. Schematic illustration of surface deflection design.

- 1) Define a single line or a figure. The figure is defined by choosing the number of corners.
- 2) Specify the amount of electron beam turns that create a surface structure by a set of arms for polygon figures. For lines, set the number of lines and the line spacing.
- 3) Determine the beam travel direction in a single figure.

For example, Figure 23 shows a quarter of a build-up for different beam travel directions of a hexagonal figure. A red line indicates the perimeter of the hexagonal figure. A red arrow denotes the start point of the first arm and the direction of the beam movement. The position the start of the first arm (first coordinate point) is chosen randomly by the NC algorithm. For beam travel directions from the centre to the perimeter, (Figure 23 (a)), a protrusion is in the centre of the figure, and this orientation is termed pin array. The change of the beam travel direction from the perimeter to the centre (Figure 23 (b)) produces an intrusion in the centre of the figure, and this orientation of figure is termed wall array.

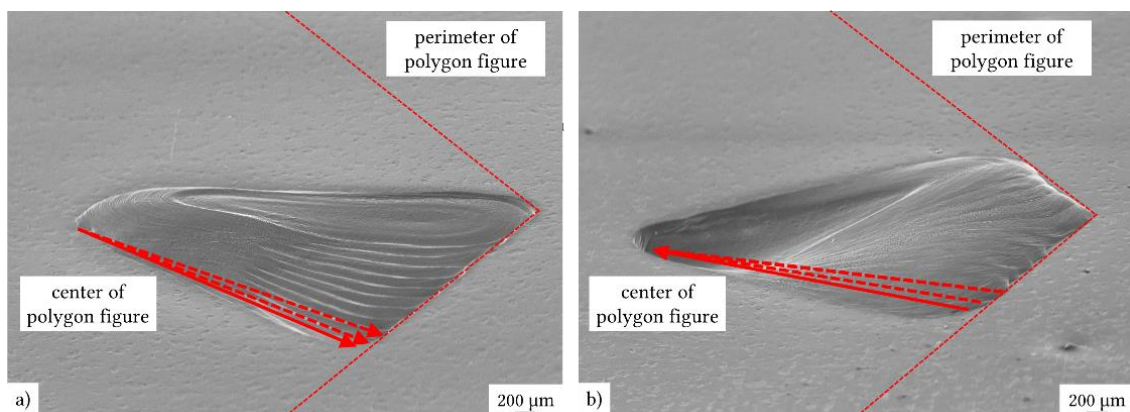


Figure 23. Quarter of hexagonal EB structure for a) a pin structure and b) a wall structure.

- 4) Design the arrangement of the polygon figures, and array, by setting the number of figures in the X and Y directions.

To create a multiple array arrangement simultaneously, the beam is deflected to travel the first arm of every single figure successively before starting over at the second arm of the first single figure, as indicated in Figure 24.

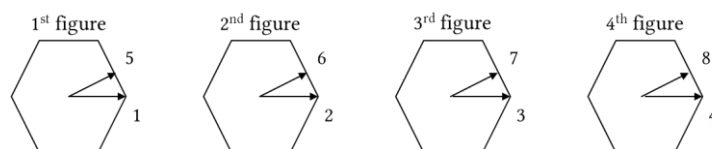


Figure 24. Schematic illustration of simultaneous creation of four figures (4x1 array).

2.5 Solidification and microstructure behaviour after EB process

The schematic in Figure 25 shows the interaction between the heat source (e.g. EB or LB) and the base material. The weld seam shows three distinct regions: the fusion zone (also

termed molten zone, MZ), the heat affected zone HAZ and the unaffected base material BM.

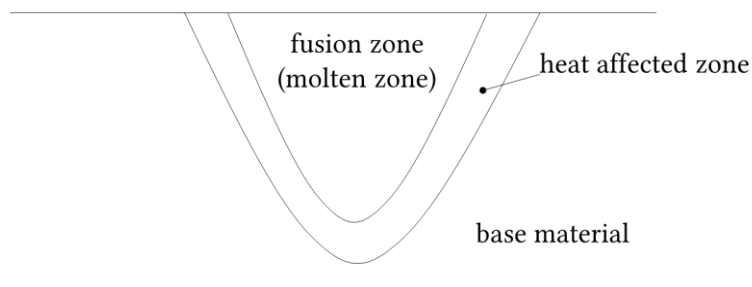


Figure 25. Schematic showing the three distinct zones within a bead on a plate.

The essential information to understand weld pool solidification will be provided here. The solidification is divided into the nucleation and crystal growth processes. The nucleation is traditionally classified as homogeneous or heterogeneous. In practice, homogeneous nucleation occurs under laboratory conditions; however, heterogeneous nucleation is the norm (also for castings), where no additional driving force is necessary to generate nucleation. Therefore, the crystal growth initiation in a weld pool is influenced by the base material grain size and orientation. In Figure 26, the crystal orientation of the base material has an effect on the growth of the weld metal, where for non-allotropic materials, an epitaxial growth related to the grains in the HAZ appear, compared to allotropic materials (e.g. steel, titanium etc.).

Parameters to determine the solidification structure are solidification (R), temperature gradient (G), undercooling (ΔT) and the alloy composition. The effect of GR and G/R on the solidification microstructure is illustrated in Figure 27 (a). A variation of parameters leads to different solidification microstructure, therefore it can be equiaxed dendritic, columnar dendritic, cellular or planar with increasing G/R value, as shown in Figure 27 (a). The solidification map for Ti6Al4V, shown in Figure 27 (b), can be used to judge what structure can form during solidification of the AM processes [65], [66].

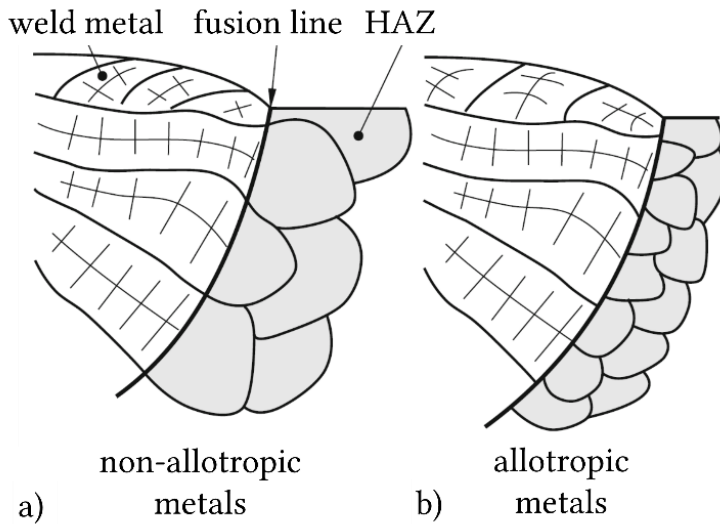


Figure 26. Epitaxial growth of weld pools for a) non-allotropic materials, where grain growth is related to HAZ and b) allotropic materials, where grain growth is not related to HAZ (no epitaxial growth). Adapted from [66].

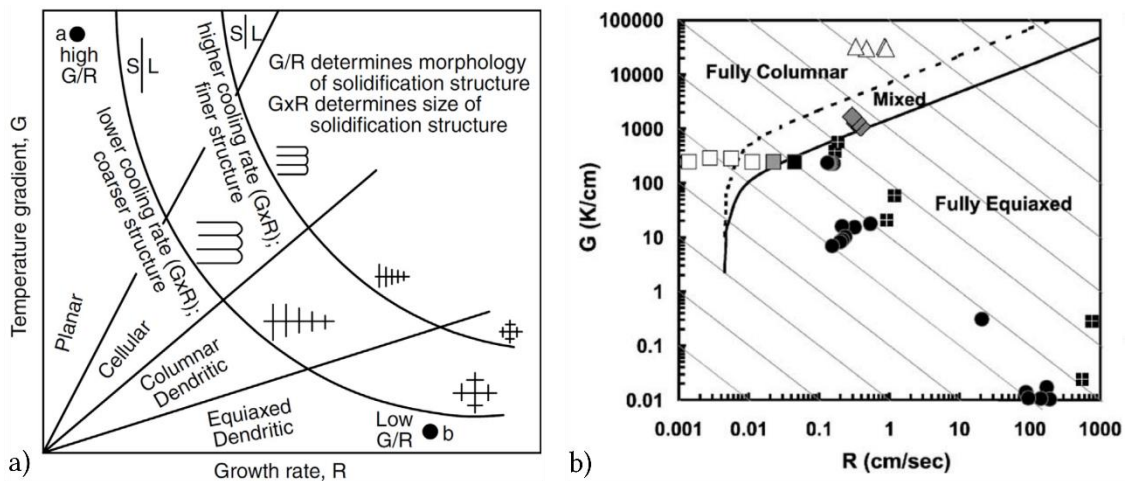


Figure 27. a) Morphology and size of the solidification microstructure depending on the temperature gradient G and growth rate R and b) solidification map for Ti6Al4V [65].

It is common to observe nonequilibrium solidification effects after welding, especially during high-power-density welding processes, such as electron beam or laser beam. Due to the increase of the solidification growth velocity, the nonequilibrium features can be associated with the partitioning of solute between solid and liquid, or a change in the solidification phenomenon, resulting in nonequilibrium phase formation. Therefore, segregation play a crucial role and can be classified as microsegregation (propagating over distances of the grain diameter or less) or macrosegregation (propagating over more than several grain diameters). The microsegregation can be subdivided into cellular or cellular-dendritic growth. Moreover, the flatter the thermal gradient, the higher the alloy content and the greater the tendency for cellular or cellular-dendritic growth [66]–[68].

Several studies indicated that due to the very high cooling rate, nucleation of the grains occurs at the fusion line and they tend to grow in the direction of the heat generation (towards the weld centreline) [69]–[72]. The solidification phenomenon in the fusion zone of Ti6Al4V indicated an epitaxial, columnar or dendritic prior β grain growth [69]–[71]. Where cp Ti exhibited severely coarse and some columnar grains [72]. The microstructure of Ti6Al4V weld seams consists of acicular α' martensitic structure due to the high cooling rate from β phase field [73]. In contrast to Tsai et al. [70], who presented on Ti6Al4V EBW samples, measurements of the fusion zone with X-ray diffraction indicated a potential generation of $\alpha_2\text{Ti}_3\text{Al}$ and $\gamma\text{-TiAl}$ intermetallic compounds.

The high energy beam processes (EB and LB) are furthermore used to selectively melt layers of metal powder or wires (AM processes). The AM process can be compared to a repetitive welding process, where stacking of multiple welds next to another to produce a 3D geometry. The welding process is distinguished due to the joining two, or more, geometries into one. For AM, the joining defines the geometry [55].

The solidification and microstructure after AM processes are strongly linked to the cooling and heating rates, as well as to the scan strategy (parallel, cross-hatching and so on). The solidification parallel to the building direction (z direction) of different titanium alloys (α , $\alpha+\beta$ alloy and metastable β alloy) showed extended columnar grain structure through many layers [71], [74], [75], as shown in Figure 28. This type of solidification is typical for partial re-melting of the top of the columnar grains (due to the re-melting of the previous layer). They act as a nucleus for epitaxial growth of the strongly textured grains [74], [76]. However, scan track boundaries in Ti6Al4V indicated by white arrows in Figure 28 (a), and in Ti-5553 as depicted in Figure 28 (b), appear as a nose-shape. These scan track boundaries define the solidified melting pool [77].

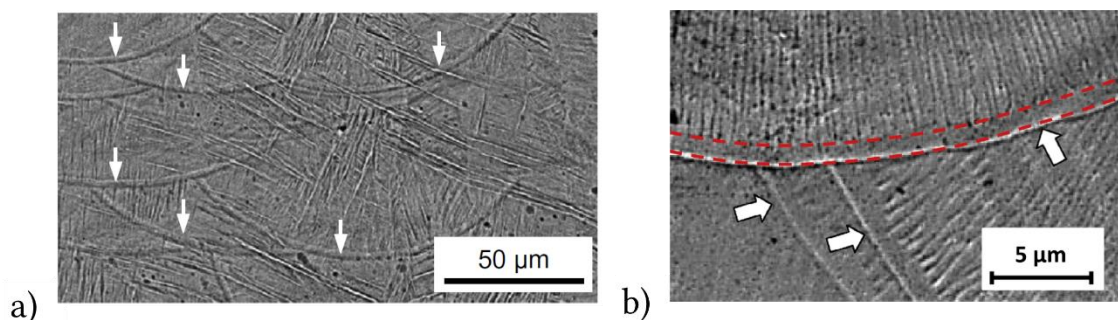


Figure 28. Solidification phenomenon parallel to the building direction for a) Ti6Al4V [77] and b) Ti-5553 [78].

Yamanaka et al. [75] reported a non-equiaxed and plate-like microstructure (weak-textured) for cp TiGr2 EBM perpendicular to the build direction. The microstructure of TiGr1 after SLM revealed mainly of lath-type α' and, in some areas, α' martensite [79]. The variation of size and morphology of the martensitic phase can be linked to varying

cooling rates across the sample by changing the SLM scan strategy. A refinement of the α phase from a coarse lath-shape α to refined structured martensitic α' was observed by an increase of the applied laser speed. This change was due to the elevated thermal and kinetic undercooling and attendant solidification rate [80].

Schwab et al. [74] showed a cellular and cellular-dendritic structure inside the grain of a metastable β Ti alloy due to a destabilization of the planar solidification. This was caused by changing the ratio of the thermal gradient and the solidification rate, as indicated in Figure 29, point 1. The same phenomenon was reported for AlSi10Mg, CoCrMo and 316L materials after SLM, by Prashanth et al. [81].

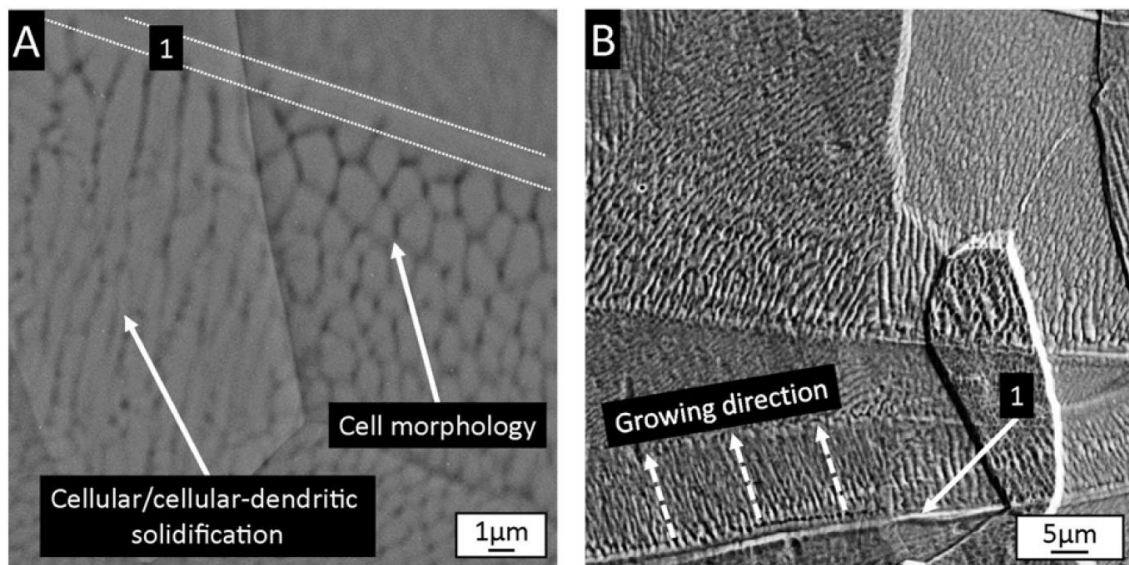


Figure 29. a) Solidification of cellular / cellular-dendritic morphology in Ti-5553 by SLM and b) change of planar solidification to cellular. Adapted from Schwab et al. [74].

The extremely high cooling rate, estimated to be around 10^4 K/s [76] for SLM, is typical for AM processes, and a fully α' martensitic microstructure usually forms in Ti6Al4V alloys [71], [76], [78]. Therefore, post heat treatments of Ti6Al4V were carried out after AM to enhance the mechanical behaviour (to increase the ductility) [76]–[78]. Vilaro et al. [76] proposed heat treatments to fully restore homogeneous and stable microstructures, where they investigated low temperature and high temperature strategies. For low temperature strategies (subtransus heat treatments), it is expected that the thermal stresses from the process are relieved, and a partial decomposition of the as-fabricated α' phase into the more stable $\alpha+\beta$ and needle α' phases will result (β phase is poor in Vanadium). The high temperature strategies involve a solution treatment (subtransus or supertransus), followed by a tempering treatment. The subtransus solution treatment leads to the decomposition of the as-fabricated microstructure (as explained), and it does not enable a modification of grains. In contrast to the supertransus solution treatment, it is not only possible to form new martensite, but also change grain morphology due to shearing of the

long columnar grains. Figure 30 (a) clearly illustrates the change of the grain morphology after supertransus solution treatment, compared to Figure 30 (b). The followed tempering treatment enables the change of the width of the α plates. This change is mainly dependent on the maximum temperature, holding time and cooling rate, although their influence increases when the temperature is closer to the β transus [78].

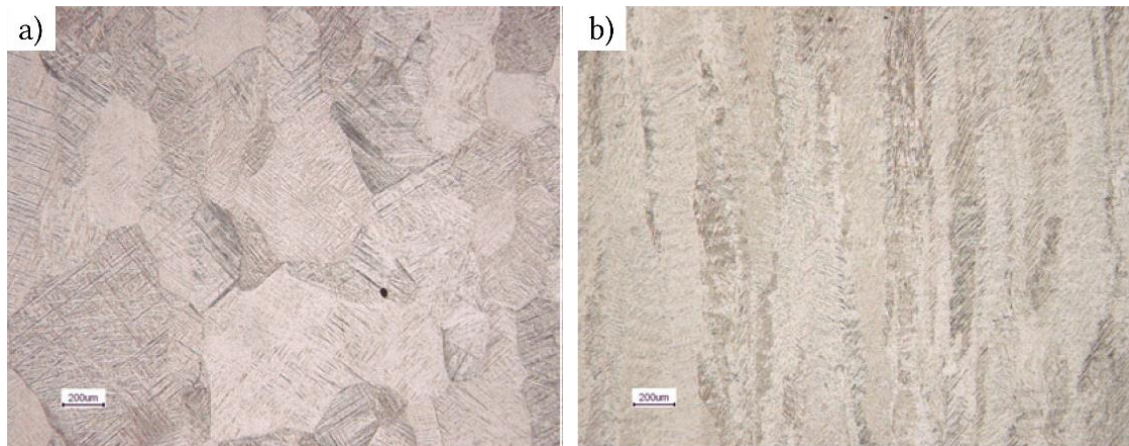


Figure 30. Microstructure of Ti6Al4V after a) supertransus solution treatment at 1050 °C / 1h WQ and b) subtransus solution treatment at 950 °C / 1h WQ. Adapted from Vilaro et al. [76].

2.6 Objectives

The main objective of this thesis is to examine EB structuring of three different titanium alloys to improve the interaction between the implant material and the biological environment. The purpose of the present work is therefore threefold: developing a novel structuring technique for biomedical application, gaining an understanding of microstructural changes after EB structuring process and developing new biomaterials.

Therefore, two established titanium alloys out of the α and $\alpha+\beta$ alloy class, and a novel metastable β titanium alloy, were used for this work. The metastable β titanium alloy is capable of achieving requirements for permanent orthopaedic devices with lower elastic modulus. However, this class has particular significance in the development of new biomaterials.

3 Description of methodology

This chapter presents the investigated materials and the equipment which were used to change the surface topography. Following this, observations of the surface topography changes and microstructural testing are introduced for the characterization of the mechanical behaviour and surface topography. The description of the in vitro investigations to evaluate the surface topography concludes the chapter.

3.1 Investigated materials

Three different titanium alloys were investigated in this work, with a different Young's modulus: α alloy (commercial pure titanium alloy TiGr2), $\alpha+\beta$ alloy (Ti6Al4V) and a metastable β titanium alloy (Ti15Mo). For cp TiGr2 specimens, 15 x 15 mm samples were cut by water jet from a sheet of 2 mm thickness. The as-received materials, Ti6Al4V and Ti15Mo, were delivered in wrought bars of \varnothing 200 mm x 20 mm and \varnothing 25 mm x 10 mm, respectively. The Ti6Al4V (15 x 15 x 2 mm) and Ti15Mo (15 x 10 x 2 mm) specimens were produced by wire cutting. The surface of the specimens was mechanically polished with silicon paper up to P4000 to induce the same surface condition.

3.1.1 α alloy

The EB structuring of a cp TiGr2 alloy was studied. Its chemical composition limits and the actual chemical composition in weight percent are listed in Table 3.

Table 3. Chemical composition of commercial pure (cp) TiGr2 in wt% [82].

| Elements in wt % | | Ti | Fe | C | N | O | H |
|--------------------|------|------|------|------|------|------|-------|
| Requirements | min. | base | - | - | - | - | - |
| | max. | base | 0.30 | 0.08 | 0.03 | 0.25 | 0.015 |
| Actual composition | min. | base | 0.06 | 0.02 | 0.01 | 0.12 | 0.002 |
| | mix. | base | 0.08 | | | | |

It was supplied in the cold rolled and annealed condition by Baoji titanium industry Co [82]. Figure 31 shows the microstructure of the as-received cp TiGr2 material.

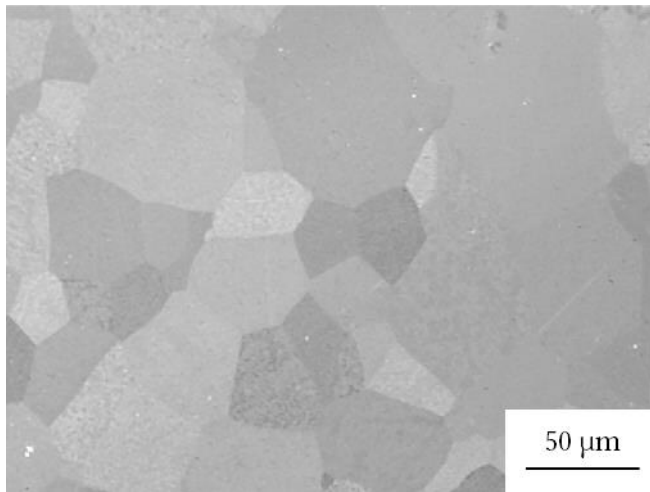


Figure 31. Microstructure of as received cp TiGr2.

Table 4 shows the physical and mechanical properties from the literature for cp TiGr2.

Table 4. Physical and mechanical properties of cp TiGr2 as reported in the literature.

| Physical property | | Value | Unit | Reference |
|------------------------------|---------|--------------|-----------------|-------------|
| Liquidus temperature | | 1665 ± 5 | °C | [83] S. 219 |
| Density | 20 °C | 4.51 | g/cm^3 | [83] |
| β -transus temperature | | 913 ± 15 | °C | [83] S. 177 |
| Young's Modulus | | 105 – 110 | GPa | [84] |
| Thermal conductivity | 20 °C | 20.8 | W/mK | [85] |
| | 650 °C | 15.8 | W/mK | [85] |
| | 1665 °C | 15.8 | W/mK | [85] |
| Specific heat | RT | 523 | J/kgK | [83], [85] |
| Mechanical property | | Value | Unit | Reference |
| Ultimate tensile strength | | 345 | MPa | [83] |
| Yield strength | | 250 | MPa | [84] |

3.1.2 $\alpha+\beta$ alloy

The EB structuring and additional heat treatments of the $\alpha+\beta$ alloy Ti6Al4V were studied in this work. Its chemical composition limits and the actual chemical composition in weight per cent are given in Table 5.

Table 5. Chemical composition of Ti6Al4V in wt% [86].

| Elements in wt % | | Ti | Al | V | Fe | O ₂ | C | N ₂ | H ₂ | Y |
|--------------------|------|------|------|------|------|----------------|-------|----------------|----------------|--------|
| Requirements | min. | base | 5.50 | 3.50 | - | 0.17 | - | - | - | - |
| | max. | | 6.75 | 4.50 | 0.30 | 0.20 | 0.08 | 0.05 | 0.008 | 0.005 |
| Actual composition | min. | base | 6.51 | 4.10 | 0.18 | 0.18 | 0.032 | 0.022 | 0.0007 | <0.001 |
| | max. | | 6.57 | 4.32 | 0.22 | 0.19 | 0.033 | 0.024 | 0.0006 | |

Ti6Al4V was delivered in a bimodal annealed condition, as shown in Figure 32. The material was forged in different steps and afterwards, annealed at 730 °C for 1h and cooled in air [86].

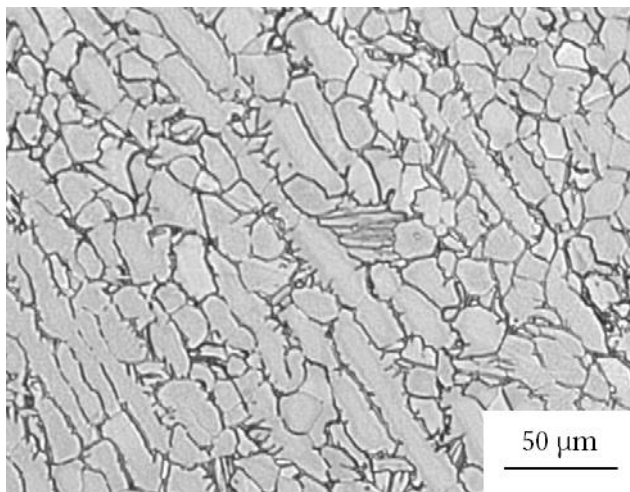


Figure 32. Microstructure of the as received Ti6Al4V.

The physical and mechanical properties of Ti6Al4V are given in Table 6.

Table 6. Physical and mechanical properties of Ti6Al4V as reported in the literature.

| Physical property | | Value | Unit | Reference |
|-------------------------------------|---------|-------------|-------------------|-------------|
| Liquidus temperature | | 1650 - 1660 | °C | [83] p. 516 |
| Density | 20 °C | 4.43 | g/cm ³ | [83] p. 495 |
| β-transus temperature | | 1020 ± 5 | °C | [86] |
| Young's Modulus | | 105 – 116 | GPa | [83] p. 494 |
| Thermal conductivity | 20 °C | 6.6 | W/mK | [85] |
| | 650 °C | 17.3 | W/mK | [85] |
| | 1665 °C | 17.3 | W/mK | [85] |
| Specific heat | RT | 526 | J/kgK | [85] |
| Mechanical property (base material) | | Value | Unit | Reference |
| Ultimate tensile strength | | 1009 – 1054 | MPa | [86] |
| Yield strength | | 923 – 964 | MPa | [86] |

3.1.3 Near β alloy

EB structuring and evolution of the ω_{iso} and α phases after additional heat treatments were investigated on the near β titanium alloy Ti15Mo. The chemical composition limits and the actual chemical composition in weight per cent are listed in Table 7.

Table 7. Chemical composition of the near β titanium alloy Ti15Mo in wt% [87].

| Elements in wt % | | Ti | Mo | Fe | C | N | O | H |
|--------------------|------|------|-------|------|------|-------|------|-------|
| Requirements | min. | base | 14.00 | - | - | - | - | - |
| | max. | | 16.00 | 0.10 | 0.10 | 0.05 | 0.20 | 0.015 |
| Actual composition | min. | base | 15.60 | 0.04 | 0.01 | 0.012 | 0.15 | 0.002 |
| | max. | | 16.00 | 0.06 | | 0.016 | | |

The investigated Ti15Mo near β titanium alloy was delivered in β annealed condition. The cooling rate after beta annealing was not indicated. The microstructure in the as received condition is shown in Figure 33. The physical and mechanical properties of Ti15Mo are given in Table 8.

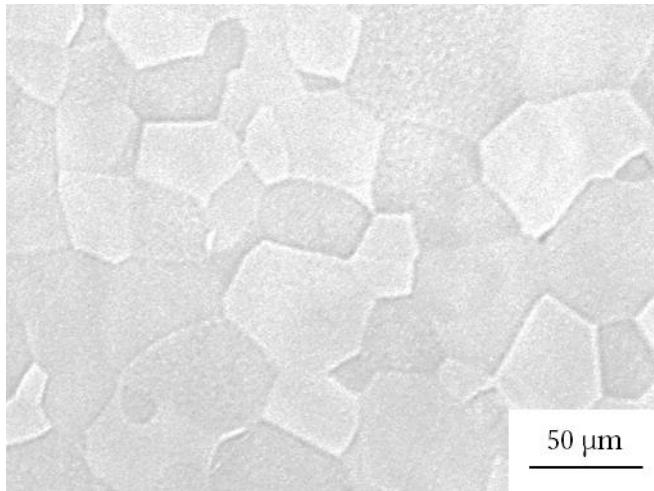


Figure 33. Microstructure of the as-received Ti15Mo.

Table 8. Physical and mechanical properties of Ti15Mo (β and $\alpha + \beta$ annealed) as reported in the literature.

| Physical property | | Value | Unit | Reference |
|-------------------------------------|-------|-------------------------------------|-------------------|------------|
| Liquidus temperature | | 1704 - 1760 | °C | [88] |
| Density | 20 °C | 5.4 | g/cm ³ | [89] |
| β -transus temperature | | 774 \pm 14 | °C | [88] |
| Young's Modulus | | 78 ¹ 106 ² | GPa | [21], [88] |
| Thermal conductivity | 31 °C | 12.56 | W/mK | [90] |
| Specific heat | RT | 500 | J/kgK | [89] |
| Mechanical property (base material) | | Value | Unit | Reference |
| Ultimate tensile strength | | 775 – 785 | MPa | [87] |
| Yield strength | | 715 - 730 | MPa | [87] |

¹ β annealed condition

² $\alpha + \beta$ annealed condition

3.2 Electron beam process

3.2.1 Electron beam welding machine

The Universal Chamber EBG 45-150 K14 Machine from pro beam was used for electron beam welding, and is shown in Figure 34. It was used for the following investigations.



Figure 34. EBW machine at Institute of Materials Science, Joining and Forming.

The machine was equipped with several investigation and sensor systems, such as a CCD camera for observation, an ELO-Tool for an electron-optical picturing of the processes and X-ray sensor system. The control occurs by a numerical control (NC) unit. The modular beam gun can be mounted horizontally or vertically. In this work, the beam gun was mounted horizontally. An aluminium sample holder prevented shifting of the specimens during the structuring process. The operating distance was 20 mm above the working table. The EB structuring process was carried out under a vacuum between 1×10^{-4} and 4×10^{-4} mbar. Further important technical specifications are shown in Table 9.

Table 9. Technical specification for Universal Chamber EBG 45-150 K14 by pro beam.

| | |
|--|-----------------------------|
| EB generator | |
| Power | 45 kW |
| High voltage | 150 kV* |
| Beam current | 0.1 – 300 mA |
| Beam oscillation | 1 °/μs |
| Chamber | |
| Volume | 1.4 m ³ |
| Table feed rate | 0.5 – 100 mm/s |
| Vacuum (operating pressure) | |
| Evacuation time | < 6 min |
| EB gun | ≤ 5 x 10 ⁻⁵ mbar |
| Chamber | ≤ 5 x 10 ⁻³ mbar |
| *for commonly used cathode type (pb.350.7) | |

3.2.2 Electron beam positioning

The Universal Chamber EBG 45-150 K14 Machine from pro beam allows the control and manipulation of the electron beam due to the fast electromagnetic control of the beam. There are three principles of beam positioning in X/Y: plane point-figures, vector-figures and grey-scale figures. For vector figure, the start and end positions are defined. The free path between these two points will be vectorised and can be scaled for size in any way. Vector figures cannot create disconnected deflection positions. The grey-scale figures had no meaning for these investigations. For the following investigations, the point-figures, termed deflection figures, were used. Therefore, the beam deflection routine interpreted coordinate data in the range of 0 to 65,535 increments, while the actual X and Y dimensions were determined separately in the numerical control (NC) program. The coordinate data (X/Y) were read line by line from a plain text file. For the creation of deflection figures, programs such as Text editor from Microsoft, Microsoft Excel or Matlab can be used, among others. For a better understanding, an example of beam travel for two positions is given in Figure 35. The beam velocity can be controlled in two ways. In the NC program of the EB machine, the dwell time of the electron beam for each coordinate point X/Y (figure point) can be set. This procedure is used to proceed an unknown number of points in a deflection figure. For proceeding a known number of

points in a deflection figure, the read rate of the coordinate file and the dwell time for the total process were set in the NC program. For the following investigations, the beam velocity was controlled by the read rate and dwell time for the total process.

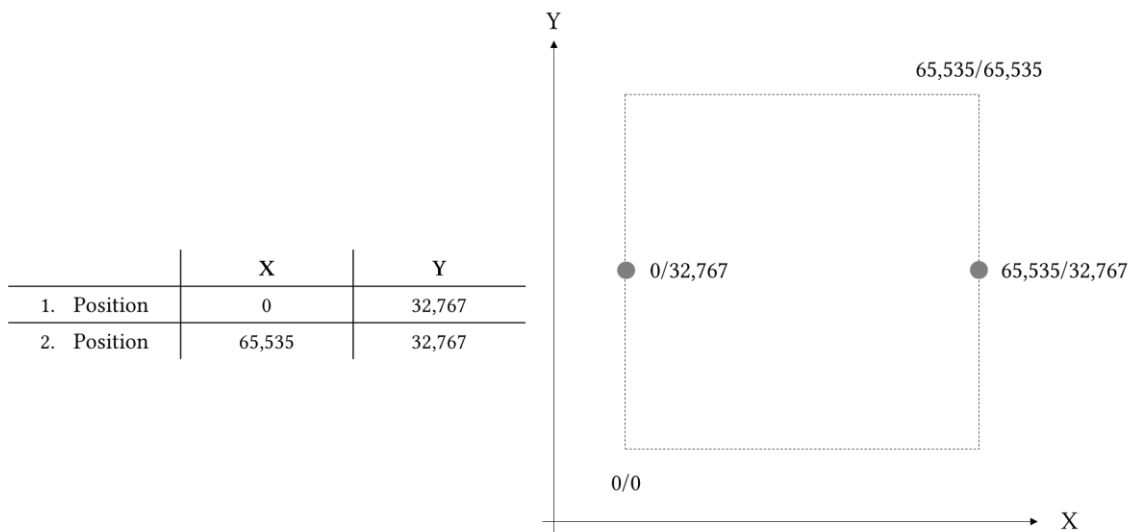


Figure 35. Schematic figure of EB deflection of two positions (grey points).

3.2.3 Design of surface geometries

The link between the beam positioning in X/Y (deflection figure) and the control of the energy input (beam voltage, beam current and beam deflection velocity) influence the design of surface geometries.

The set up to produce surface geometries was performed as follows. First, the adjustment of the energy input was determined, denoted by voltage, beam current and beam velocity. Next, a deflection figure was generated by coordinate points. Finally, the sizing of the structure was done by setting the X and Y amplitudes in the NC program. The routine to design deflection figures and create the corresponding coordinate files was programmed with Matlab [60]. In this work, the lines, hexagonal, trigonal and square figures with different arm numbers and array arrangements were used, as summarized in Table 10 and Table 11.

3.2.4 EB parameters (bead on plate and structuring)

Countless parameters influence the quality of the EB process. For example, the EB EBG 45-150 K14 machine contains more than 100 parameter settings that can be changed, including obvious ones such as the EB power (velocity and current) and beam velocity, but also the beam intensity distribution, focus position and many more. For these investigations, only the energy input controlled by the voltage, beam current and beam velocity were changed. The acceleration voltage was kept constant, due to a high beam stability condition and a small beam diameter at 150 kV [57]. The lowest value for the

beam current was set at 0.8 mA, due to the beam focus at the surface. Table 10 and Table 11 list the EB parameter combinations of EB bead on plate and EB structuring.

Table 10. Parameters for electron beam bead on plate and subsequent investigations.

| Material | Energy input | | | Beam deflection | | | | Metallographic investigations |
|---------------------------------|--------------|---------|----------|-----------------|---------------|-------------|-------------|-------------------------------|
| | Voltage | Current | Velocity | Number of lines | Line distance | X amplitude | Y amplitude | |
| | kV | mA | mm/s | | mm | mm | mm | |
| cp TiGr2, Ti6Al4V, Ti15Mo | 150 | 0.8 | 338 | 13 | 1 | 13 | 13 | x |
| | | 0.8 | 676 | 13 | 1 | 13 | 13 | x |
| | | 0.8 | 169 | 13 | 1 | 13 | 13 | x |
| | | 2.5 | 338 | 13 | 1 | 13 | 13 | x |
| | | 2.5 | 169 | 13 | 1 | 13 | 13 | x |
| | | 2.5 | 676 | 13 | 1 | 13 | 13 | x |

Table 11. Parameters for electron beam structuring figures and subsequent investigations.

| Material | Energy input | | | Beam deflection | | | | | | Metallographic investigations | Surface roughness | Cell cultivation | | | | |
|----------|--------------|---------|----------|-----------------|------------|-------------|-------------|-------------|---------------|-------------------------------|-------------------|------------------|------|------|------|--|
| | Voltage | Current | Velocity | Polygon form | Arm number | Array (x/y) | X Amplitude | Y Amplitude | Beam movement | | | 6 h | 12 h | 24 h | 48 h | |
| | kV | mA | mm/s | | | | mm | mm | | | | | | | | |
| cp TiGr2 | 150 | 2.5 | 697 | hexagonal | 96 | 2/4 | 13 | 8.65 | pin | x | x | | | x | X | |
| | | 2.5 | 697 | hexagonal | 96 | 2/4 | 13 | 8.65 | wall | x | x | | | | | |
| | | 0.8 | 341 | hexagonal | 96 | 2/4 | 13 | 8.65 | pin | x | x | | | | | |
| Ti6Al4V | 150 | 2.5 | 697 | hexagonal | 96 | 2/4 | 13 | 8.65 | pin | x | x | x | x | x | X | |
| | | 2.5 | 697 | hexagonal | 96 | 2/4 | 13 | 8.65 | wall | x | x | | | | | |
| | | 0.8 | 341 | hexagonal | 96 | 2/4 | 13 | 8.65 | pin | x | x | x | x | x | x | |
| | | 2.5 | 916 | hexagonal | 126 | 2/4 | 13 | 8.65 | wall | x | | | | | x | |
| | | 2.5 | 1135 | hexagonal | 156 | 2/4 | 13 | 8.65 | wall | x | | | | | x | |
| | | 2.5 | 715 | square | 100 | 3/3 | 12 | 10 | 10 | pin | x | | | | x | |
| | | 2.5 | 715 | square | 100 | 3/3 | 12 | 10 | 10 | wall | x | | | | x | |
| | | 2.5 | 631 | triangular | 99 | 4/2 | 10 | 6.92 | 6.92 | pin | x | | | | | |
| Ti15Mo | 150 | 2.5 | 697 | hexagonal | 96 | 2/4 | 13 | 8.65 | pin | x | x | | | x | x | |
| | | 2.5 | 697 | hexagonal | 96 | 2/4 | 13 | 8.65 | wall | x | x | | | | | |
| | | 0.8 | 341 | hexagonal | 96 | 2/4 | 13 | 8.65 | pin | x | x | | | | | |

3.3 Dilatometry

The dilatometry experiments were carried out using a BÄHR Thermoanalyse DIL805 dilatometer under vacuum and quenched by argon or helium gas. Rectangular samples with a thickness between 4 and 5 mm and a height of 10 mm were used. Each sample was placed in the dilatometer between two silica tubes, the chamber was evacuated and the sample heated by induction. The temperature was controlled by a type K (Ti15Mo and Ti6Al4V) thermocouple welded in the middle of the sample, and if necessary the elongation of the sample was measured.

3.3.1 Heat treatments of $\alpha+\beta$ alloy Ti6Al4V

Heat treatments on EB structured specimens were performed in order to stabilize the molten zone. The temperature cycle is shown in Figure 36, where the heating rate was 300 K min^{-1} up to $650 \text{ }^\circ\text{C}$ and $720 \text{ }^\circ\text{C}$, and then temperature was held there for 2 h and 8 h. The quenching was by argon gas to retain the microstructure for further observations.

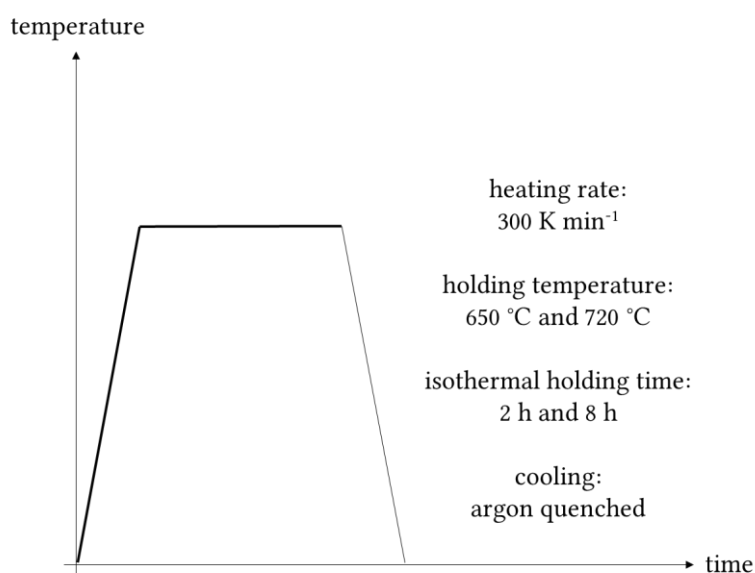


Figure 36. Schematic illustration of additional heat treatments on EB structured samples.

3.3.2 Dilatometry and heat treatments of near β titanium alloy Ti15Mo

Phase transformation investigations after different heating rates on as-delivered specimens were done within two temperature cycles, as illustrated in Figure 37. For temperature cycle 1, the specimens were heated at 300 K min^{-1} to $850 \text{ }^\circ\text{C}$, held for 10 minutes and then quenched under argon atmosphere to achieve a solution treated condition and ensure the same starting condition for temperature cycle 2. To evaluate the phase change after different heating temperatures, temperature cycle 2 consisted of different heating rates. The samples were heated at 5, 100, 200 and 300 K min^{-1} up to $850 \text{ }^\circ\text{C}$ and $580 \text{ }^\circ\text{C}$, held for 5 s and then quenched under

argon gas to retain the microstructure for further investigations. The relative change of length plotted versus the temperature was used to determine the transformation temperatures by the tangent method [91]. A line was drawn following this curve. The transformation temperatures were defined as the point where the tangent deviated from the curve.

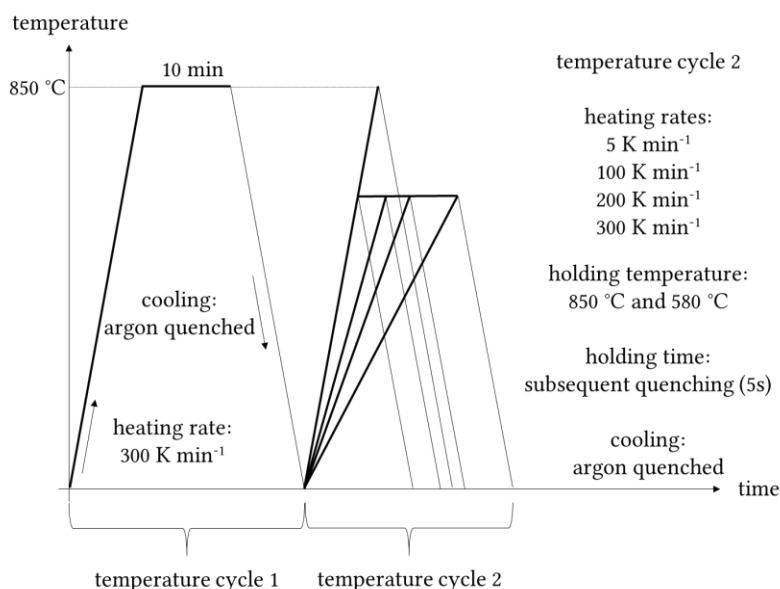


Figure 37. Schematic illustration of phase transformation investigations for different heating rates for Ti15Mo.

In order to determine the evolution of precipitates in Ti15Mo during heating at 300 K min⁻¹ and after EB, the structuring ageing tests were carried out, as illustrated in Figure 38. For the Ti15Mo base material, investigations for temperature cycle 1 were done to achieve a solution treated condition for temperature cycle 2 (as mentioned in section 3.1.3). Therefore, the specimen was heated up to 850 °C with a heating rate of 300 K min⁻¹, held for 10 min and then quenched under argon gas. For temperature cycle 2, the samples were kept at a different holding temperature and isothermally aged for 8 h or quenched after 5 s (termed as subsequent quenching) under argon gas to retain the microstructure for further observations. Investigations on EB structured Ti15Mo were carried out in the same way as for investigations on the base material, but without the solution treatment (temperature cycle 1).

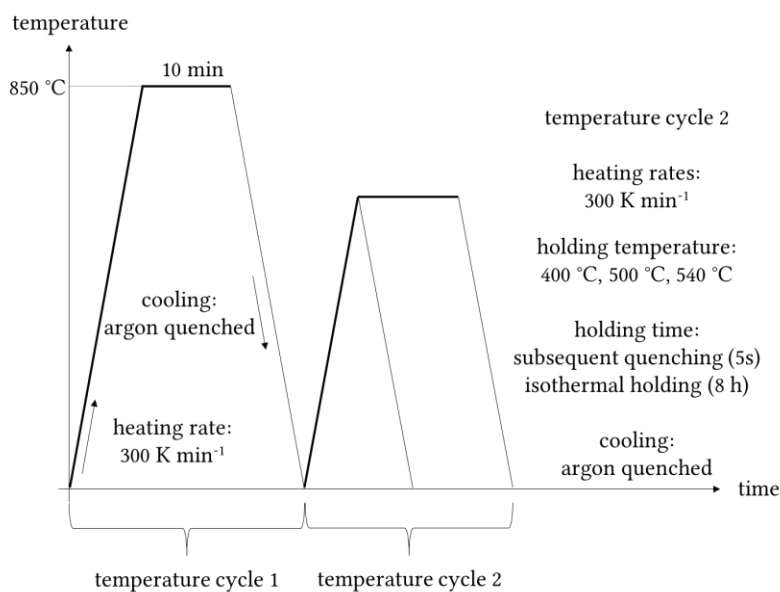


Figure 38. Schematic illustration of heat treatments for Ti15Mo.

3.4 Metallography

3.4.1 Sample preparation

Two different metallographic sample preparations were performed: preparation of the sample surface and preparation for material characterization. The sample surface preparation was carried out before the EB process to ensure the same surface condition for material and cell investigations. Therefore, the surface of each specimen was polished by hand with SiC paper up to P 4000. The sample preparation for material characterization consisted of hot embedding, grinding, polishing and etching, as required to reveal the microstructure for light optical microscopy (LOM). Characterization with the scanning electron microscope (SEM) and electron backscattered diffraction (EBSD) were carried out on embedded, grinded and polished specimens. To enhance the quality of the measurements, some specimens were abstract of the resin. The sample preparation procedures, listed in Table 12, were done with a semi-automatic with Struers Tegra Pol-31.

Table 12. Sample preparation and etchant for material characterization.

| Steps | Consumables | Lubricant | Time [min] | Force [N]/sample |
|--|----------------------------|----------------|------------|------------------|
| Grinding | SiC paper P 800 | Water | 4 | 15 |
| | SiC paper P 1200 | Water | 4 | 15 |
| | SiC paper P 2000 | Water | 4 | 15 - 30 |
| | SiC paper P 4000 | Water | 4 | 30 |
| Polishing | MD-Nap 1 μ m | Lubricant Blue | 30 | 15 - 30 |
| | MD-Chem OPS ^{*)} | - | 120 | 15 |
| Polishing cp TiGr2 | MD-Chem OPS ^{**)} | - | 8 | 15 |
| Etching with Kroll's reagent for 8 to 15 s of Ti6Al4V and Ti15Mo with: 91 ml distilled water, 6 ml nitric acid, 3 ml hydrofluoric acid | | | | |
| *) OPS consists of 50% OPS Non-dry and 50% distilled water | | | | |
| **) OPS consists of 98% OPS Non-dry and 2% hydrogen peroxide | | | | |

3.4.2 Light optical microscope

A ZEISS Axio Observer.Z1m microscope equipped with an AxioCam MRc5 camera was used for microstructure investigations of as-delivered, heat treated and EB structured specimens. Pictures of Ti15Mo and Ti6Al4V were taken in bright field mode, whereas polarized light was used for cp TiGr2. The weld seam shape as a function of the EB parameters for cp TiGr2, Ti6Al4V and Ti15Mo was analysed by the depth and width of bead on plates by measuring LOM pictures. The pictures of EB structured samples were taken in such a way that the cross section corresponded to the horizontal of the EB structure/EB bead on plate. LOM investigations of heat treated specimens were done near the thermocouples, to prevent incorrect phenomena due to the temperature gradient.

3.4.3 Scanning electron microscope

The scanning electron microscope was used for material investigations. The secondary electron detector (SE) of a Leo (ZEISS) 1450VP microscope was used to observe the topography of EB

structured surface using an acceleration voltage between 10 kV and 20 kV. SEM backscattered electron detector (BSE) investigations were done to reveal microstructural features. A Leo (ZEISS) 1450VP, a MIRA 3 (TESCAN) and a ZEISS (Auriga Compact) with an acceleration voltage between 10 kV and 20 kV were used.

3.4.4 Electron backscattered diffraction

EBSD measurements were carried out with a ZEISS (Auriga Compact) and a MIRA 3 (TESCAN) with step sizes of 0.1 μm for cp TiGr2 and 2 μm for Ti15Mo. The obtained data were treated using Orientation Imaging Microscopy Software (OIM).

3.4.5 Transmission electron microscope

TEM observations were performed on a JEOL 2200 FS microscope with an operating voltage of 200 kV. For TEM investigations, samples in form of a disc (investigations near to the hole) or FIB lamella were produced. The lamellae were prepared using a FIB device (consisting of a liquid metal ion source in a SEM, ZEISS, Auriga Compact).

3.5 Hardness

Hardness measurements were carried out using a EMCO Test (M10 010) with an indentation load of 0.1 kg (HV 0.1) and a dwell time of 15 s. Six to eight indentations were taken in the as-delivered, EB structured, heat treated and aged material and the average value was calculated to determine the mechanical properties.

3.6 Surface characterization

The surface characterization was divided into two steps. First, the shape of the created surface structure was qualitatively documented and evaluated by macroscopic pictures to determine inhomogeneities on the surface, and to choose a structure type for further investigations. Second, an Alicona InfiniteFocus microscope (IFM 2.0) was used to quantify the surface after the EB structuring process. The special focus variation technique allowed the 3D reconstruction of the observed profile. The EB structured samples were recorded with 10x and 50x objectives, with a maximal vertical resolution of 100 nm and 50 nm, respectively. The lateral resolution was 3 μm for lens of 10x and 2 μm for 50x. The groove shape was evaluated with a line profile at two positions on the surface (position 1 at 200 μm from the reference corner and position 2 at 600 μm from the reference corner) as illustrated in an acquired surface profile in Figure 39. The groove shape was determined with Δw for groove width and Δz for groove depth. Further, the pin height/wall depth were evaluated with a line profile through the centre of the structure, as indicated with the blue line in Figure 39. A list of investigated EB structured samples is given in Table 11.

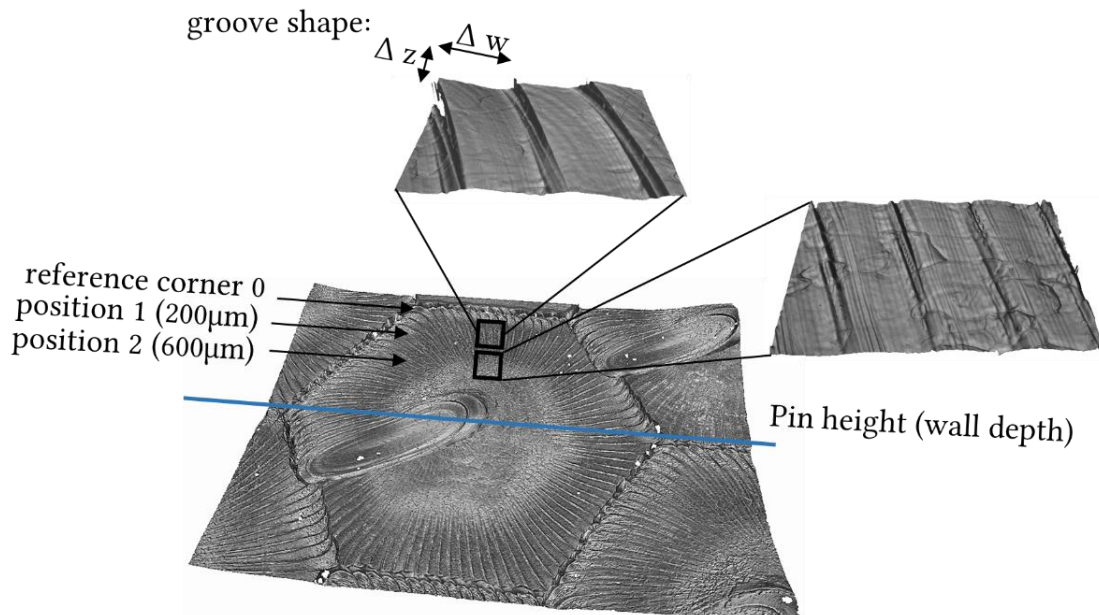


Figure 39. Example of 3D topography images of EB structure.

3.7 Cell investigations

3.7.1 Cell culture

Murine (MC3T3-E1) pre-osteoblast cells obtained from European collection of cell cultures (ECACC, Salisbury, UK, catalogue number 99072810) were applied for cell culture studies. This cell line was used to evaluate behaviours such as cell morphology and cell proliferation studies [92] [93]. Cells were cultured in Eagle's minimum essential medium (Sigma-Aldrich, Vienna, Austria) supplemented with 10 % fetal bovine serum, 100 U ml⁻¹ penicillin, 100µg ml⁻¹ streptomycin and 2 mM glutamine (all reagents Invitrogen, CA, USA) at 37 °C, 5 % CO₂ and 95 % humidity. Titanium alloy specimens were sterilized 1 hour under UV light (each side) and incubated for 15 min with 70 % ethanol. Before cell cultivation, samples were dried completely at room temperature. The cells were seeded on structured and non-structured (control) specimens, at a density of 10,000 cells/cm², for 6, 12, 24 and 48 h. Table 11 includes information about the material, machine- and deflection parameters used for the evaluation of cell morphology and cell spreading area.

3.7.2 Scanning electron microscope

To evaluate the cell morphology and cell spreading area of structured and control samples, the media was removed and specimens were rinsed in normal PBS (37 °C) for 5 min and fixed in 2 % PFA 2.5 % glutaraldehyde in a phosphate buffer pH=7.4 for 30 minutes. Subsequently, samples were rinsed in 0.1M P-buffer pH=7.4 and fixed with osmium tetroxide. Fixed samples

then were subjected to 30 %, 50 %, 70 %, 80 %, 90 % and 96 % alcohol dehydration for 15 min at room temperature, respectively. After dehydration in graded alcohol, specimens experienced critical point drying with BAL TEC CPD 030 (formerly BAL TEC, now Leica, Germany). Both structured and control specimens were then sputter-coated with gold palladium by using a SCD 050 Sputter Coater, BAL-TECH for 70 s at 20 mA. The cell spreading area, after different cultivation times, was evaluated by analysing BSE SEM images with the software AXIO VISIO (ZEISS). For evaluation, five images were taken at three positions: pin, structure and cross-over, as shown in Figure 40. A position represents a size of 2 mm². Furthermore, secondary electron (SE) SEM images were randomly taken to analyse the morphology of the cells at various cultivation times. For SE and BSE investigations a Leo (ZEISS) 1450VP microscope was used with an acceleration voltage of 10 kV or 15 kV.

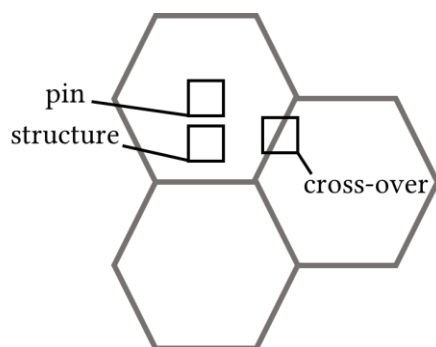


Figure 40. Schematic figure of positions to evaluate the cell spreading area.

4 Results

The obtained results after different energy inputs of EB bead on plate will be presented first. Then, the feasibility of the EB structuring with different parameter combinations (machine and figure parameter) will be shown. The change of roughness due to the EB structuring process will be summarized and evaluated. Furthermore, the influence of the EB process on the microstructural change of all investigated titanium alloys will be evaluated. The impact on additional heat treatments after the EB process on Ti6Al4V will be shown. Moreover, additional phase transformation of Ti15Mo after different heat treatments will be presented. The influence of different surface characteristics after the EB process on the biological behaviour will be shown with in vitro tests.

4.1 EB bead on plate

EB bead on plates were performed on cp TiGr2, Ti6Al4V and Ti15Mo to investigate the microstructure in the MZ and to analyse different EB parameters. The MZ was characterized by the depth and width. The change of the MZ was compared due to the different energy inputs per unit length. The energy input per unit length is generally known as $E = \frac{U \cdot I}{v}$, where U represents the acceleration voltage, I the beam current and v the deflection velocity. The deflection velocity was calculated as $\frac{L}{s}$, where L was the total length of the beam travel direction and s the total deflection time.

4.1.1 Modification of MZ (depth and width) after different EB parameter

The top view images of bead on plates on Ti6Al4V samples were evaluated as shown in Figure 41. Therefore, a first parameter set was applied with the lowest current of 0.8 mA and different velocities. Figure 41 (a) shows an experiment where the lowest energy input of $E = 178 \text{ J/m}$ ($I = 0.8 \text{ mA}$ and $v = 676 \text{ mm/s}$) was used. The material was not melted, determining that the used energy was not enough to melt the material on the surface. By reducing the velocity to the half and a quarter, the energy input was increased up to $E = 355 \text{ J/m}$ ($I = 0.8 \text{ mA}$ and $v = 338 \text{ mm/s}$) and $E = 710 \text{ J/m}$ ($I = 0.8 \text{ mA}$ and $v = 169 \text{ mm/s}$). Homogeneous bead on plate with apparent columnar grains shape can be observed, as shown in Figure 41 (b) and (d). A second parameter set with higher beam current ($I = 2.5 \text{ mA}$) and same velocities was investigated. Figure 41 (c) shows a bead on plate with an energy input of $E = 555 \text{ J/m}$ ($I = 2.5 \text{ mA}$ and $v = 676 \text{ mm/s}$) which evolved an apparent columnar grain shape and smooth solidification lines. Solidification lines were strong and distinct with an energy input of $E = 1109 \text{ J/m}$ ($I = 2.5 \text{ mA}$ and $v = 338 \text{ mm/s}$) and $E = 2219 \text{ J/m}$ ($I = 2.5 \text{ mA}$ and $v = 169 \text{ mm/s}$), as indicated with black arrows in Figure 41 (e) and (f).

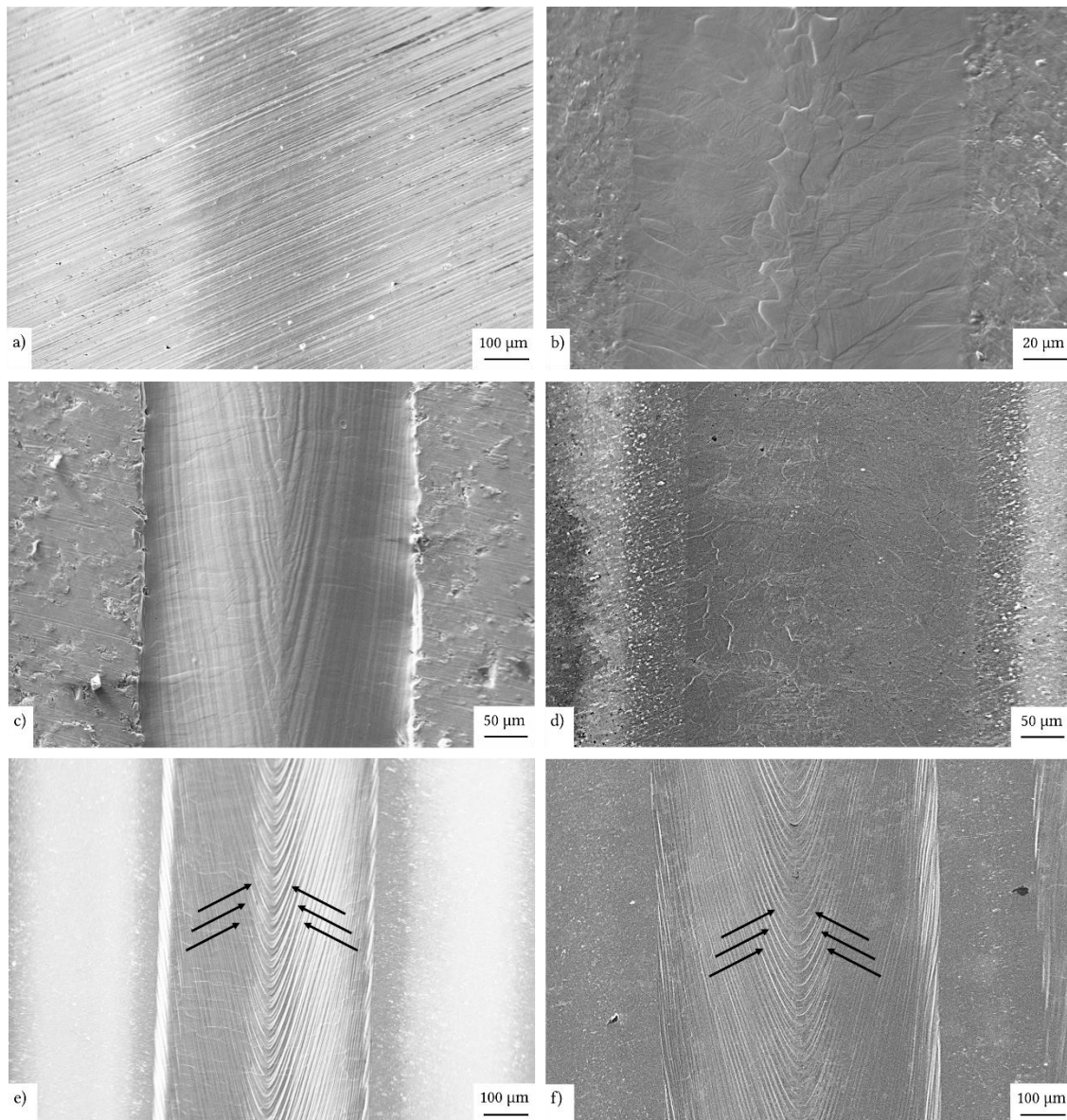


Figure 41. Top view of EB bead on plate with different energy inputs ($U = 150$ kV is constant) for a) $E = 178$ J/m ($I = 0.8$ mA, $v = 676$ mm/s), b) $E = 355$ J/m ($I = 0.8$ mA, $v = 338$ mm/s), c) $E = 710$ J/m ($I = 0.8$ mA, $v = 169$ mm/s), d) $E = 555$ J/m ($I = 2.5$ mA, $v = 676$ mm/s), e) $E = 1109$ J/m ($I = 2.5$ mA, $v = 338$ mm/s) and f) $E = 2219$ J/m ($I = 2.5$ mA, $v = 169$ mm/s).

Furthermore, the depth and width of the MZ were determined by different energy inputs per unit length on cp TiGr2, Ti6Al4V and Ti15Mo. The weld pool depth and width expanded by an increase of the energy input, as shown in Figure 42 and Figure 43.

The values of the depth increased by raising the energy input per unit length. The measuring points were suitable to the linear function and for all investigated titanium alloys, except for 335 J/m and 710 J/m (indicated with red arrows, Figure 42), where a greater deviation was observed due to the lower current used (0.8 mA). In case of measuring the width, a similar behaviour was observed. The values increased by raising the energy input per unit length and

followed the square root function. Similar to the investigations of the depth, the values of the width showed a greater deviation due to the use of 0.8 mA for 335 J/m and 710 J/m (indicated with red arrows in Figure 43).

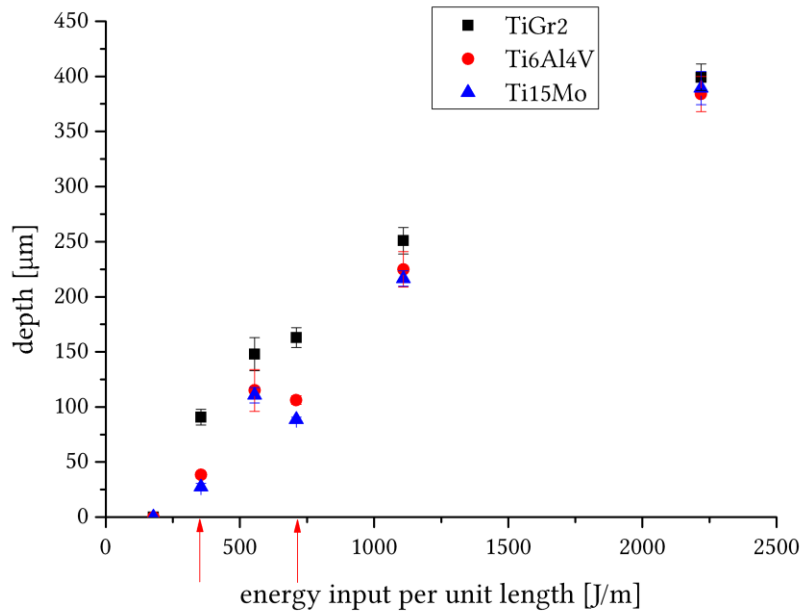


Figure 42. Depth of bead on plates after changing the energy input per unit length.

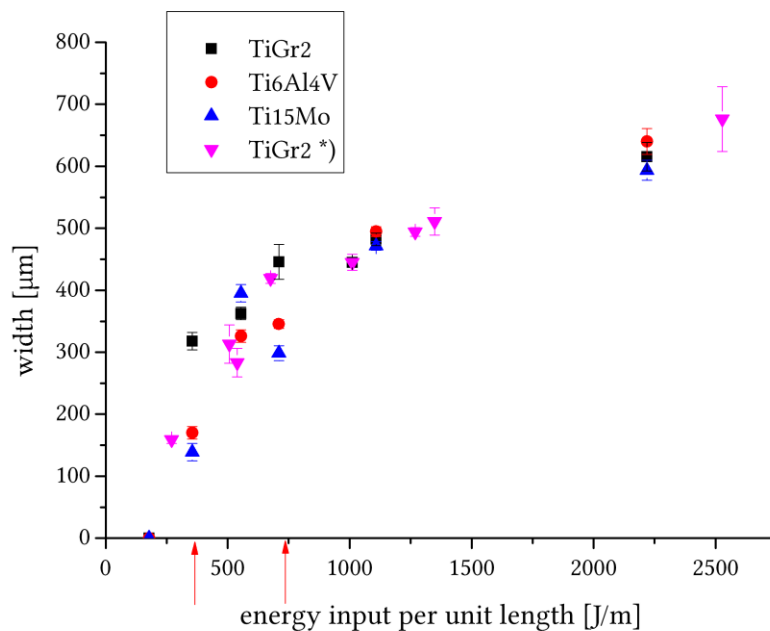


Figure 43. Width of bead on plate after changing the energy input per unit length. Values adapted from [94].

4.1.2 Microstructure investigations of cp TiGr2 after EB bead on plate

Figure 44 (a) and (b) show the LOM cross section images of cp TiGr2 bead on plate with two different energy inputs, namely $E = 355 \text{ J/m}$ and $E = 555 \text{ J/m}$, respectively. Due to the increase of the energy input, the width and depth of the MZ was enlarged. The cp TiGr2 samples did not show any well-defined heat affected zone. Therefore, the microstructure was divided into MZ and base material, as shown in Figure 44 (a) and (b). The MZ of the bead on plate of cp TiGr2 samples were similar for all observed experiments, and characterized by coarse, columnar and elongated grains. The grains tended to grow in the direction of the thermal gradient.

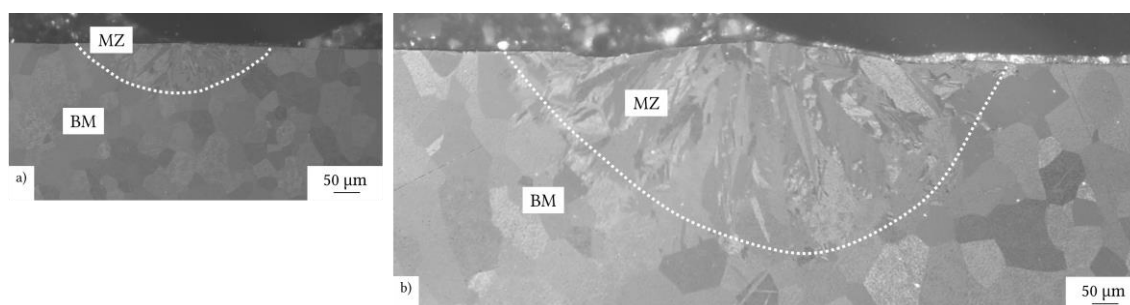


Figure 44. EB bead on plate cp TiGr2 ($U = 150 \text{ kV}$ is constant) for a) $E = 355 \text{ J/m}$ ($I = 0.8 \text{ mA}$, $v = 338 \text{ mm/s}$) and b) $E = 555 \text{ J/m}$ ($I = 2.5 \text{ mA}$, $v = 676 \text{ mm/s}$).

4.1.3 Microstructure investigations of Ti6Al4V after EB bead on plate

Figure 45 (a) and (b) compare the LOM cross section images of two different energy inputs, namely $E = 355 \text{ J/m}$ and $E = 555 \text{ J/m}$ on Ti6Al4V bead on plate, respectively. As a result of the increased energy input, the width and depth of the MZ was enlarged. Due to the microstructure change of Ti6Al4V after the EB process, the microstructure of all Ti6Al4V samples can be divided in three zones: the MZ, the HAZ and the base material, as shown in Figure 45. The prior β grains tended to columnar growth in the direction of the thermal gradient. The microstructure within the columnar grain was full martensitic (α') microstructure. The microstructure of the HAZ was a mixture of α' , primary α and β phase.

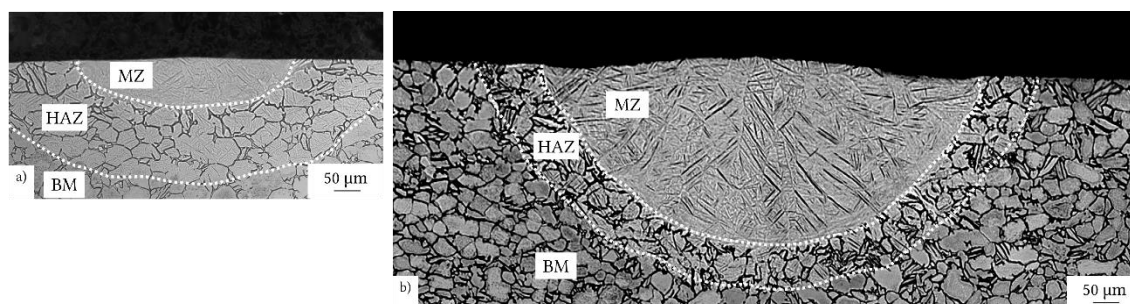


Figure 45. EB bead on plate on Ti6Al4V ($U = 150 \text{ kV}$ is constant) for a) $E = 355 \text{ J/m}$ ($I = 0.8 \text{ mA}$, $v = 338 \text{ mm/s}$) and b) $E = 555 \text{ J/m}$ ($I = 2.5 \text{ mA}$, $v = 676 \text{ mm/s}$).

4.1.4 Microstructure investigations of Ti15Mo after EB bead on plate

Figure 46 (a) and (b) show the LOM cross section images of Ti15Mo bead on plate with two different energy inputs, namely $E = 355 \text{ J/m}$ and $E = 555 \text{ J/m}$, respectively. As a result of the increased energy input, the width and depth of the MZ was enlarged. The microstructure investigations on Ti15Mo did not show any well-defined heat affected zone. Therefore, the microstructure was divided into two zones: the molten zone and the base material, as shown in Figure 46. The microstructure of the MZ of all Ti15Mo consisted of elongated columnar β grains, with a dendritic cellular microstructure. The growth of the grains was in the direction of the thermal gradient.

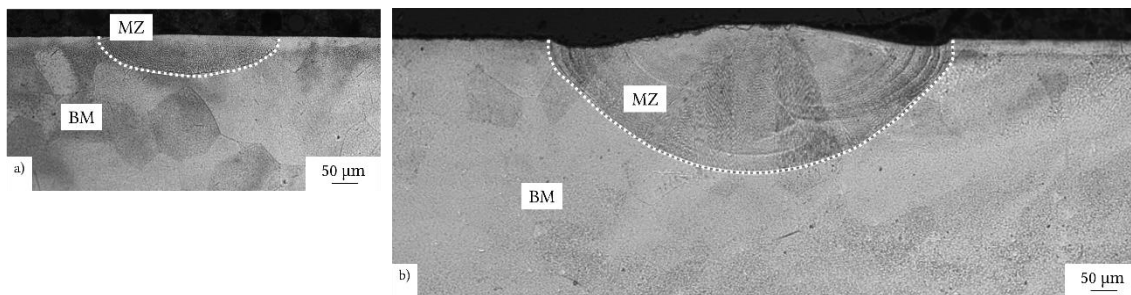


Figure 46. EB bead on plate on Ti15Mo ($U = 150 \text{ kV}$ is constant) for a) $E = 355 \text{ J/m}$ ($I = 0.8 \text{ mA}$, $v = 338 \text{ mm/s}$) and b) $E = 555 \text{ J/m}$ ($I = 2.5 \text{ mA}$, $v = 676 \text{ mm/s}$).

4.2 EB structuring

The machine parameters (voltage, current and velocity of the beam) for the EB structuring were based on the results of bead on plate. As mentioned before, the voltage was kept constant at 150 kV and two different values for the current (0.8 mA and 2.5 mA) were used. Therefore, the energy input of $E = 355 \text{ J/m}$ ($I = 0.8 \text{ mA}$ and $v = 338 \text{ mm/s}$) and $E = 710 \text{ J/m}$ ($I = 0.8 \text{ MA}$ and $v = 169 \text{ mm/s}$) were chosen for further investigations.

4.2.1 EB parameter combinations

Polygon figures

Figure 47 shows the feasibility of different polygon figures. Polygons of triangular, square and hexagonal shaped deflection figures were arranged adjacent to each other. Hexagons formed a honeycomb structure, which showed a better connectivity between the figures compared to triangular and square shaped figures, as indicated with the red lines. Therefore, the present work concentrated on the hexagonal arrangement of surface structuring. The oval forms (one for each structure – representative) mark the start/end position of the structuring process. The shape of the oval form is typical for welding processes [66], and the width was limited to the achievable beam focus, estimated for this work between $0.3 - 0.4 \text{ mm}$.

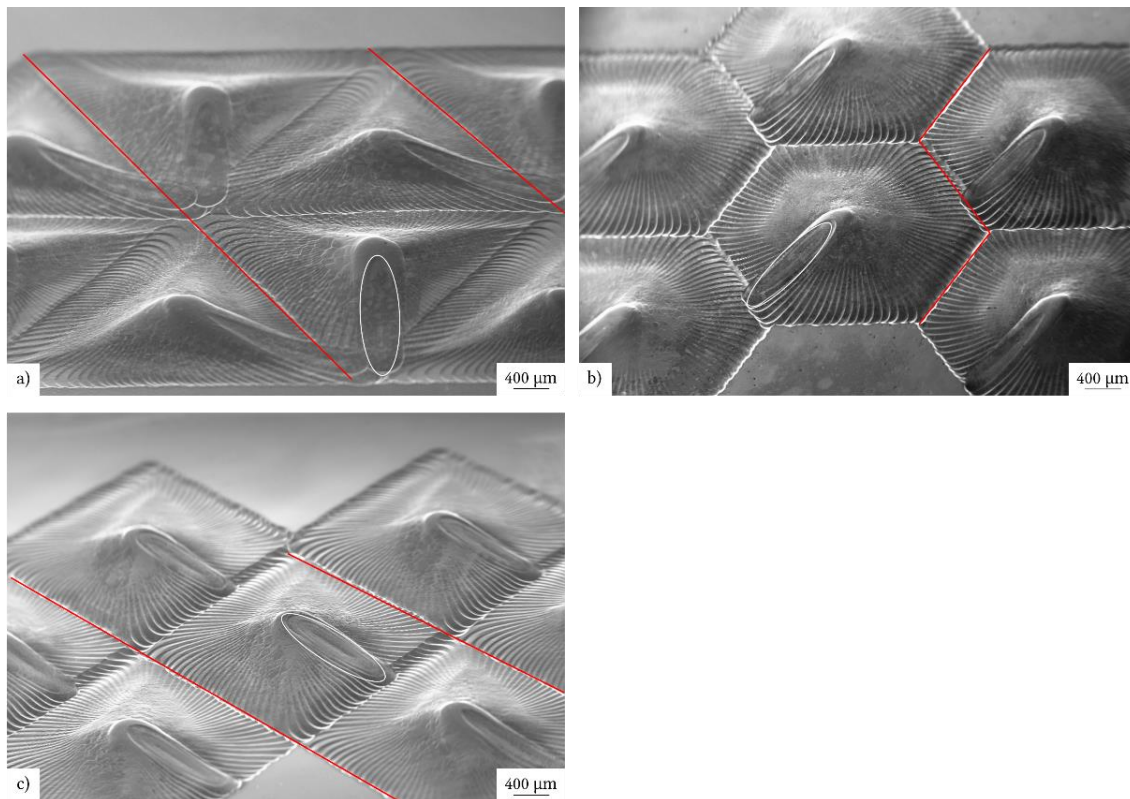


Figure 47. EB structuring on Ti6Al4V of different deflection figures for a) triangular 4/2 pin array with 99 arms produced with $I = 2.5$ mA and $v = 697$ mm/s, b) hexagonal 2/4 pin array with 96 arms produced with $I = 2.5$ mA and $v = 676$ mm/s and c) square 3/3 pin array with 100 arms produced with $I = 2.5$ mA and $v = 715$ mm/s.

Figure orientation

By changing the figure orientation, the beam movement along the arms was changed, as explained in section 2.4.1. The material transport for creating pin arrays occurred from the perimeter to the centre of the border, as indicated by the arrows in Figure 48 (a). An intrusion along the perimeter was observed, as shown in Figure 48 (c). For the wall array, it is the other way around, as the material was shifted from the centre to the border, as indicated by the arrows in Figure 48 (b). A protrusion along the perimeter was observed, as shown in Figure 48 (d).

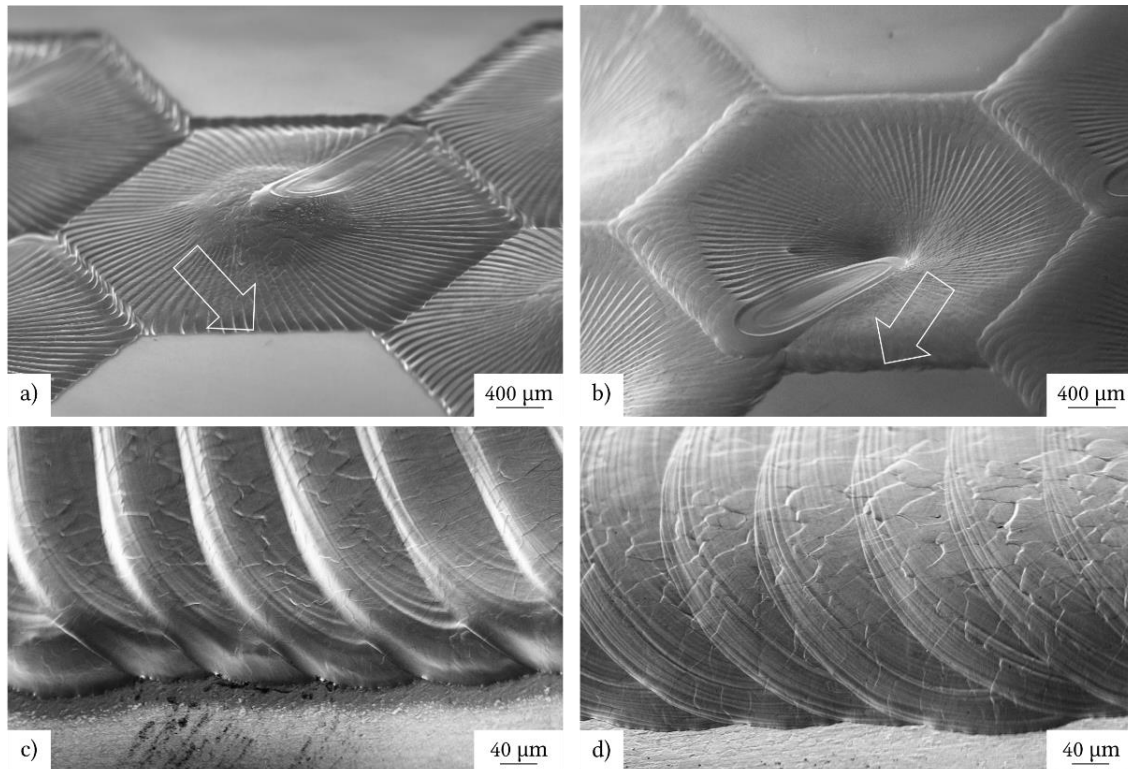


Figure 48. EB structuring of hexagonal structure on Ti6Al4V by changing the figure orientation for a) pin array, b) wall array, c) detail pin array and d) detail wall array. $I = 2.5$ mA and $v = 697$ mm/s.

Arm numbers

Figure 49 shows a pin array with a hexagonal shape and two different sets of arm numbers, namely 126 and 156 arms. By comparing the details in Figure 49 (c) and (d), the beam overlap was increased, and therefore the travel distance between every single arm increased. The beam overlap, or travel distance, between every single arm directly depended on the number of arms.

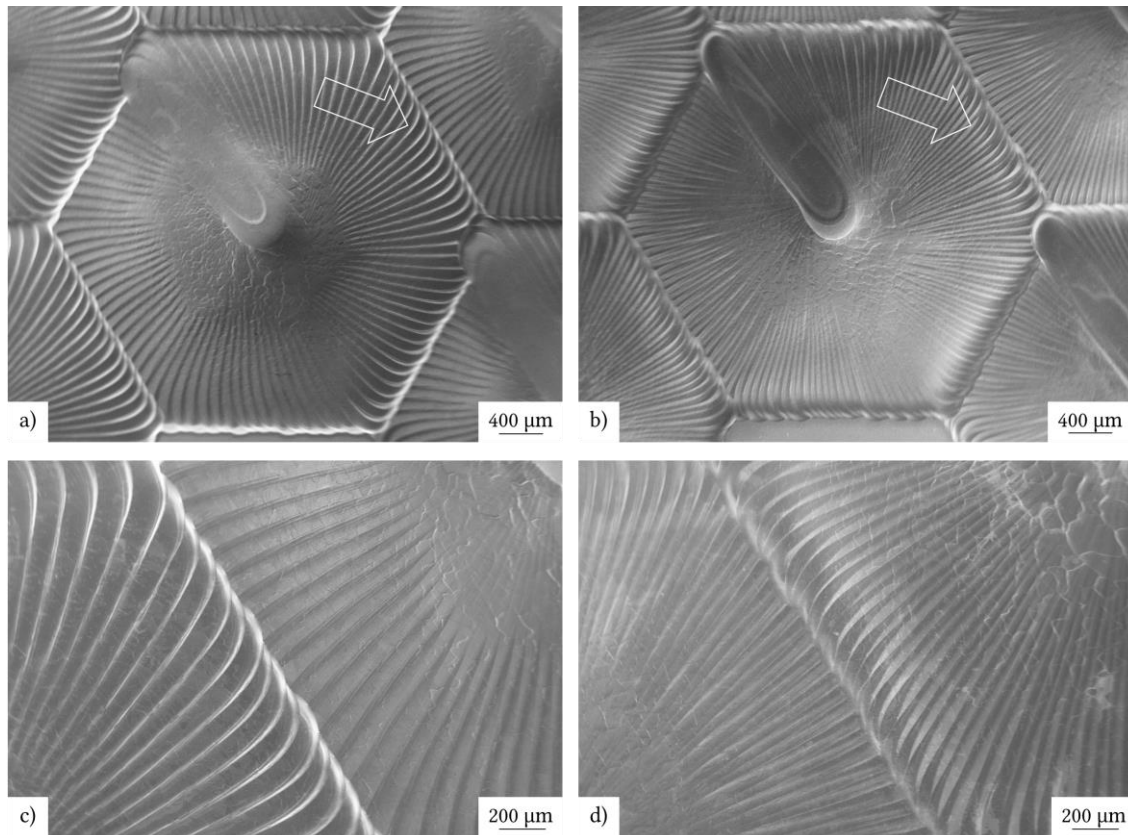


Figure 49. EB structuring of a hexagonal pin array structure on Ti6Al4V by changing the arm number for a) pin 126 arm, b) pin 156 arm, c) detail 126 and arm d) detail 156 arm. $I = 2.5$ mA and $v = 697$ mm/s.

Energy input

Figure 50 shows hexagonal structures with different energy input. The energy input (determined by voltage, current and velocity) was directly dependent on the displacement of molten material. Therefore, a change in the surface roughness was evident. The change of surface roughness as related to groove shape (width and height) and pin height is described in section 4.2.2. Hereinafter, the structure with the lower energy is termed as the smoother structure.

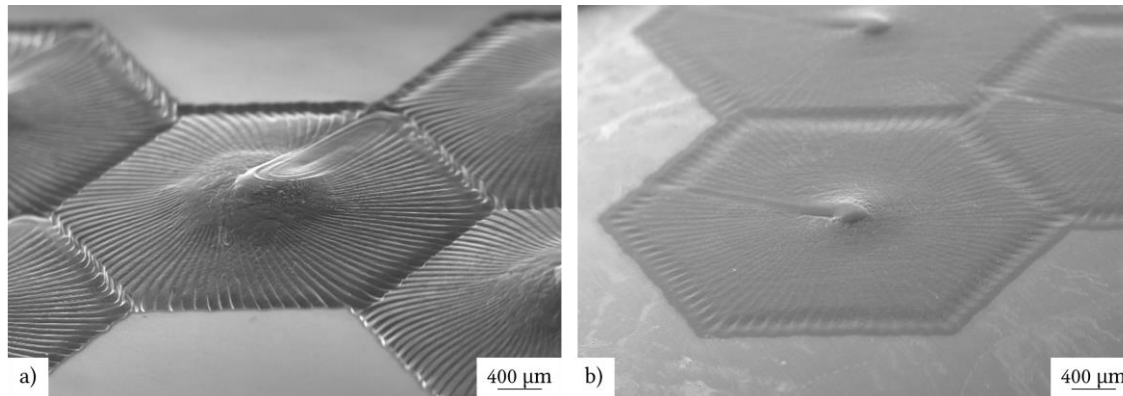


Figure 50. EB structuring of hexagonal pin structure on Ti6Al4V by changing the energy input for a) $I = 2.5$ mA and $v = 697$ mm/s and b) $I = 0.8$ mA and $v = 341$ mm/s.

Materials

The difference between cp TiGr2, Ti6Al4V and Ti15Mo after EB surface structuring of a hexagonal shape can be observed in Figure 51. Cp TiGr2 trends to generate a martensitic structure, as indicated on the surface, and shown in Figure 51 (b).

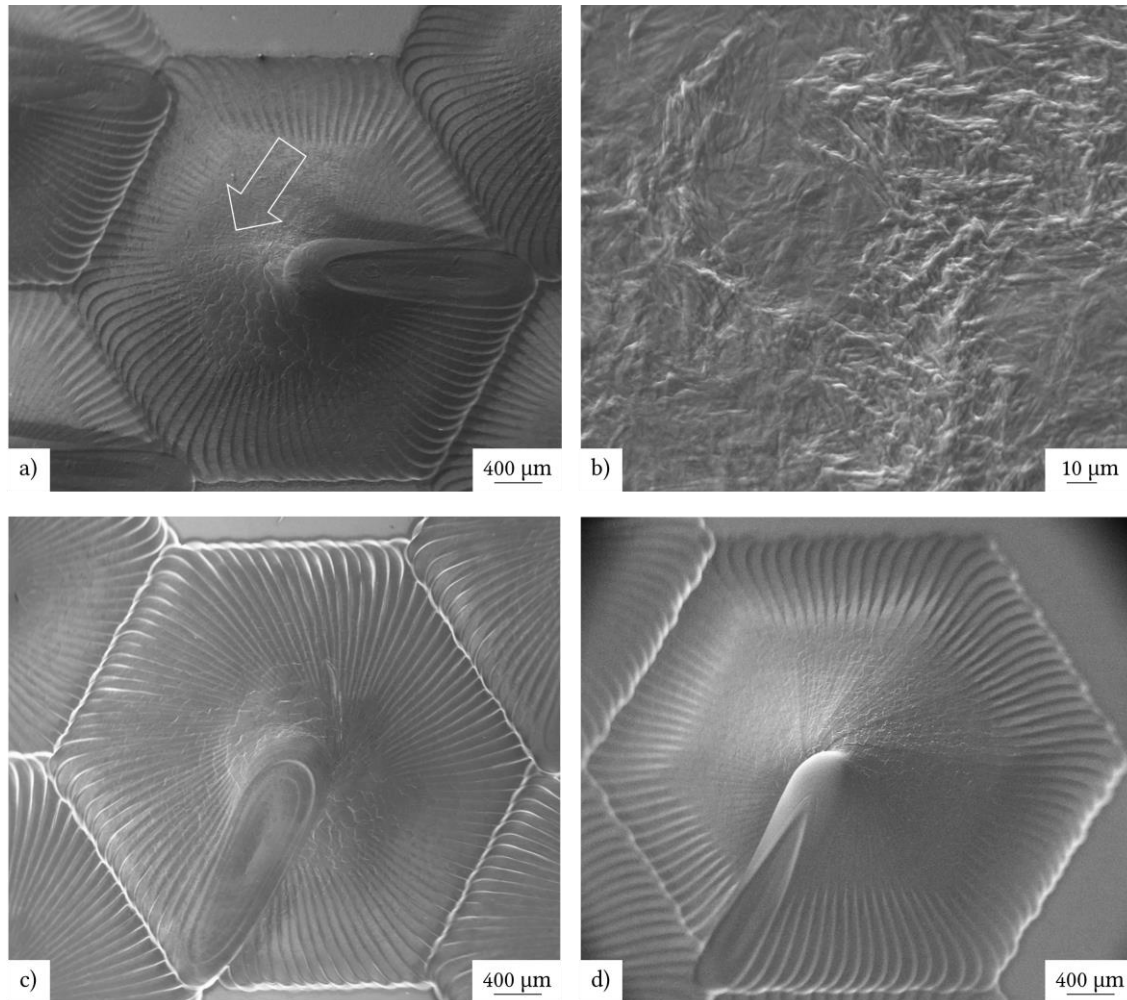


Figure 51. EB structuring of hexagonal pin array on a) cp TiGr2, b) Detail cp TiGr2, c) Ti6Al4V and d) Ti15Mo. $I = 2.5\text{mA}$ and $v = 697\text{ mm/s}$.

4.2.2 Surface roughness measurement

Table 13 gives a summary of the surface roughness measurements after three different conditions of EB structuring. The shape orientation (pin or wall structure) with the same energy input, and two different energy inputs, are compared. The topography values include the pin height/wall depth and the groove shape, including the depth (Δz) and width (Δw) of the groove.

Comparing different energy inputs reveals lower topography values for EB structuring with lower energy input, for all titanium alloys. The width of the groove shape increased along the length to the perimeter of the figure due to the overlapping distance of the arm.

The comparison between the shape orientation (pin and wall structure) with the same energy input exhibits significant differences of the surface roughness values for all titanium alloys. Therefore, the value of the wall depth was higher than the pin height due to a combination of “keyhole” effect, beam travel and overlapping of arms.

For pin array structures, the beam started for each arm in the centre of the figure and moved towards the perimeter. The overlapping of arms and the “keyhole” effect helped to remove the material from the perimeter of the figure, as shown in Figure 23 (a). Furthermore, the concentration of dragged material was found in the centre of the figure at very high temperatures, promoting the flow of the material during solidification. This was perceived as a smooth area; e.g. compare Δz pin with $1.7\mu\text{m}$ and Δz wall with $0.7\mu\text{m}$ of cp TiGr2.

In the case of wall array structures, the material movement was the other way around. The beam started for each arm along the perimeter of the figure and moved towards the centre (Figure 23 (b)). The material was removed from the centre along the perimeter of the figure and was well distributed (Figure 48 (b)).

Furthermore, the values of the canal depth for wall structures along the beam travel direction from position 1 to position 2 decreased due to the same reason as described above, while for pin structures it was the other way around.

The values of the groove depth for the wall structure along the beam travel direction from position 1 to position 2 decreased, while for pin structures it was the other way around. The width of the groove shape for all figure types depended on the energy input and the overlapping alteration.

Table 13. Surface roughness measurement for cp TiGr2, Ti6Al4V and Ti15Mo after EB structuring.

| Material | Beam current | Beam velocity | Beam travel direction | Pin height Wall depth | Position 1 200 μm from the reference | | Position 2 600 μm from the reference | |
|----------|--------------|---------------|-----------------------|--------------------------|---|---------------|---|---------------|
| | mA | mm/s | | | Δz | Δw | Δz | Δw |
| | | | | μm | μm | μm | μm | μm |
| TiGr2 | 0.8 | 341 | pin | 90 | 2.5 | 113.1 | 1.1 | 82.2 |
| Ti6Al4V | 0.8 | 341 | pin | 93 | 4.4 | 119.7 | 1.3 | 84.2 |
| Ti15Mo | 0.8 | 341 | pin | 47 | 0.8 | 84.3 | 0.6 | 61.6 |
| TiGr2 | 2.5 | 697 | pin | 305 | 4.9 | 85.5 | 1.7 | 78.5 |
| Ti6Al4V | 2.5 | 697 | pin | 298 | 9.0 | 82.3 | 4.0 | 68.6 |
| Ti15Mo | 2.5 | 697 | pin | 284 | 6.3 | 107.7 | 2.4 | 61.6 |
| TiGr2 | 2.5 | 697 | wall | 252 | 1.7 | 104.9 | 0.7 | 82.5 |
| Ti6Al4V | 2.5 | 697 | wall | 452 | 3.2 | 105.7 | 2.3 | 81.8 |
| Ti15Mo | 2.5 | 697 | wall | 238 | 1.5 | 108.0 | 1.3 | 78.2 |

4.3 Microstructure evolution after EB structuring process and additional heat and aging treatments

The energy input during EB structuring process creates a melt pool on the surface, and the solidification forms a homogenous gradient of microstructure. The gradient of microstructure change was independent of the deflection figure and free of defects for cp TiGr2, Ti6Al4V and Ti15Mo. The dimension of the different zones, namely MZ, HAZ and BM, were dependent on the beam current and velocity, as shown in section 4.1.1.

4.3.1 Commercial pure TiGr2

The cross section in Figure 52 was taken perpendicular to the structured surface, and it shows the macrostructure of cp TiGr2 after the EB structuring process. The heat input during the EB structuring process formed a gradient of microstructure. A difference between the MZ and the HAZ cannot be distinguished, and therefore the microstructure was divided into two zones:

MZ and BM. No defects in the macrostructure and microstructure were observed after the EB process, such as porosity and cracks.

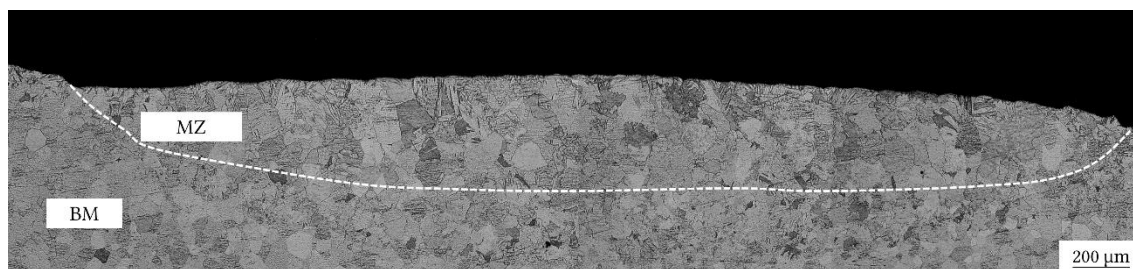


Figure 52. LOM image from a typical cross section of a hexagonal pin array on cp TiGr2 sample. $I = 2.5$ mA and $v = 697$ mm/s.

The grain growth in the MZ was similar to the weld seam of the bead on plate, but consisted of fewer columnar grains, more coarse grains and some martensitic laths, as shown in Figure 53. The hardness of the MZ ($189 \text{ HV} \pm 22$) was 13 % higher when compared to the BM ($164 \text{ HV} \pm 11$).

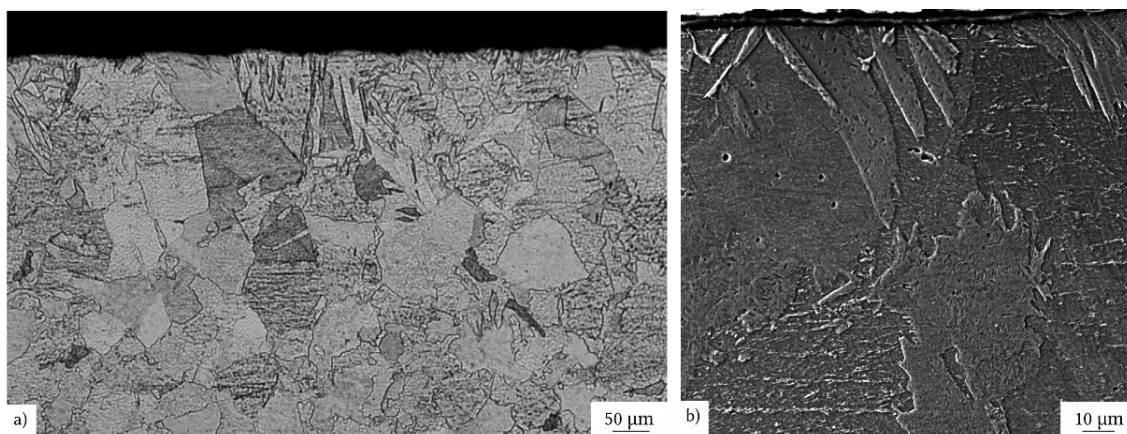


Figure 53. Detail of the white rectangular from Figure 52 for a) LOM image and b) SEM/SE image.

4.3.2 Ti6Al4V

The cross section in Figure 54 was taken perpendicular to the structured surface, and it shows the macrostructure after the EB structuring process for Ti6Al4V. Due to the heat input during the EB process, a gradient of microstructure is formed. According to the difference in the microstructure, it can be generally divided into three distinct zones, the MZ, HAZ and BM. No defects, such as porosity and cracks after the EB process, were observed in the macrostructure and microstructure.

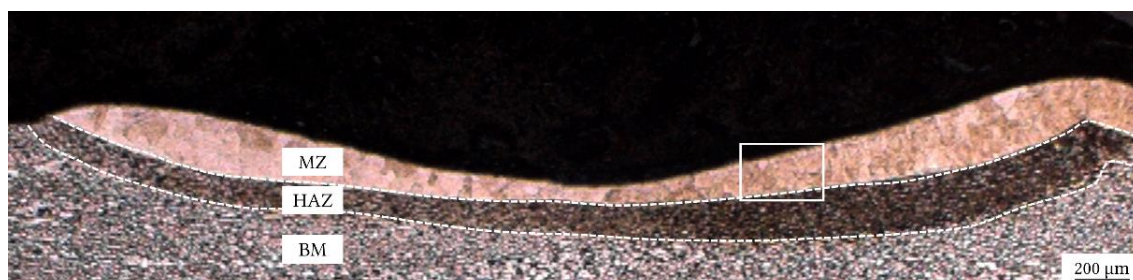


Figure 54. LOM image from a typical cross section of a hexagonal wall array on Ti6Al4V sample. $I = 2.5 \text{ mA}$ and $v = 697 \text{ mm/s}$.

The grain growth in the MZ was similar to the bead on plates. The growth of prior β grains started at the fusion line, and did not show an epitaxial growth (growth related to the HAZ zone), as indicated by the blue arrows in Figure 55. Furthermore, the prior β grain grew in the direction of the thermal gradient (as indicated by the red lines in Figure 55) through many arm rotations, where the growth was related to the previous layer.



Figure 55. Magnified LOM image of the white rectangular region near to the centre of a wall array shown in Figure 54.

The microstructure of the MZ, as shown in Figure 56 (a), consisted of a non-equilibrium martensitic α' structure with a hardness of $449 \text{ HV} \pm 23$, which was 109 HV higher than the value for the BM ($340 \text{ HV} \pm 14$). The HAZ, as shown in Figure 56 (b), represents a mixture of martensitic α' structure, primary α and β phase.

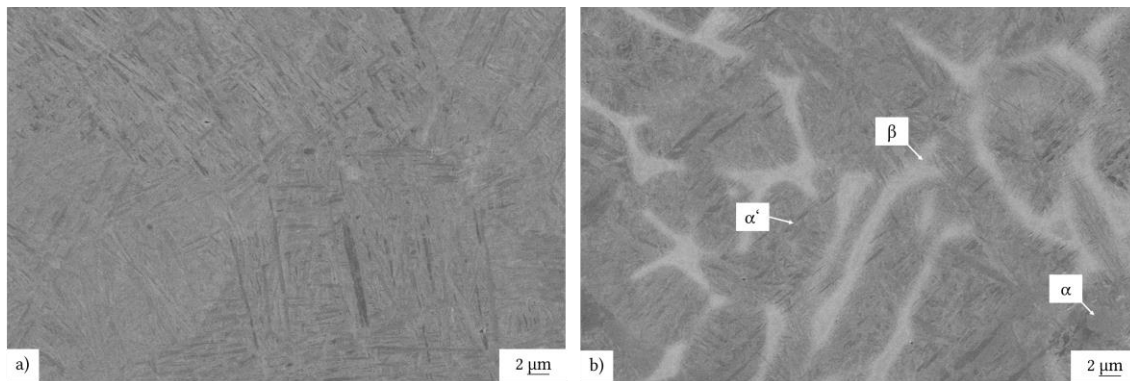


Figure 56. BSE-SEM image of Ti6Al4V after EB structuring of a hexagonal wall array for a) MZ and b) HAZ. $I = 2.5 \text{ mA}$ and $v = 697 \text{ mm/s}$.

The evolution of the martensite in the MZ after heat treatments at $650 \text{ }^\circ\text{C}$ and $720 \text{ }^\circ\text{C}$ for 2 h and 8 h is shown in Figure 57. At $650 \text{ }^\circ\text{C} / 2 \text{ h}$, the martensitic lath coarsened slightly, and a part transformed into β phase. The white spots are β phase, and were delineated by the martensitic lath, as indicated by the red arrow in Figure 57 (a) – (d). The evolution of the microstructure after $720 \text{ }^\circ\text{C} / 2 \text{ h}$ shows coarser martensite and a further increment of β phase, compared to $650 \text{ }^\circ\text{C} / 2 \text{ h}$. An increase of aging time up to 8 h did not show any significant difference for $650 \text{ }^\circ\text{C}$, but after $720 \text{ }^\circ\text{C} / 8 \text{ h}$ the microstructure revealed an increase of β phase, compared to the post heat treatment at $720 \text{ }^\circ\text{C} / 2 \text{ h}$. The microstructure after the heat treatments shows a clear effect of element partitioning, where the martensite was stabilized in very fine α lamellae and β phase. The associated hardness values are illustrated in Figure 58. The hardness after post heat treatment at $650 \text{ }^\circ\text{C}$ and $720 \text{ }^\circ\text{C}$ for 2 h and 8 h showed a slight decrease compared to the MZ.

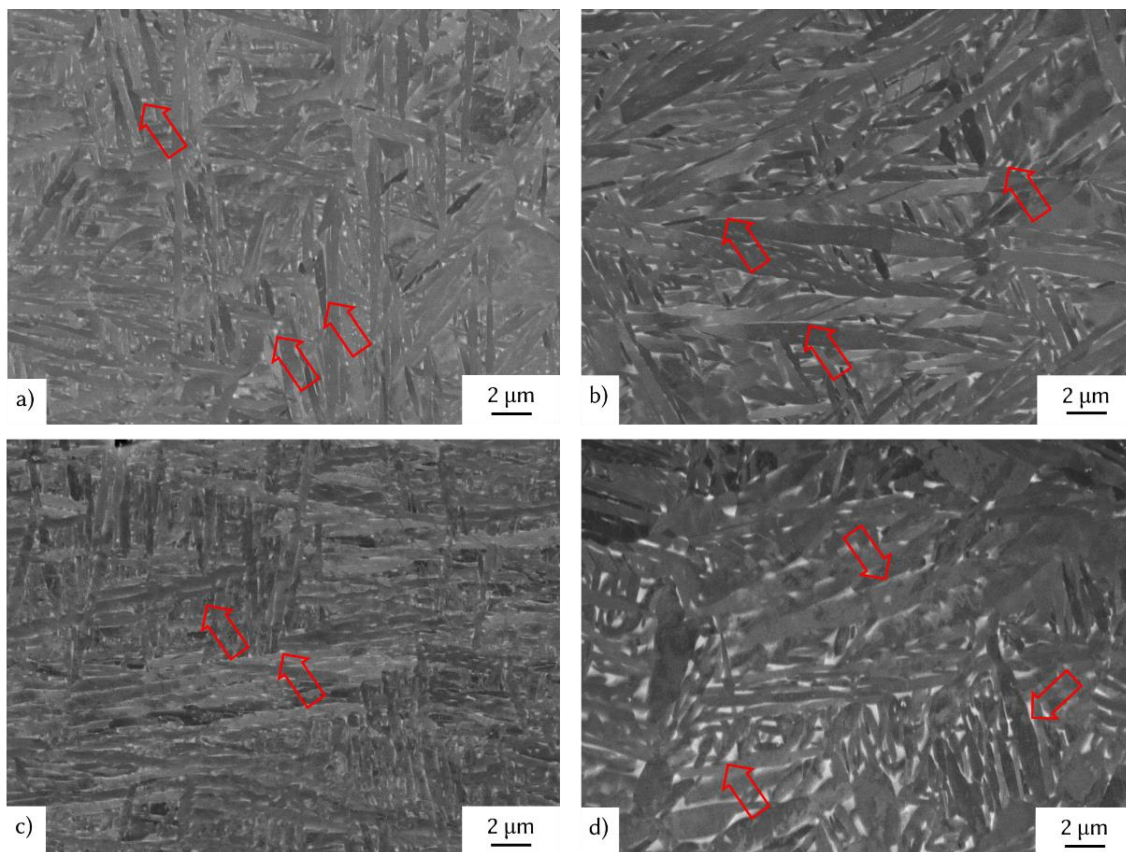


Figure 57. BSE-SEM images of the MZ after heat treatments at a) 650 °C / 2 h, b) 720 °C / 2 h, c) 650 °C / 8h and d) 720 °C / 8h. Brighter zones are β phase and dark areas denote α phase.

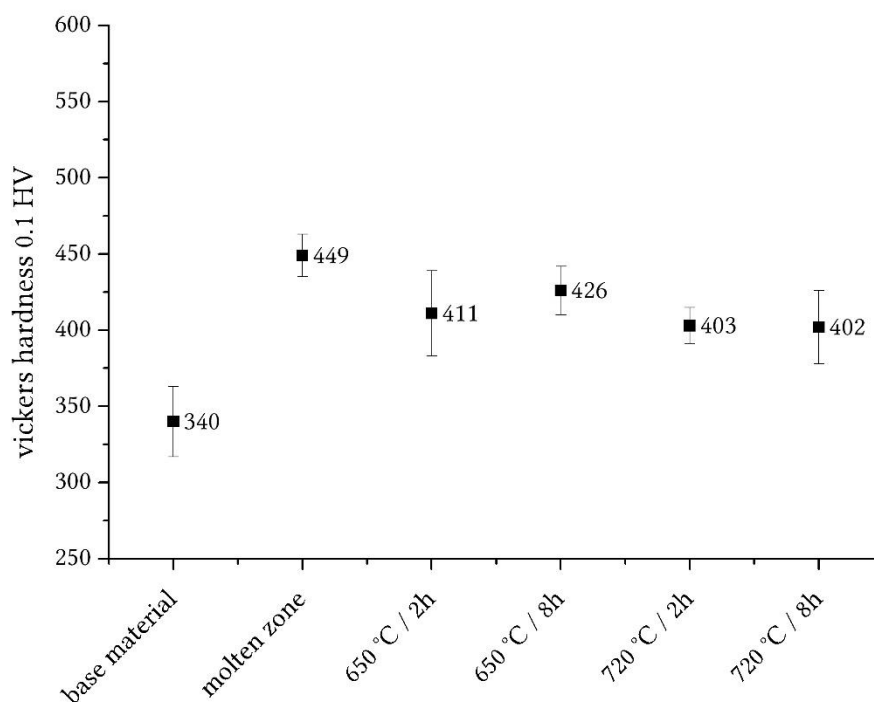


Figure 58. Vickers hardness values of Ti6Al4V after EB structuring and post heat treatments.

4.3.3 Ti15Mo

4.3.3.1 Investigation on the base material Ti15Mo

Investigations of the Ti15Mo base material were performed in order to obtain information about phase transformations during different heating rates. Figure 59 to Figure 62 display dilatometry data, where the change of length for different heating rates as a function of temperature are shown.

For all heating rates, the curves have a linear behaviour, due to the linear volume expansion of the material. The temperature range where the divergence from the linear growth is observed are different for all heating rates. All heating rates indicate a reduction and expansion of the volume, which indicates that diffusion-controlled processes occurred in the material, and impacted the volume.

For the heating rates of 5 K/min (Figure 59), 100 K/min (Figure 60), 200 K/min (Figure 61) and 300 K/min (Figure 62), the first temperature where a reduction of the volume expansion occurred was between 250 °C and 350 °C, 280 °C and 450 °C, 290 °C and 450 °C, 400 °C and 500 °C, respectively. The second temperature range where an increase of the volume expansion occurred was between 350 °C and 560 °C for 5 K/min, 450 °C and 560 °C for 100 K/min, 450 °C and 560 °C for 200 K/min and 500 °C and 560 °C for 300 K/min.

To obtain information about phase transformations and the aging response of Ti15Mo with a heating rate of 300 K/min, continuous heating up to 400 °C, 500 °C and 540 °C, or isothermal heating for 8 h at this temperature, were carried out.

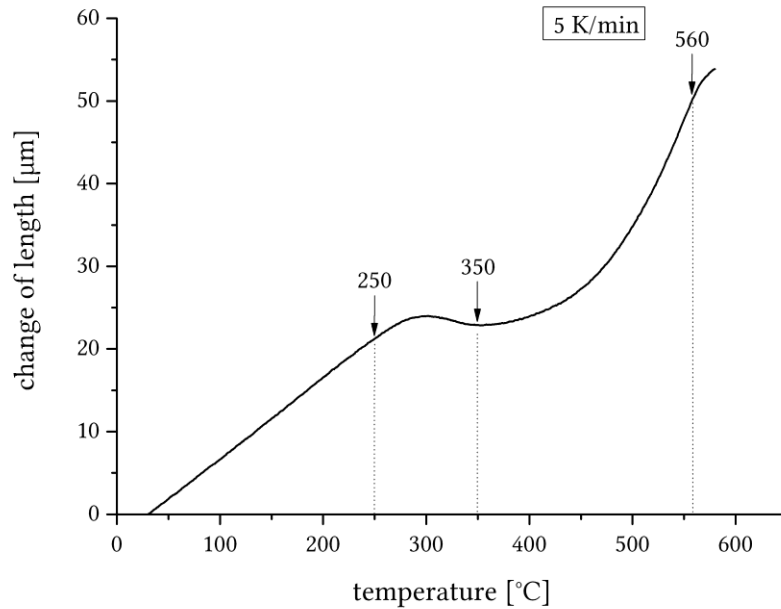


Figure 59. Dilatometry curve for Ti15Mo with 5 K/min heating rates up to 580 °C.

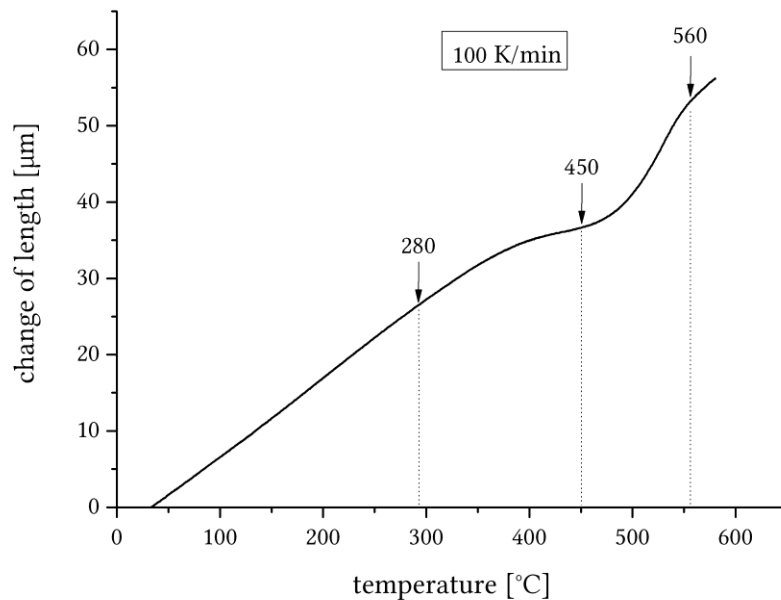


Figure 60. Dilatometry curve for Ti15Mo with 100 K/min heating rates up to 580 °C.

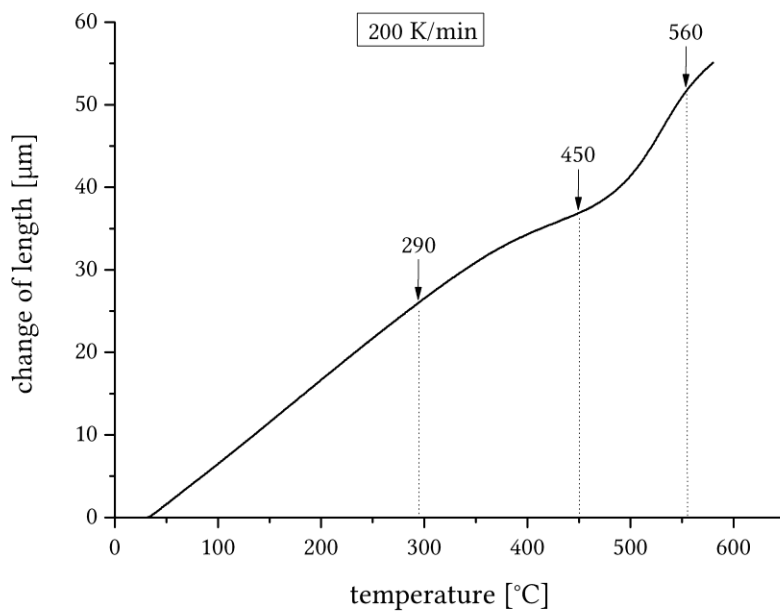


Figure 61. Dilatometry curve for Ti15Mo with 200 K/min heating rates up to 580 °C.

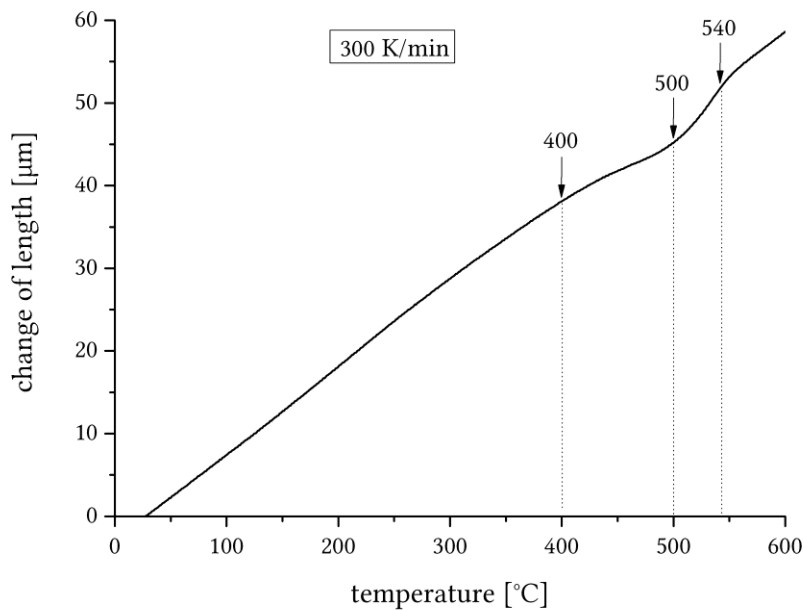


Figure 62. Dilatometry curve for Ti15Mo with 300 K/min heating rates up to 580 °C.

Additional hardness measurements showed higher hardness values for a heating rate of 5 K/min, compared to the values from 100 K/min to 300 K/min, as listed in Table 14.

Table 14. Vickers hardness values after different heating rates up to 580 °C

| heating rate | hardness value |
|--------------|----------------|
| [K/min] | |
| 300 | 312 ±11 HV |
| 200 | 310 ±18 HV |
| 100 | 315 ±18 HV |
| 5 | 347 ±19 HV |

Figure 63 shows the hardness values obtained for Ti15Mo samples after continuous heating and isothermal holding, compared to the as-delivered and solution-treated conditions. The α precipitation, and thus mechanical properties, were sensitive to the cooling condition [95]. Therefore, the as-delivered hardness value was slightly higher compared to the β solution treated. The hardness value for 400 °C (317 ± 22 HV) was similar to the β solution treated condition (317 ± 19 HV). No phase transformation occurred up to this temperature. The peak hardness value of 392 ± 32 HV was achieved at 500 °C. For heating up to 540 °C, the hardness decreased to 325 ± 25 HV. An increase in the hardness was observed for all isothermal aged samples, compared to the quenched samples during heating. The hardness after isothermal treatment at 400 °C resulted in 411 ± 67 HV. The highest hardness value of 438 ± 15 HV was achieved at 500 °C, while a hardness reduction was observed after isothermal aging at 540 °C for 8 h (339 ± 13 HV).

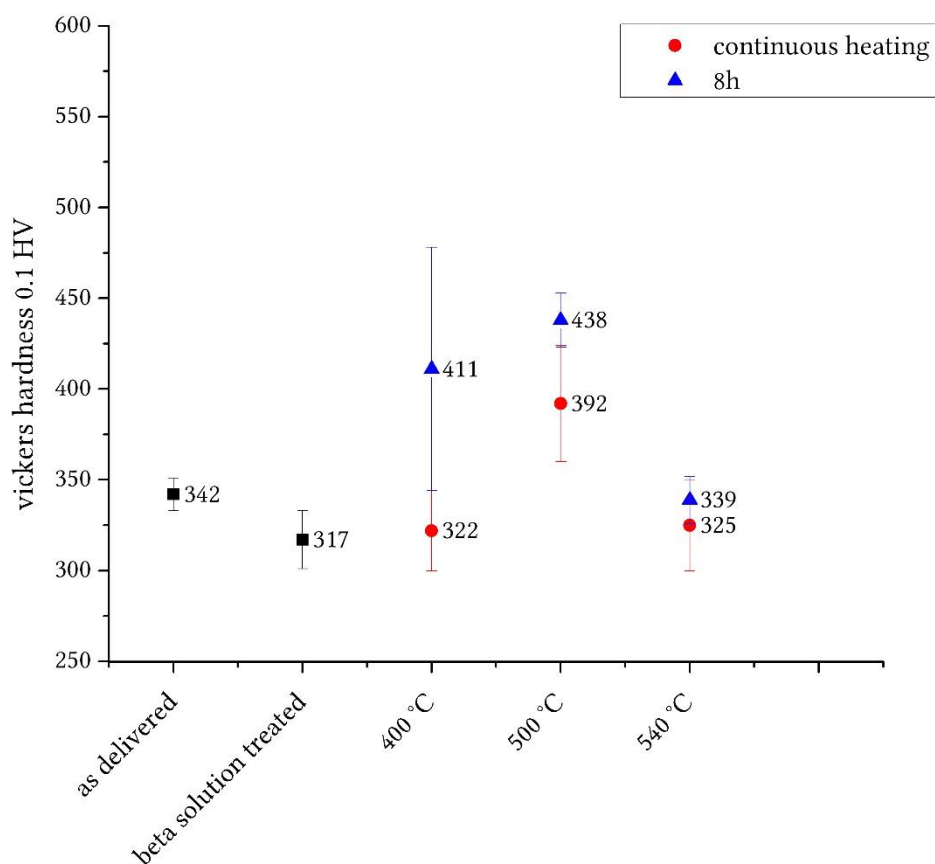


Figure 63. Vickers hardness values of Ti15Mo samples after continuous heating and isothermal treatment.

SEM investigations on continuously heated (500 °C and 540 °C) and isothermally aged (400 °C / 8h) samples could not provide all the details regarding the microstructure and phase formation. For this purpose, TEM was carried out.

Figure 64 (a) shows the dark field image of samples with continuous heating up to 500 °C, and the corresponding diffraction pattern with an electron beam parallel to $[110]_{\beta}$ in Figure 64 (b). The presence of ellipsoidal ω phase, with a size between 10 nm to 20 nm, is clear and indicated in Figure 64 (a).

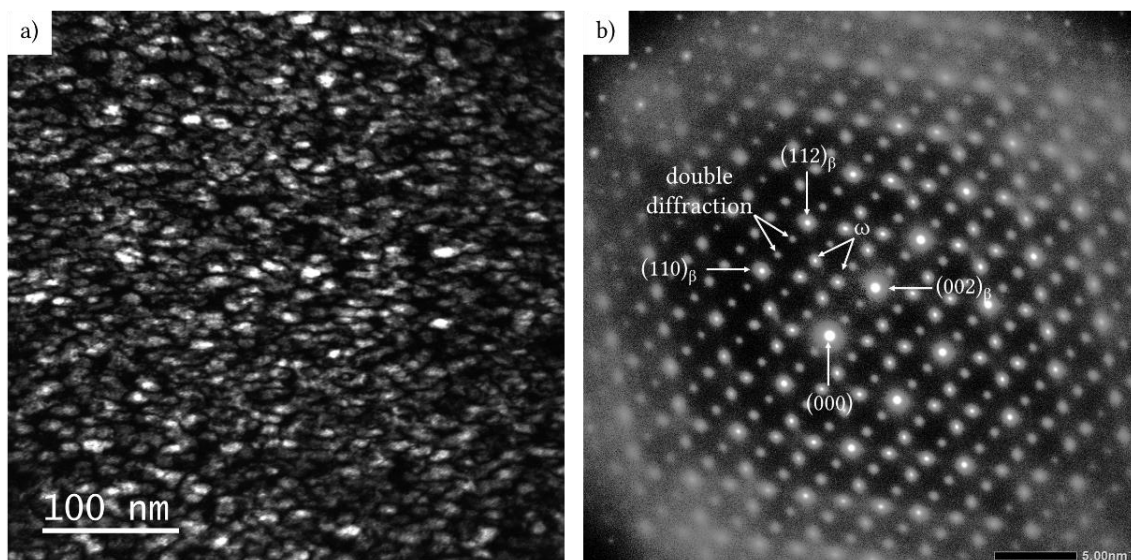


Figure 64. a) Dark field image of ω phase in the sample after continuous heating up to 500 °C and b) corresponding energy filtered SAD pattern with electron beam parallel to $[110]_{\beta}$.

The dark field image and corresponding diffraction pattern with the electron beam parallel to $[110]_{\beta}$ in Figure 65 shows the presence of ω phase after continuous heating up to 540 °C.

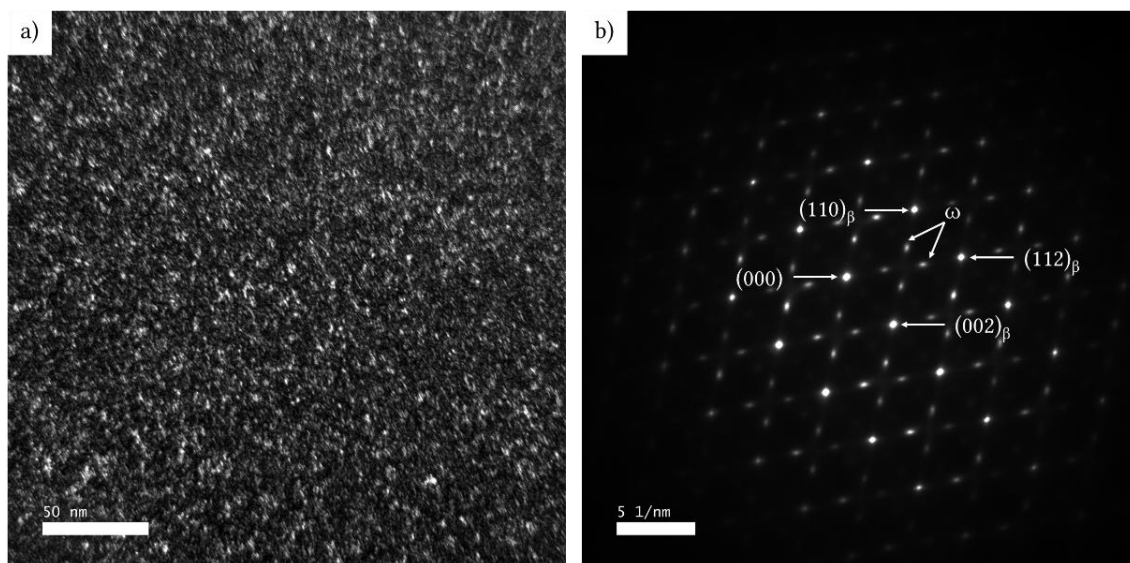


Figure 65. a) Dark field image of ω phase in the sample after continuous heating up to 540 °C and b) corresponding SAD pattern with electron beam parallel to $[110]_{\beta}$.

Figure 66 (a) shows the dark field image of isothermally aged sample at 400 °C / 8h, and the diffraction pattern with an electron beam parallel to $[110]_{\beta}$ is in Figure 66 (b). The dark field image shows ellipsoidal shaped ω phase, with a size between 10 nm to 20 nm. In the SAD pattern, a relatively weak streak was also observed, which could indicate the presence of a small amount of α phase.

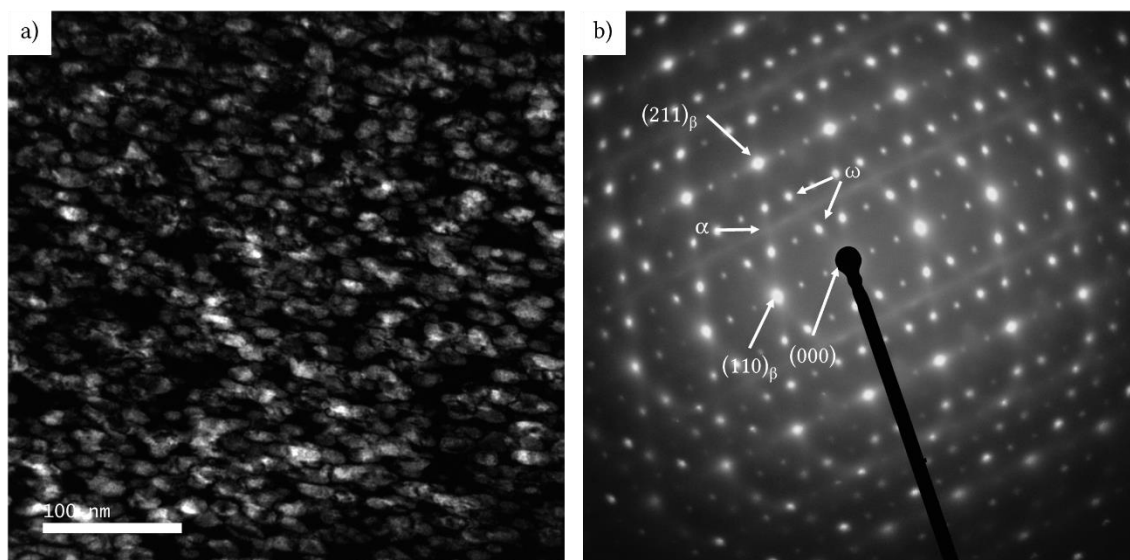


Figure 66. a) Dark field image of ω phase in the sample after isothermal aging at 400 °C / 8 h and b) SAD pattern with electron beam parallel to $[113]_{\beta}$.

The SEM image in Figure 67 shows the evolution of α phase after 8 h aging for 500 °C and 540 °C. For both conditions (500 °C and 540 °C), lamellar intragranular α phases with different morphological orientation were observed, namely grain boundary α (α_{GB}) and Widmanstätten grain boundary α plates (α_{WGB}). By comparing the microstructure after isothermal aging for 8 h at 500 °C (Figure 67 (a)) with 540 °C (Figure 67 (b)) it is observed that the α phase shows a slight coarsening for higher aging temperature.

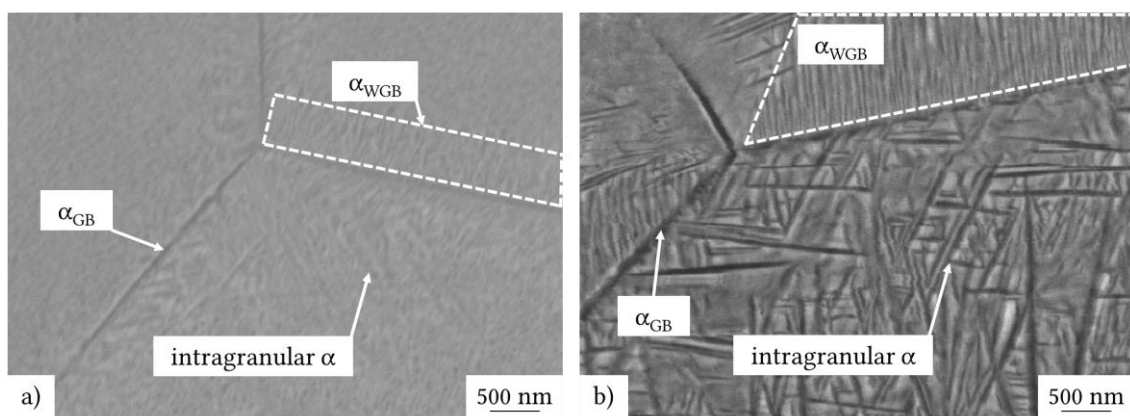


Figure 67. Ti15Mo after heating with 300 K/min and aging for 8h at a) 500 °C and b) 540 °C.

4.3.3.2 EB structuring on Ti15Mo

Figure 68 shows the cross section of the macrostructure after the EB structuring process on Ti15Mo. During the EB process, a gradient of microstructure was formed due to the heat input. A difference between the MZ and HAZ cannot be distinguished. Therefore, the change of the

microstructure is divided into two zones: the MZ and the BM. No defects in the macrostructure and microstructure were observed, such as porosity and cracks, after the EB process.

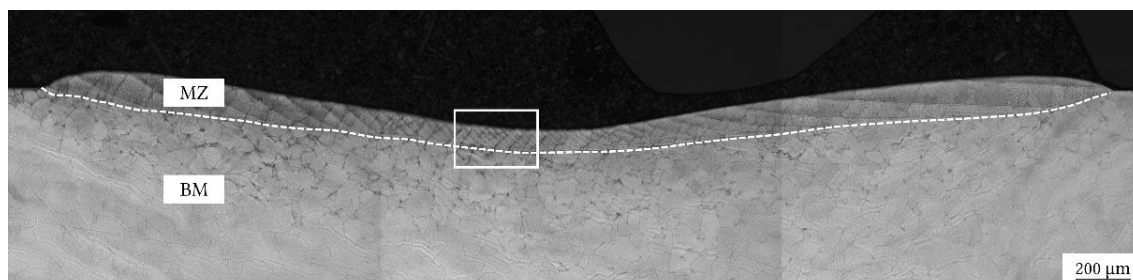


Figure 68. LOM image from a typical cross section of a hexagonal wall array structure on Ti15Mo sample. $I = 2.5$ mA and $v = 697$ mm/s.

The detailed view in Figure 69 reveals the melt pools for each arm number delimited by bright boundaries (marked by white arrows). The growth of the grains started at the fusion line, and showed an epitaxial growth (marked by red filled form) in the direction of the thermal gradient. Furthermore, the red line indicates an example of columnar β grains, that grew epitaxially over multiple melt pools, defined by a cellular substructure (blue arrow in Figure 69, detail in Figure 70).

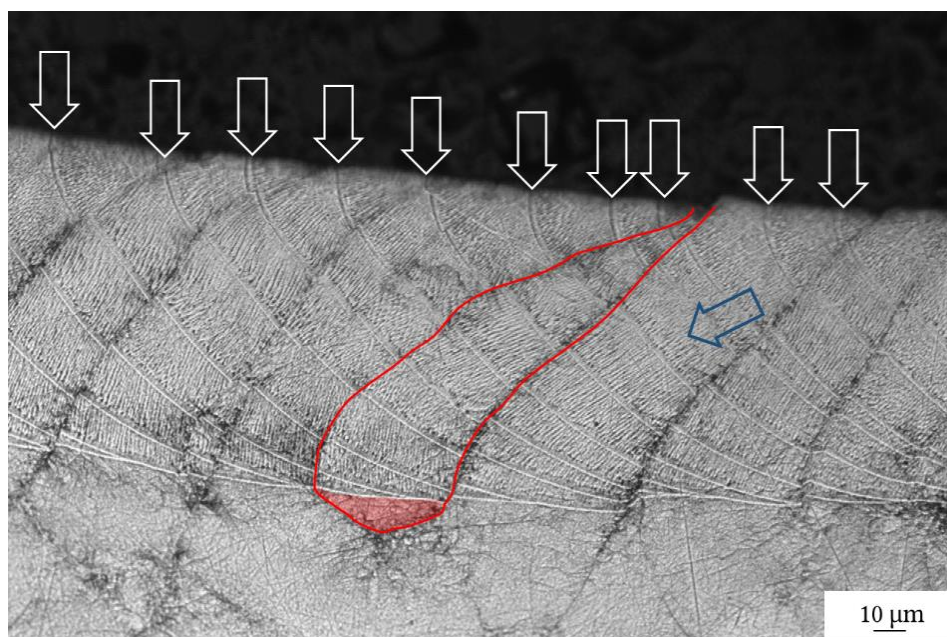


Figure 69. Magnified view of the white rectangular region near to the centre of a wall array figure in Figure 68.

A cellular dendritic substructure with an intercellular spacing between 1 to 2 μm is shown in Figure 70 (a). The EDS line scan depicts a change of Mo content in the cell cores, as shown in Figure 70 (b).

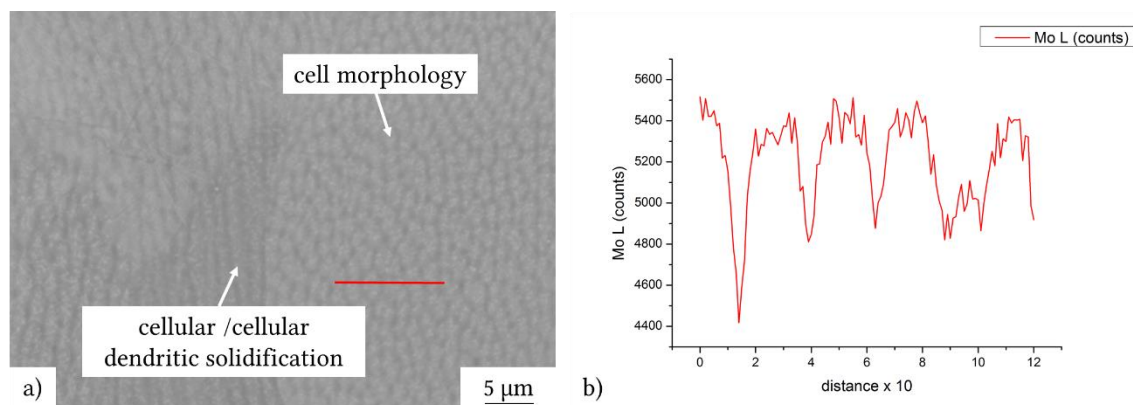


Figure 70. SEM image of a) cellular substructure magnified view of the blue arrow in Figure 69 and b) corresponding EDS line.

EB structured samples were treated based on the dilatometry investigations of the BM, as explained in detail in section 4.3.3. Only the solution treatment (temperature cycle 1, explained in section 3.3.2) was not carried out after structuring. The treatment was defined as follows: continuously heat at 300 K/min up to 400 °C, 500 °C and 540 °C and isothermally hold at 400 °C, 500 °C and 540 °C for 8 h. The hardness values of the β solution treated sample, the MZ and the MZ after additional treatment, are shown in Figure 71. The hardness value after heating to 400 °C ($294 \pm \text{HV}$) was even lower compared to the solution treated sample ($317 \pm \text{HV}$) and the MZ ($321 \pm \text{HV}$). The development of the hardness by increasing the time and temperature behaved similar to the base material. Therefore, the hardness of subsequent quenched samples increased up to $367 \pm \text{HV}$ at 500 °C and decreased to $299 \pm \text{HV}$ at 540 °C. The hardness value of the isothermally aged samples was higher compared to the samples continuous heating. The peak hardness was evaluated at 500 °C after isothermal holding of 8 h ($541 \pm \text{HV}$). After the peak hardness was obtained, it decreased to $350 \pm \text{HV}$.

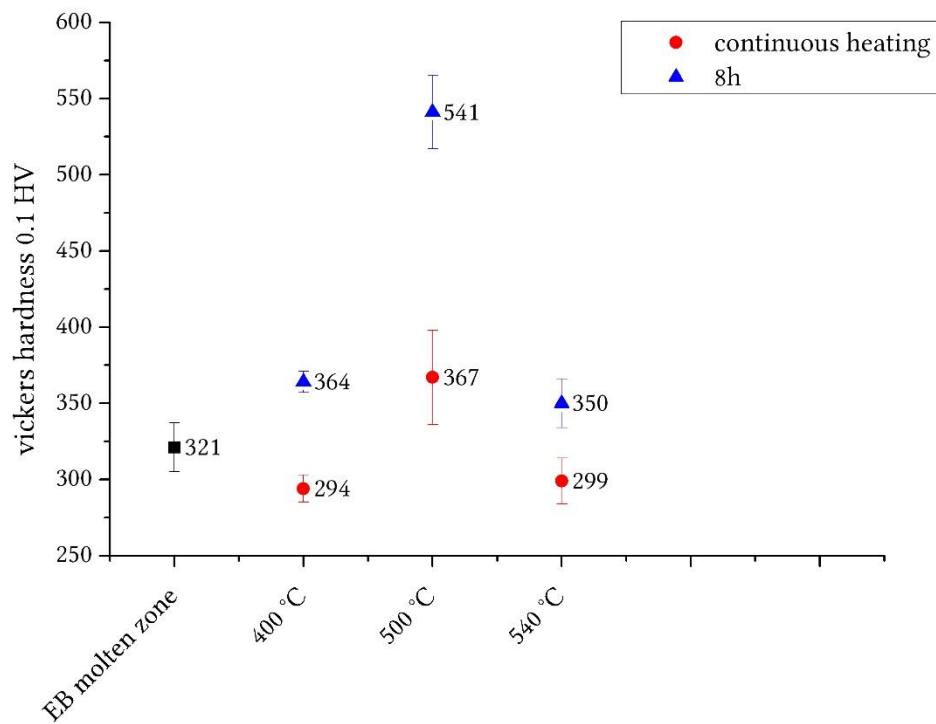


Figure 71. Vickers hardness values of Ti15Mo EB structured samples after continuous heating and isothermal aging.

The microstructure of the MZ was observed with TEM investigations of FIB lamella, as shown in Figure 72. The SAD pattern shows the presence of ω phase and weak streaks for both temperatures (500 °C and 540 °C). These weak streaks are probably from small, newly developed α precipitates.

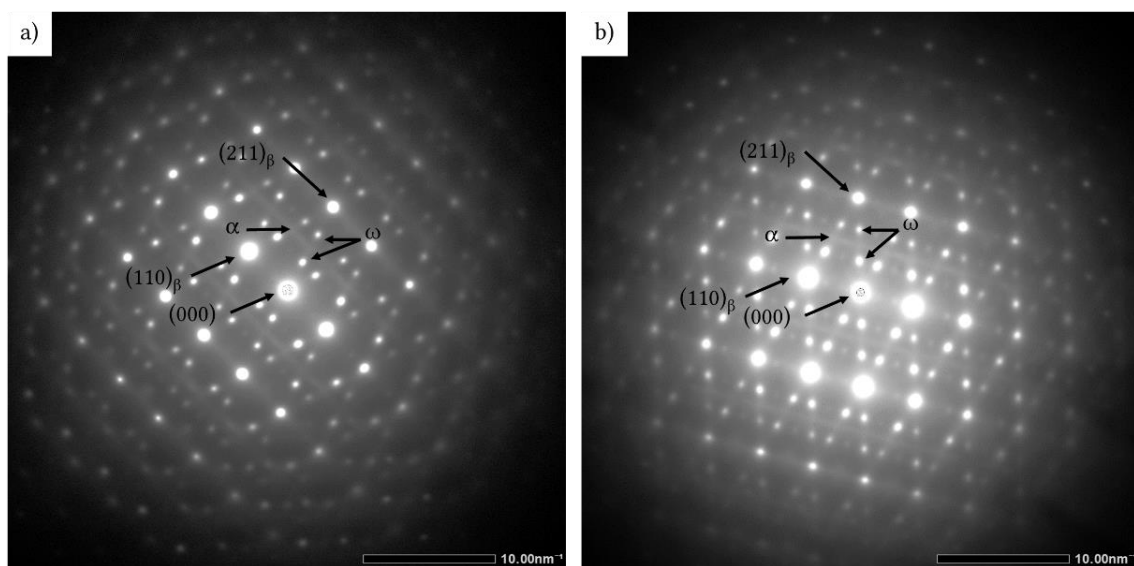


Figure 72. SAD pattern of EB structured samples with electron beam parallel to $[113]_{\beta}$ a) after heating up to 500 °C and b) after heating up to 540 °C.

Figure 73 shows the evolution of the α phase after 8 h isothermally aging at 400 °C, 500 °C and 540 °C. For 400 °C, the dendritic cellular substructure can still be distinguished. After isothermally aging at 500 °C and 540 °C for 8 h, the α phase appeared and showed a slight growth after aging at the higher temperature. The α phase for both aging temperatures was the intergranular α phase, with different morphological orientation, and grain boundary α (α_{GB}).

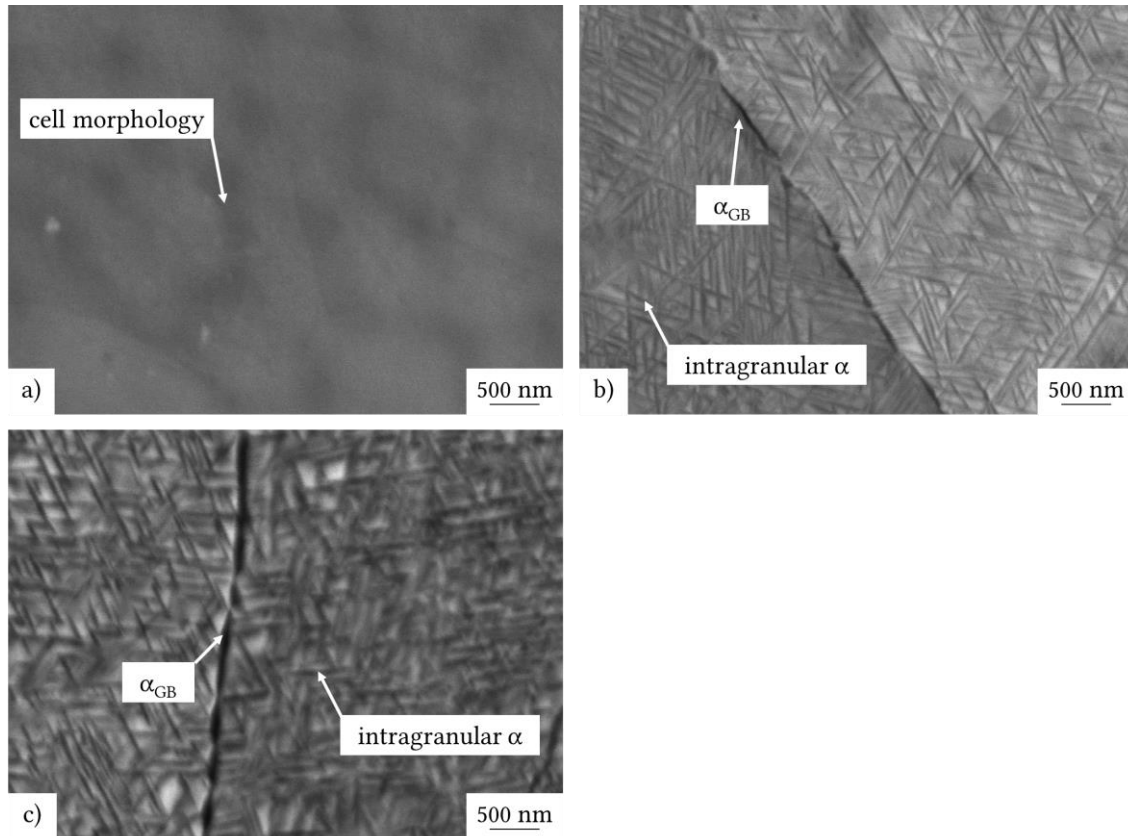


Figure 73. EB structured Ti15Mo after heating with 300 K/min and aging for 8h at a) 400 °C b) 500 °C and c) 540 °C.

The microstructure of the MZ after isothermal aging at 400 °C / 8 h was observed with TEM of the FIB lamella. Figure 74 shows the dark field image and the corresponding diffraction pattern with the electron beam parallel to $[113]_{\beta}$. The dark field image shows an inhomogeneous microstructure across the grain, with ellipsoidal shaped ω phase (20 – 60 nm) and α plates (length between 50 to 200 nm) in the MZ after isothermal aging for 400 °C / 8 h.

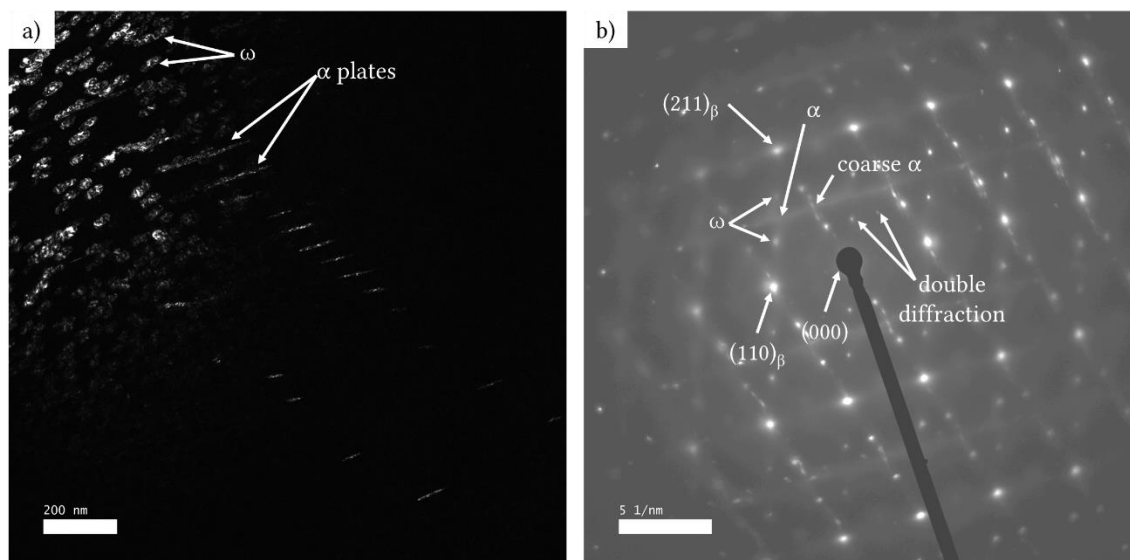


Figure 74. a) Dark field image of ω phase and α phase in sample EB structuring after isothermal aging at 400 °C / 8 h and b) SAD pattern with electron beam parallel to [113] β .

4.4 Biological response by in vitro investigations

Surface characteristics, such as topography and roughness, greatly influence the cell behaviour. In order to estimate the cell behaviour on EB structured titanium alloys, the anchorage, morphology and the cell spreading area were evaluated after different cultivation times and on different surface structures.

4.4.1 Cell morphology

The pictures to analyse the cell morphology were taken randomly on the surface. Figure 75 correlates the different titanium alloys, cp TiGr2, Ti6Al4V and Ti15Mo, after 24 h and 48 h of cultivation time. Furthermore, the variation of arm number (Figure 76) and the change of the energy input (Figure 78) were used to estimate the influence of roughness change. Also, the influence of the structure orientation (Figure 77) was determined by comparing pin and wall array structure.

The cells exhibited a healthy appearance on all investigated alloys and EB structures with many cell-cell interactions. Both filopodia and lammelopodia like structures were observed for these cells.

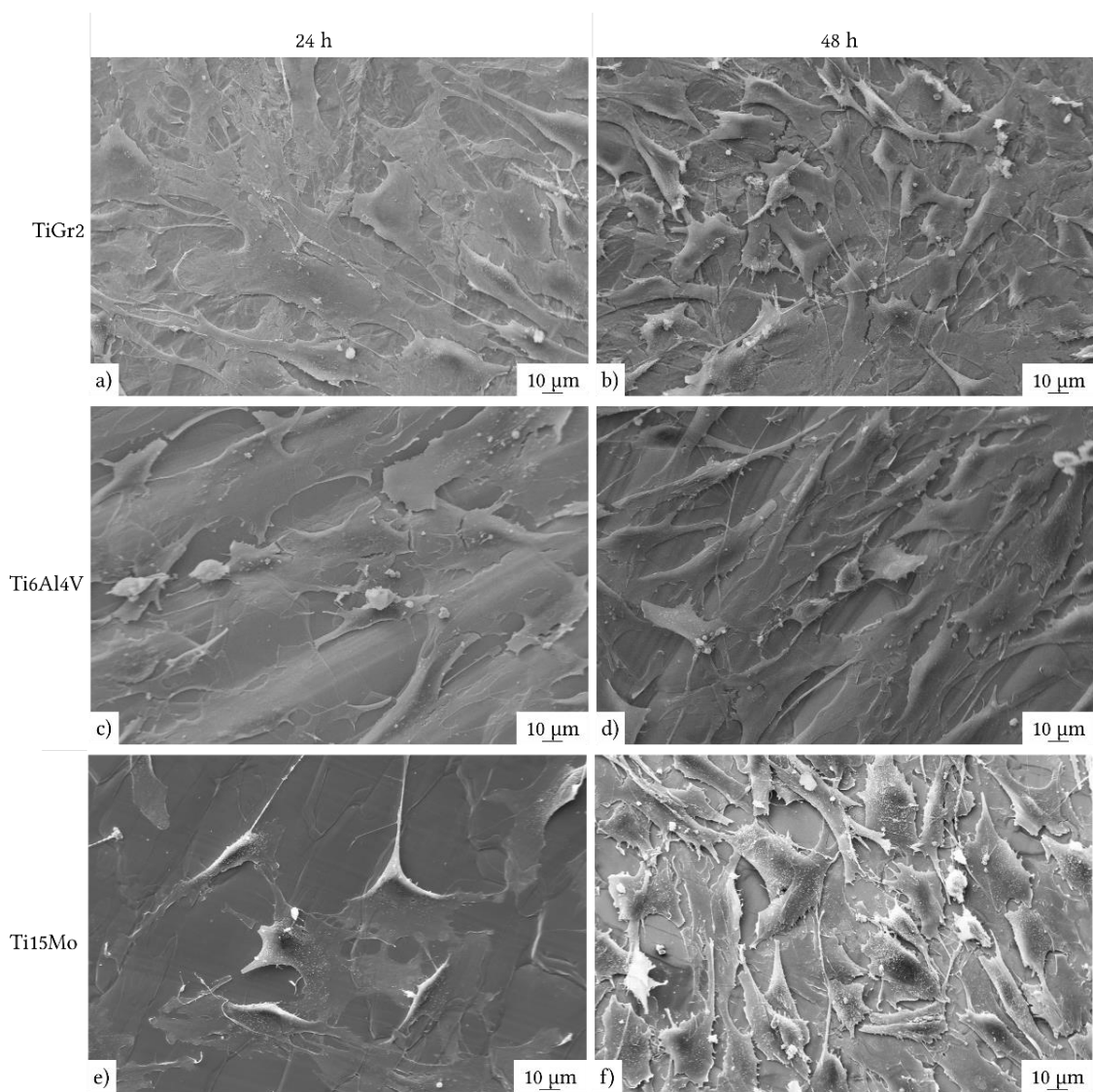


Figure 75. MC 3T3 E1 pre-osteoblastic cell morphology on a hexagonal wall array for $I = 2.5$ and $mA v = 697$ mm/s for a) cultivation on cp TiGr2 for 24h, b) cultivation on cp TiGr2 for 48h, c) cultivation on Ti6Al4V for 24h, d) cultivation on Ti6Al4V for 48 h, e) Ti15Mo cultivation for 24 h and f) Ti15Mo cultivation for 48 h.

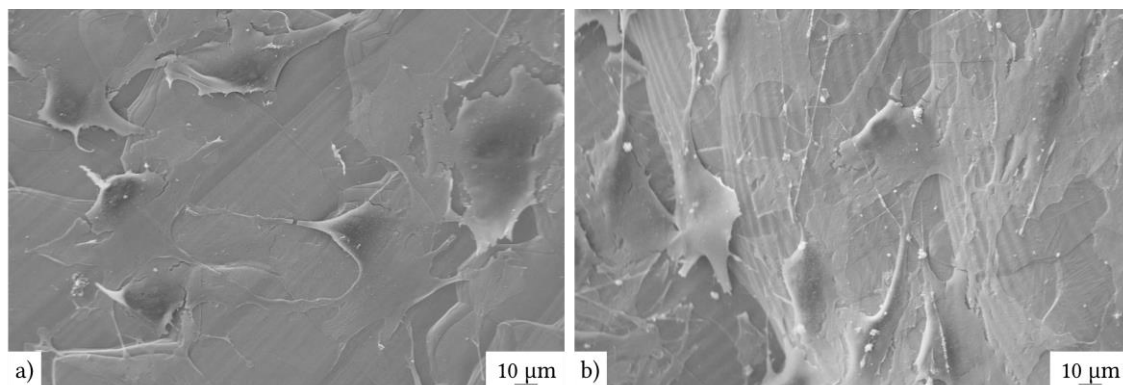


Figure 76. MC 3T3 E1 pre-osteoblastic cell morphology on Ti6Al4V a hexagonal wall array for $I = 2.5$ mA and $v = 697$ mm/s cultivation for 24 h for a) 126 arms and b) 156 arms.

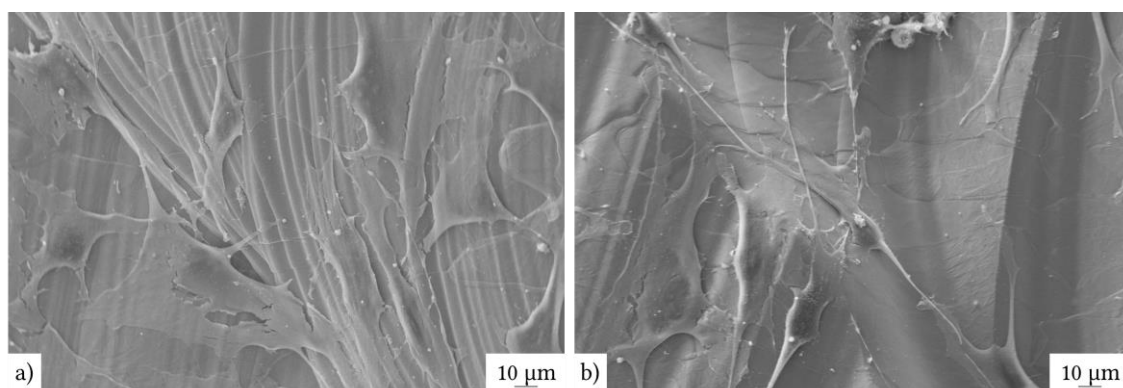


Figure 77. MC 3T3 E1 pre-osteoblastic cell morphology on Ti6Al4V for $I = 2.5$ mA and $v = 697$ mm/s cultivation for 24 h for a) square wall array and b) square pin array.

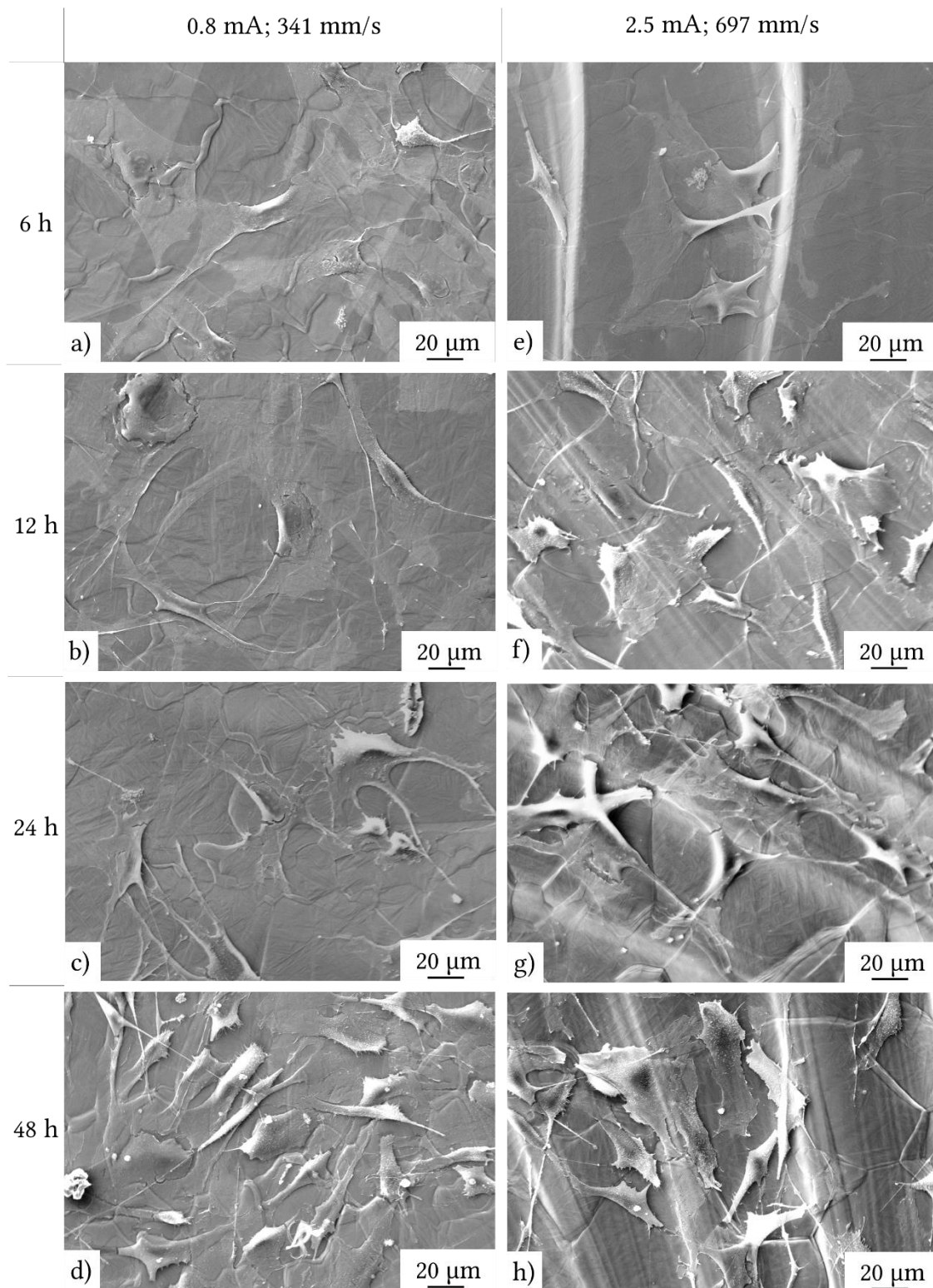


Figure 78. MC 3T3 E1 pre-osteoblastic cell morphology on Ti6Al4V hexagonal pin array for a) to d) $I = 0.8 \text{ mA}$ and $v = 341 \text{ mm/s}$ with a cultivation time from 6 h to 48 h and e) to h) $I = 2.5 \text{ mA}$ and $v = 697 \text{ mm/s}$ cultivation time from 6 h to 48 h.

4.4.2 Distribution of cells

Figure 79 to Figure 83 show a selection of SEM-BSE images of cell experiments after different cultivation times on different areas (Figure 40) for different Ti6Al4V surfaces. Cell experiments on a ground surface (Figure 83), pin array samples with low and high energy input (Figure 50) after cultivation times of 6 h (Figure 79), 12 h (Figure 80), 24 h (Figure 81) and 48 h (Figure 82) are compared.

For all investigated samples with a different cultivation time, a uniform distribution of the cells was visible, except for evaluations in the centre of the rougher samples ($I = 2.5 \text{ mA}$ and $v = 697 \text{ mm/s}$). There, a heterogeneous distribution of cells was observed after different cultivation times. The cells showed a polygonal morphology, and no particular orientation of the cells due to the surface structure was visible on all samples. The diagram in Figure 84 shows the evaluation of SE-BSE images. Therefore, incubation times up to 12 h did not show any significant effect of surface roughness on cell spreading. After 24 h of culture, the measurements showed an influence on the cell spreading. The cells preferred the *structure* on the smoother sample ($I = 0.8 \text{ mA}$ and $v = 341 \text{ mm/s}$) compared to the rough ($I = 2.5 \text{ mA}$ and $v = 697 \text{ mm/s}$) and the control samples. The measurements after 48 h showed a developed difference between the *structure* on the smoother sample ($I = 0.8 \text{ mA}$ and $v = 341 \text{ mm/s}$) compared to the rough ($I = 2.5 \text{ mA}$ and $v = 697 \text{ mm/s}$) and control samples. In sum, after 24 h, a difference between the control sample and EB structured sample was observed.

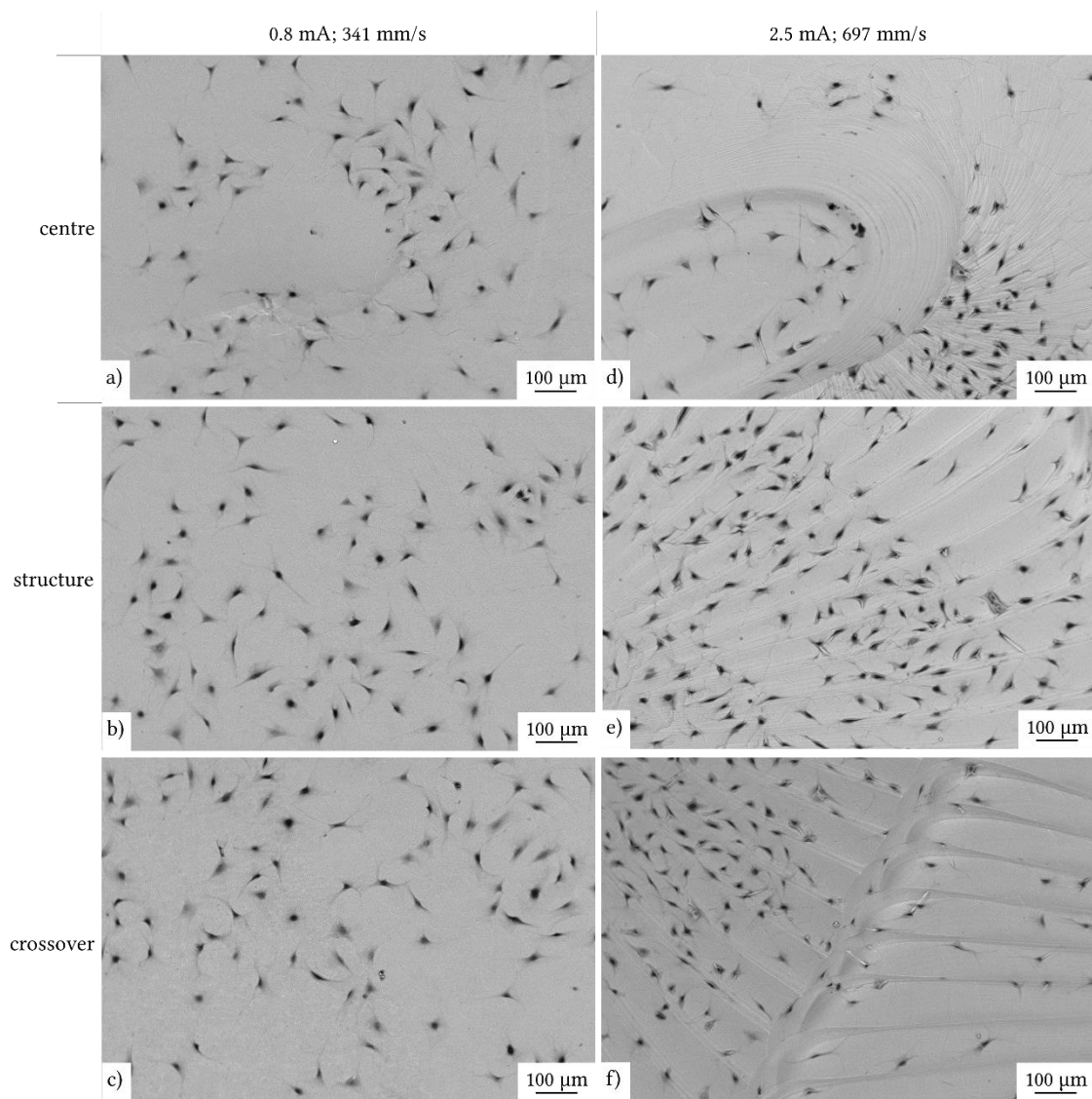


Figure 79. MC 3T3 E1 pre-osteoblastic cells cultivated for 6 h on hexagonal pin array Ti6Al4V samples for a) to c) centre structure cross-over for $I = 0.8$ and $mA v = 341$ mm/s and d) to f) centre structure cross-over for $I = 2.5$ and $mA v = 697$ mm/s.

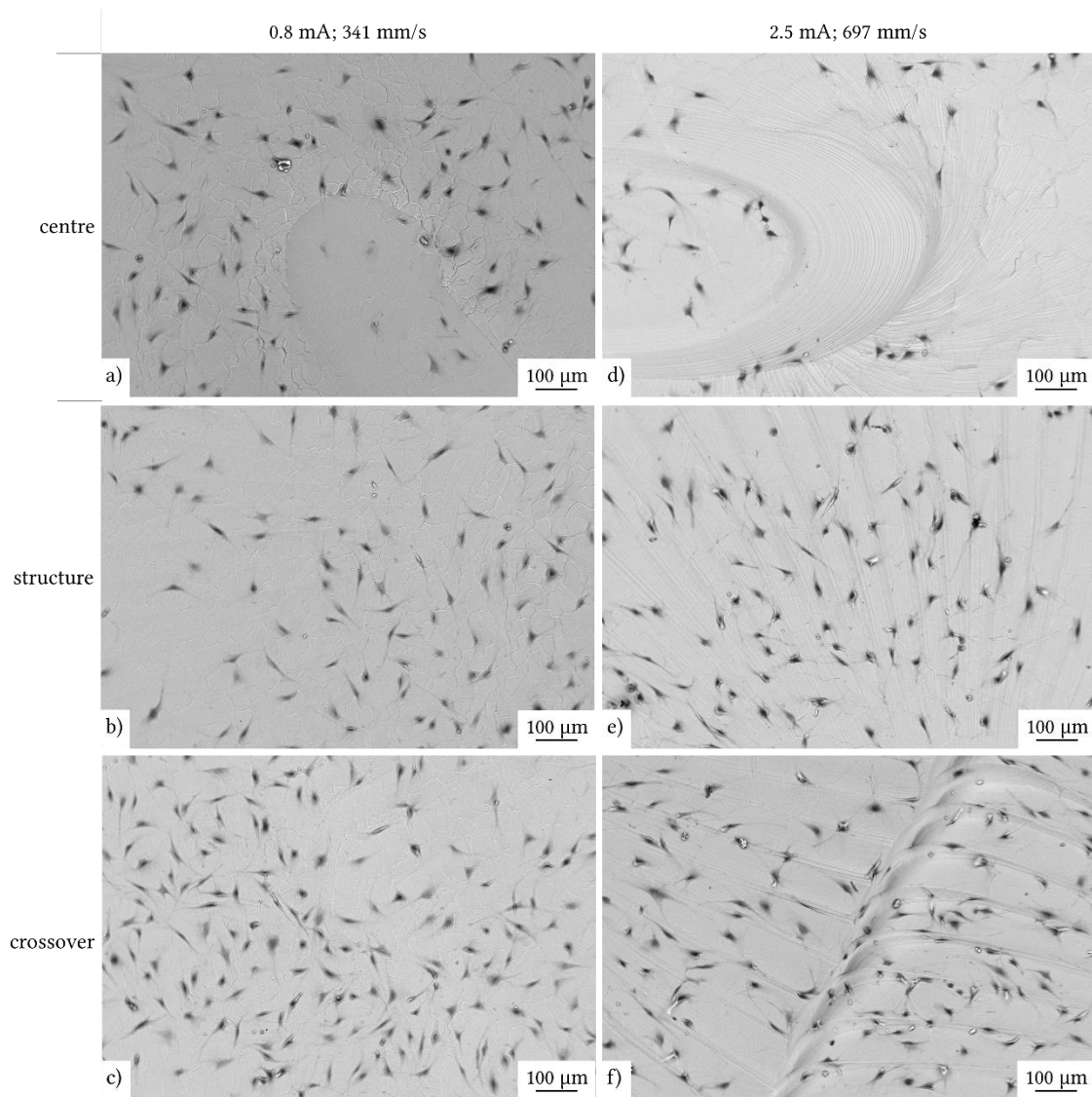


Figure 80. MC 3T3 E1 pre-osteoblastic cells cultivated for 12 h on hexagonal pin array Ti6Al4V samples for a) to c) centre structure cross-over for $I = 0.8 \text{ mA}$ and $v = 341 \text{ mm/s}$ and d) to f) centre structure cross-over for $I = 2.5 \text{ mA}$ and $v = 697 \text{ mm/s}$.

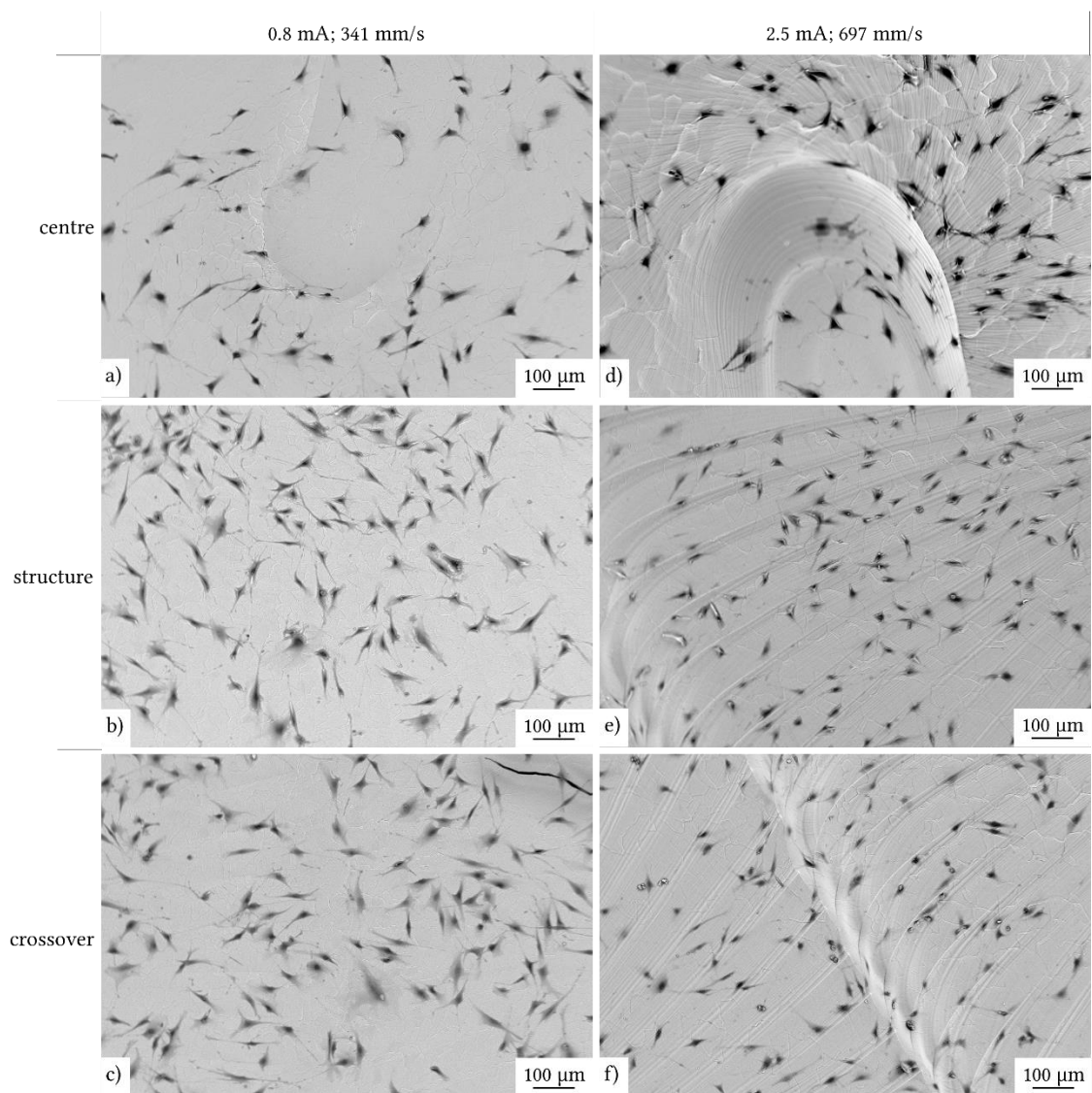


Figure 81. MC 3T3 E1 pre-osteoblastic cells cultivated for 24 h on hexagonal pin array Ti6Al4V samples for a) to c) centre structure cross-over for $I = 0.8$ mA and $v = 341$ mm/s and d) to f) centre structure cross-over for $I = 2.5$ mA and $v = 697$ mm/s.

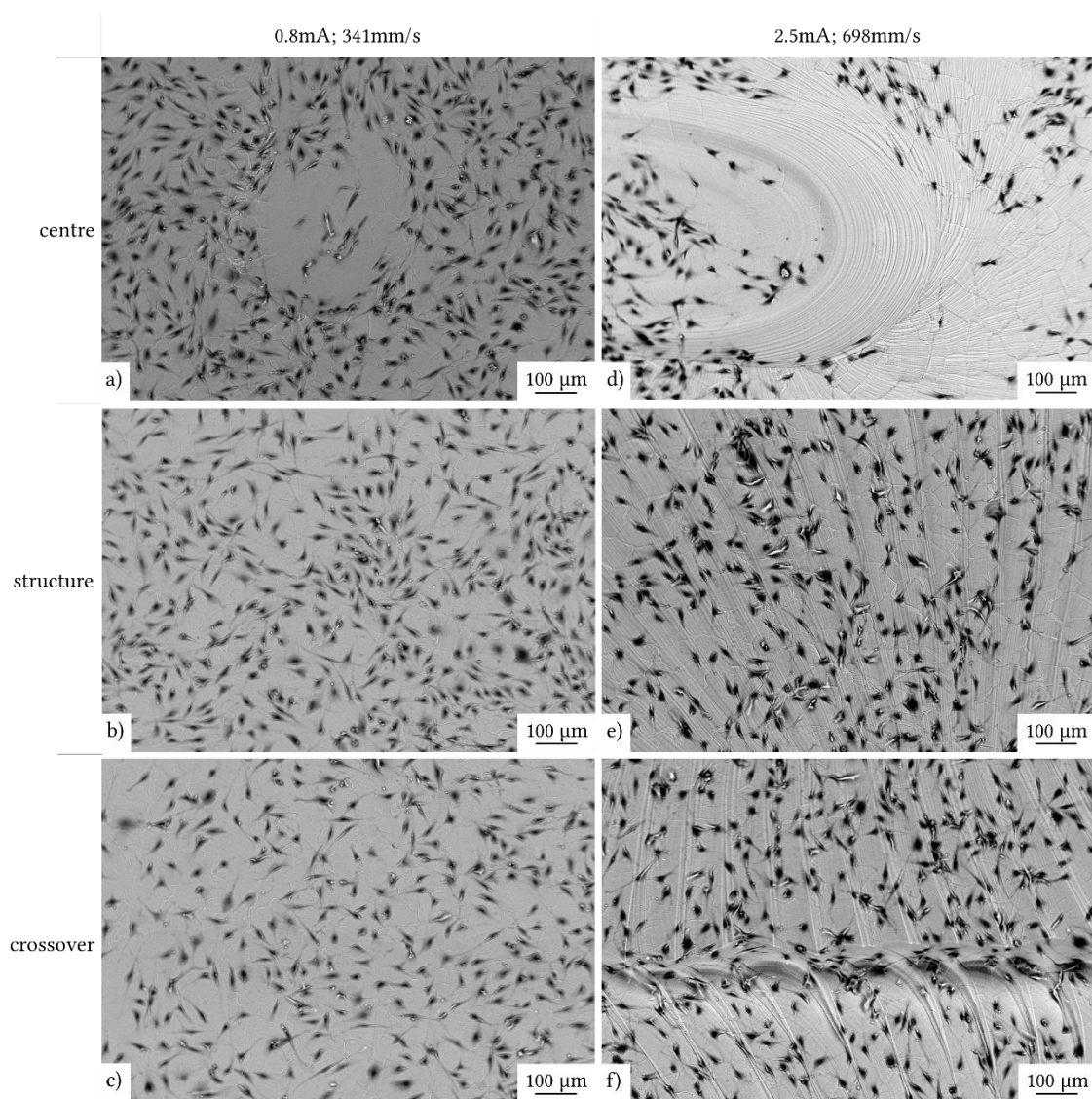


Figure 82. MC 3T3 E1 pre-osteoblastic cells cultivated for 48 h on hexagonal pin array Ti6Al4V samples for a) to c) centre structure cross-over for $I = 0.8 \text{ mA}$ and $v = 341 \text{ mm/s}$ and d) to f) centre structure cross-over for $I = 2.5 \text{ mA}$ and $v = 697 \text{ mm/s}$.

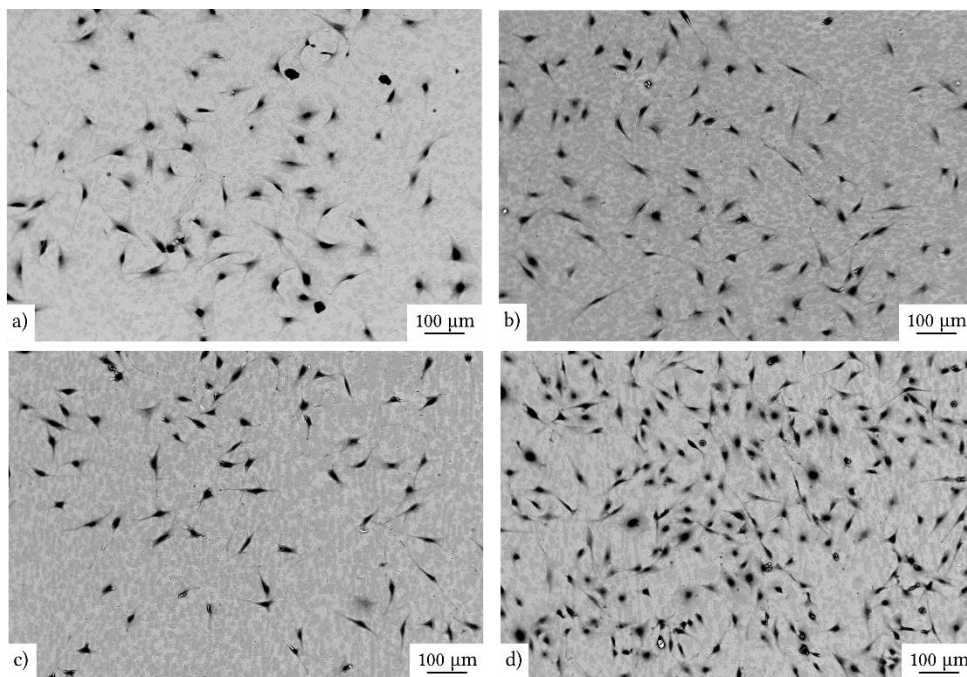


Figure 83. MC 3T3 E1 pre-osteoblastic cells Ti6Al4V control samples (without structuring) for different cultivation time for a) 6 h, b) 12 h, c) 24 h and d) 48 h.

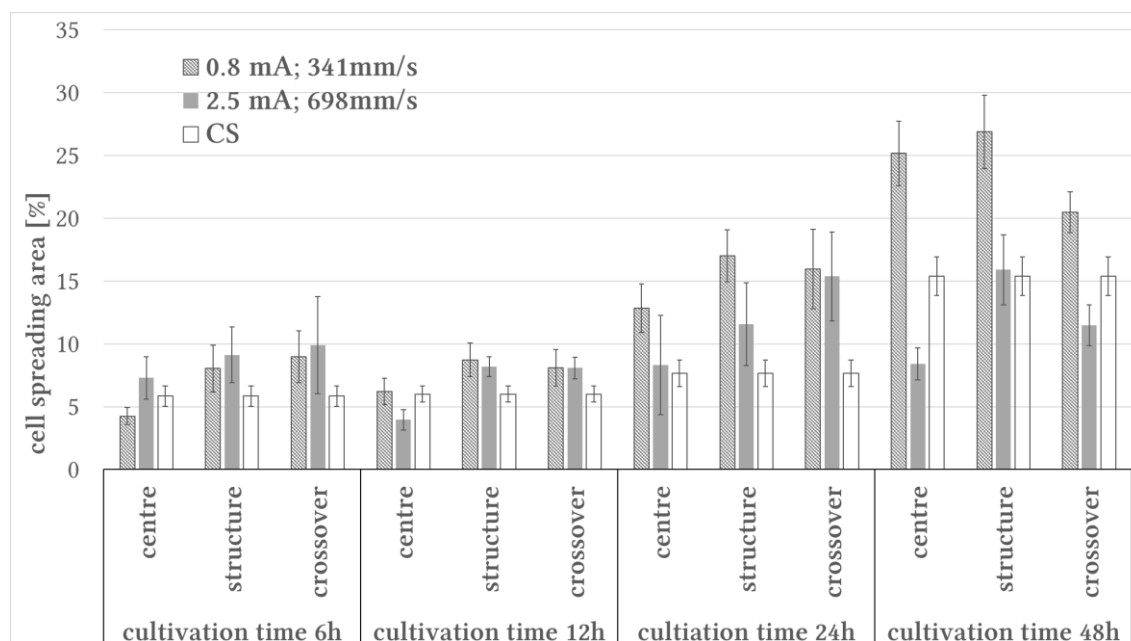


Figure 84. Cell distribution of MC 3T3 E1 pre-osteoblast cells at cultivation times of 6 h, 12 h, 24 h and 48 h on two EB structured patterns at different areas on the surface and control sample (CS) (n=10).

5 Discussion

This chapter analyses the solidification and microstructural behaviour of the investigated titanium alloys after the EB structuring process. Namely, the post heat treatment response of Ti6Al4V and Ti15Mo will be covered. The influence of cell morphology and spreading area on titanium structured samples will also be discussed.

5.1 EB process as a structuring technique

The achievable beam focus is one of the most important limits for EB structuring. Corresponding to the specifications, the EB machine can reach a minimum beam focus diameter of 0.1 mm. Nevertheless, this requires a perfect focus on the surface of the specimen and a perfect setup of the machine. In this work, a beam diameter of 0.3-0.4 mm was probably obtained, although it was not measured.

The present experiments showed that the energy input to melt the material needed to be greater than 178 J/m. Investigations with a current of 0.8 mA showed the greatest deviation of the MZ (depth and width) (Figure 42 and Figure 43) and surface structuring compared to 2.5 mA (Table 13). The specifications of the EB machine allowed a fluctuation of ± 0.2 mA. This means that for the current set for the experiments with 0.8 mA, there was a deviation of ± 25 %, whereas for 2.5 mA, the deviation was about 8 %.

Several conventional techniques have been proposed for surface structuring, such as shot peening [96], anodization [19] [97], plasma spraying [97] and acid etched surfaces [97], among others. However, propagation of cracks in the subsurface region, nucleation of voids and additional treatments to remove weakly adhering particles limit the application of such techniques compared to EB structuring. The EB structuring process enables surface structuring with a single step process and the machining is performed without contact through a beam and without additional material. Furthermore, many parameters of the EB process can easily be adjusted, resulting in a great variety of possible structures and the ability to reproduce hierarchical multi-scale surface topographies. This is similar to the laser texturing technique, where pit pattern and parallel grooves have been observed, described in Ref. [54] and [96].

5.2 Solidification of cp TiGr2, Ti6Al4V and T15Mo during EB structuring process and change of the mechanical properties

5.2.1 Cp TiGr2

The EBSD investigations were carried with a cross section after EB structuring in the MZ. The IPF map, shown in Figure 85 (a), presents the microstructure of cp TiGr2 after EB structuring and indicates a columnar, coarse and plate-like grain morphology with irregular grain boundaries along the z direction. The direction of the columnar grains is in the direction of the thermal gradient. The evolution of grains after the EB structuring is similar to EBM processes and laser beam welding of cp TiGr1 and cp TiGr2 [75], [98]. Palanivel et al. [98] described the grains in the fusion zone as coarse and elongated granular-like grains with serrated and irregular boundaries. Nevertheless, the coarseness of the grains can be changed by increasing the cooling rate (due to increasing the welding speed) [99]. The misorientation in the grains of the MZ, as shown in Figure 85 (b), is heterogeneous, in accordance to Ref. [99]. Liu et al. [99] describe the misorientation distribution of pure titanium after laser beam welding in the fusion zone by the high cooling rate associated with the welding speed. After EB structuring, the MZ presents a slight hardness increase of 189 HV compared to 164 HV for the base material. According to the literature [98], the increase in hardness in the fusion zone is directly related to nitrogen and oxygen content, localized strain fields and an increase of substructure boundary concentrations due to an increase of welding speed.

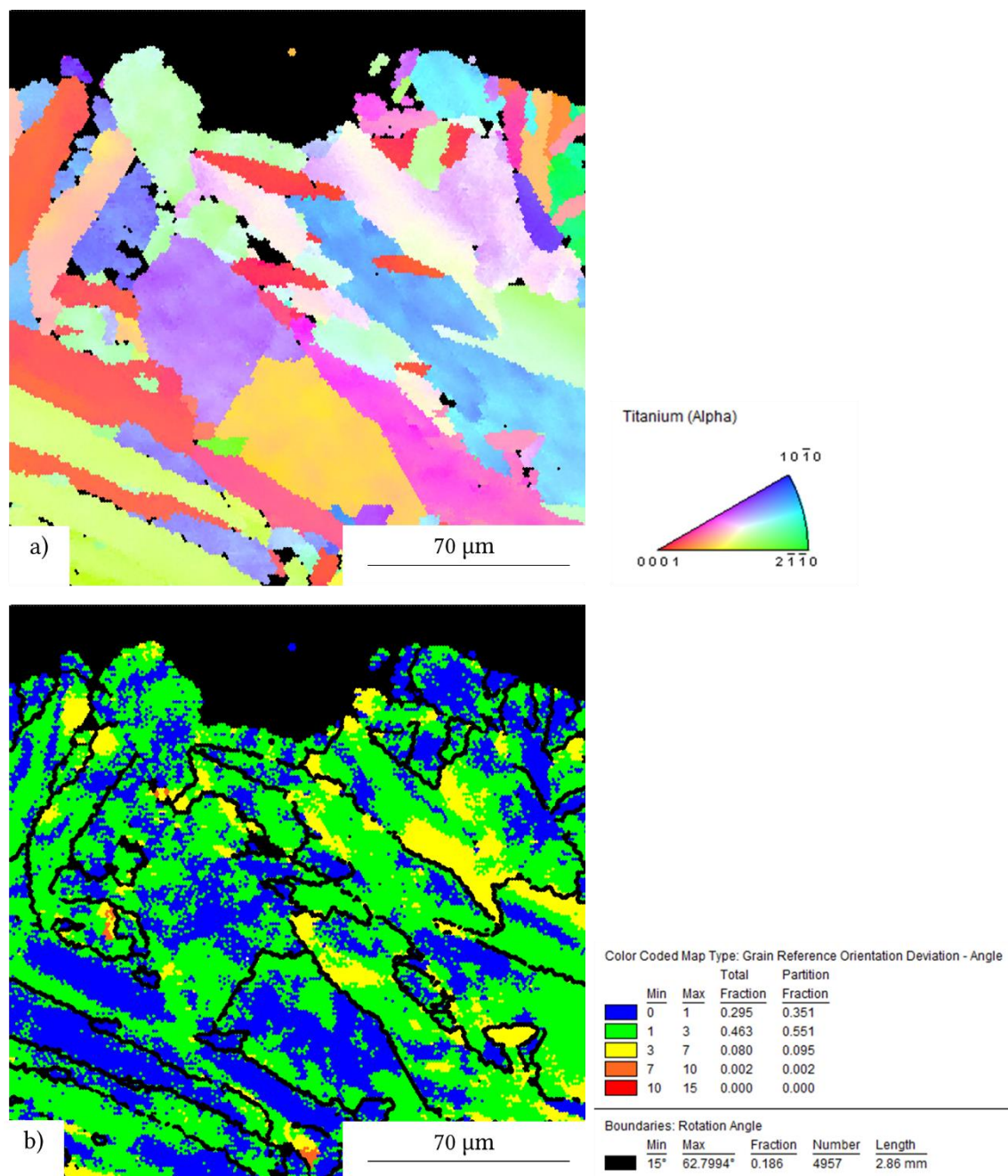


Figure 85. EBSD investigations of cp TiGr2 after EB structuring in the MZ of pin array for $I = 2.5$ mA and $v = 697$ mm/s shown as a) IPF map and b) grain reference orientation (GROD) map.

5.2.2 Ti6Al4V

The first observation of EB structured Ti6Al4V at a small magnification in the building direction (z direction) revealed columnar prior β grains (Figure 55). The grains grew epitaxially in the direction of the thermal gradient. This is similar to the AM process, where the re-melted grains of the previous layer acted as nuclei for the epitaxial growth [76], [100], [101]. The microstructure after the EB process did not show any melt pool boundaries, in accordance with

Vilaro et al. [76] and in contrast to Yadroitsev et al. [77]. They reported a change of the melt pool boundary by changing scanning strategies. The cooling rate was estimated by Qian et al. [102] to be about $7 \cdot 10^4$ K/s after a single laser pass in argon atmosphere, and was calculated for EBM in vacuum to be between 10^3 and 10^5 K/s [71]. Therefore, the microstructure in the prior β grains was composed of α' phase formed by shear deformation, related to an extremely high cooling rate from the β domain [103], [104]. This is similar to SLM [100], [105] and EBM [71] produced Ti6Al4V parts, and the fusion zone of a laser welded Ti6Al4V [73]. The hardness value after SLM depends on the scanning velocity and strategy, and generally varied between 409 and 479 HV [104], which is in a good agreement with 449 ± 23 HV in the MZ after EB structuring. The microstructure in the HAZ consisted of a mixture of α' , primary α and β phase. The peak temperature in the HAZ was assumed to be lower than β transus, and higher than the martensite start temperature (M_s). Therefore, the microstructure in the HAZ during the process consisted of $\alpha + \beta$ (< 1020 °C ± 5) under high temperature for a short time (less than 2 s), where the α phase was not transformed to the β phase and some α' phase was formed at the boundaries and interior β grains due to the fast cooling [103], [73]. Vrancken et al. [100] correlated a reference material with untreated SLM, as shown in Table 15. The ductility of the SLM part was much lower (less than 10 %) in comparison to the equiaxed Ti6Al4V, due to the α' phase.

Table 15. Mechanical properties of Ti6Al4V before and after SLM; adapted from [100]

| | E-Modulus [GPa] | σ_Y [MPa] | UTS [MPa] | $\epsilon_{\text{fracture}}$ [%] |
|--------------------------------|--------------------|---------------------|---------------|-------------------------------------|
| equiaxed Ti6Al4V | 120.2 ± 1.9 | 960 ± 10 | 1006 ± 10 | 18.37 ± 0.88 |
| α' phase (after SLM) | 109.2 ± 3.1 | 1110 ± 9 | 1267 ± 5 | 7.28 ± 1.12 |

The microstructure observations after post heat treatments at 650 °C and 720 °C for 2 h and 8 h corresponded to similar observations in heat treated Ti6Al4V of SLM samples [76], [100]. Vilaro et al. [76] also observed that a $\alpha' + \beta_{\text{metastable}} + \alpha$ phase microstructure after a heat treatment at 730 °C for 2 h experienced a slight reduction of the yield strength and the ultimate strength but was favoured by higher ductility. Vrancken et al. [100] described the transformation of the α' needles to a mixture of α and β alloy in SLM parts with similar heat treatments, where the fracture strain was higher compared to ASTM standards for forged and cast parts.

5.2.3 Ti15Mo

The EBSD investigations were carried out with a cross section after EB structuring. The IPF map, as shown in Figure 86 (a), shows the microstructure of Ti15Mo after EB structuring and indicates elongated grains along the z direction, similar to Ti6Al4V, where a SLM typical grain growth controlled the solidification [78], [106]. The melt pool boundaries of each arm for EB structuring of Ti15Mo, indicated by blue arrows Figure 87 (a), acted as sites for nucleation of grain growth and were not in direct correlation to grain boundaries. This is similar to scan track boundaries of a near beta titanium alloy produced by SLM, as shown in Figure 87 (b) [74], [78]. Furthermore, the MZ was revealed and showed a size of 250 μm .

The destabilization of the planar solidification caused by the changing ratio of the solidification rate and thermal gradient led to a cellular / cellular dendritic solidification inside of the grain for Ti15Mo structured samples, according to Ref. [78], [107]. This type of solidification occurs often during welding or AM [68], [74] and forms chemical segregations [74]. Nevertheless, the misorientation inside the grains were heterogeneous in the MZ compared to the BM, as shown in GROD map in Figure 86 b). These differences are normally indicated by deformation of the microstructure [108]. In this case, it was not possible that the difference occurred due to deformation. Schwab et al. [74] considered no direct correlation of the scan track boundaries and the building direction. They assumed that this effect was related to the epitaxial grain growth and the repeated fusion occurring by the SLM process, and proposed further investigations for a better understanding.

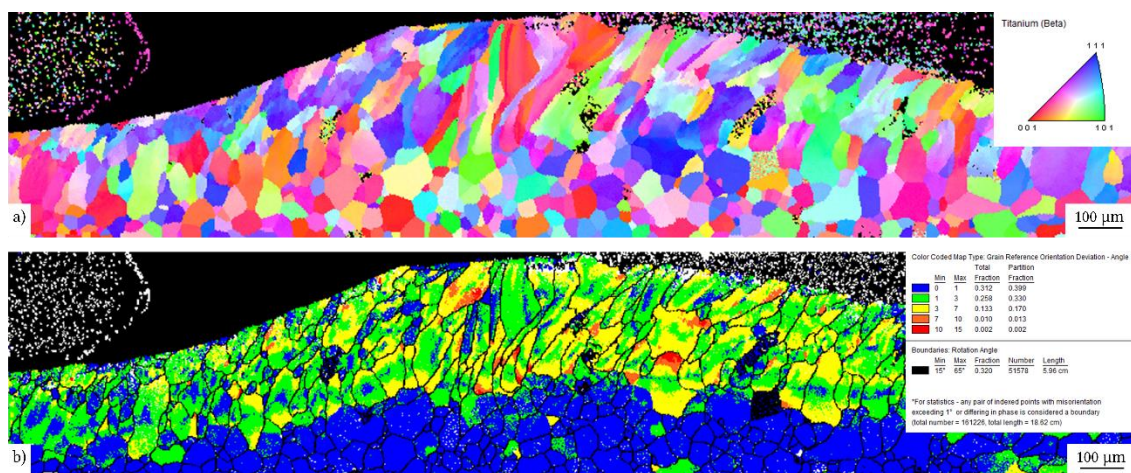


Figure 86. EBSD images of Ti15Mo after EB structuring of pin array for $I = 2.5$ mA and $v = 697$ mm/s shown as a) IPF map and b) GROD map.

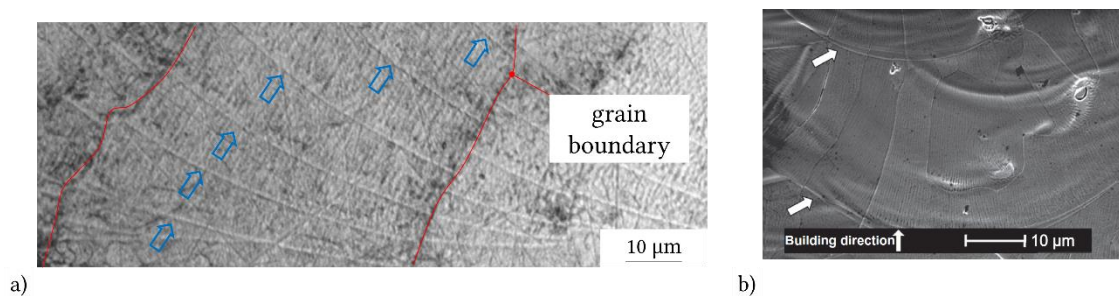


Figure 87. a) LOM image from a typical cross section of a hexagonal wall array structure on Ti15Mo, indicating the solidified melt pool boundaries (blue arrows) and the grain growth through layers (red lines) and b) SEM/SE image of SLM of Ti6Al4V + 10 % Mo, where the grain grew across the melt pool boundary (indicated by white arrows) [78].

5.3 Age response and phase evolution of Ti15Mo

The hardness measurements after EB structuring in the MZ ($321 \text{ HV} \pm 13$) showed a similar value compared to the solution treated sample ($317 \text{ HV} \pm 19$) and differed from the base material ($342 \text{ HV} \pm 9$). This can be related to the fact that the as-delivered material did not include any information about the cooling of the samples. Nag et al. [95] reported the sensitivity of α phase formation by changing the cooling rate. Therefore, the α precipitates were coarser for slow cooling (furnace cooled) compared to fast cooling (water quenched) for beta titanium alloys.

The comparison of different heating rates (5 K/min, 100 K/min, 200 K/min and 300 K/min) showed a shift of the temperature ranges where a divergence from the linear volume expansion occurred. Similar to observations from Barriobero et al. [109], where differential scanning calorimetry curves presented similar behaviour of phase transformations, there was a shift to higher temperatures when increasing heating rate. Diffusion controlled processes were shifted to higher temperatures with increasing heating rates. The end of the second temperature range at 560°C did not change with heating rates of 100 K/min, 200 K/min and 300 K/min. Also, the hardness values after these heating rates were the same and similar to the solution treated samples (317 HV). Therefore, it can be assumed that the matrix of Ti15Mo, after quenching from 560°C in argon atmosphere, consisted of β and due to the quenching of ω_{ath} . Zahnal et al. [110] showed the same behaviour for Ti15Mo, and caused it by the dissolution of the ω_{iso} phase at 560°C . This caused the small hardness increase after heating at 5 K/min because of compositional pockets affecting the phase precipitation.

The microstructure of Ti15Mo after solution treatment consisted of $\beta + \omega_{\text{ath}}$ and exhibited a hardness of $317 \text{ HV} \pm 19$. This value can be associated with the hardness of solution treated Ti15Mo (317 HV) [111] and Ti 19Nb 1.5Mo 4Zr 8Sn (310 HV) [112]. Similar values were obtained for the MZ and after heating with 300 K/min to 400°C for Ti15Mo and Ti15Mo+EB,

as shown in Figure 88. Thus, it can be argued that heating with 300 K/min up to 400 °C had no effect on the ω_{iso} precipitation.

The characteristics of hardness values at 500 °C and 540 °C were even for Ti15Mo and Ti15Mo+EB. Therefore, it can be assumed that the cellular substructure after the EB process had no effect on the formation of ω_{iso} . At 500 °C, a significant hardness increase occurred during heating. The peak value at 500 °C, and the decrease at 540 °C, were expected to be due to the formation and dissolution of ω_{iso} . Therefore, the precipitation sequence during continuous heating from room temperature to 540 °C for Ti15Mo and Ti15Mo+EB was determined to be: $\beta + \omega_{ath} \rightarrow \beta + \omega_{iso} \rightarrow \beta$. Nag et al. [95] reported a ω solvus temperature for the Ti 5AL 5Mo 5V 3Cr 0.5 Fe alloy to be in the range of 350 – 400 °C. Furthermore, XRD patterns for Ti 7Nb 10Mo showed an evolution (at 500 °C) and dissolution (at 650 °C) of ω_{iso} , indicated with red arrows in Figure 89 [32]. The discrepancy of the ω solvus temperature, compared to Ti15Mo, was related to different heating rates and chemical composition of the alloys [113] [114], although for both investigations the heating rate was not noted. The hardness at 540 °C showed a significant decrease, and is comparable to the initial condition and 400 °C. Therefore, the ω phase revealed in the SAD pattern (Figure 65 (b) and Figure 72(b)) was related to the ω_{ath} formation during quenching from 540 °C.

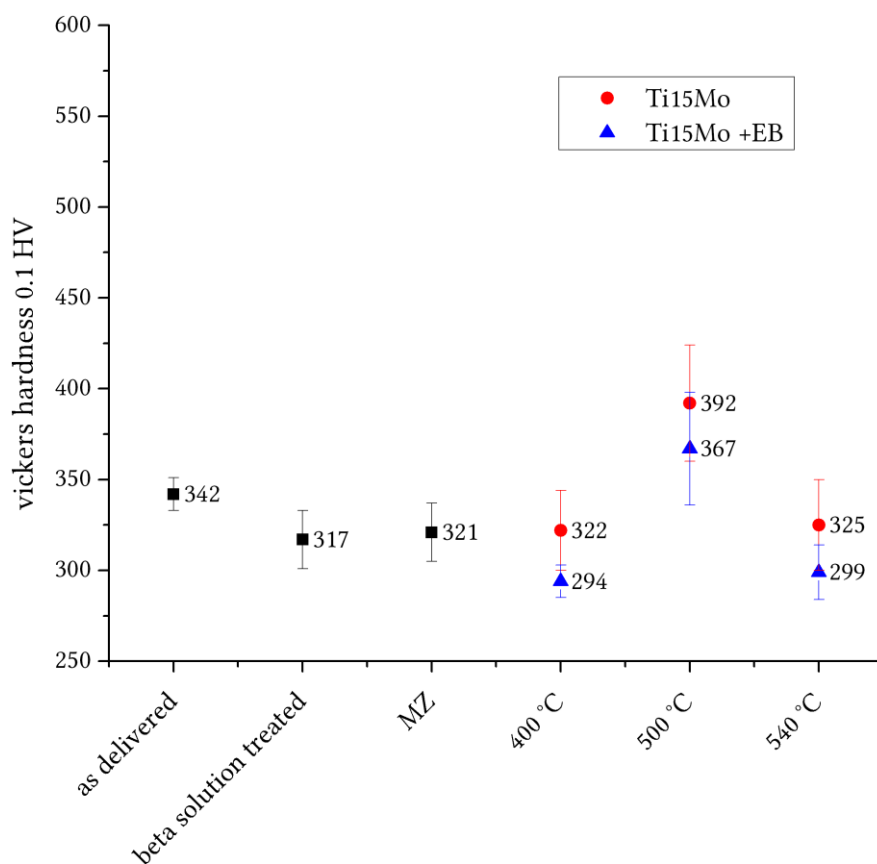


Figure 88. Vickers hardness measurement values for Ti15Mo and Ti15Mo+EB samples and additional treatment of continuous heating with 300 K/min up to 400 °C, 500 °C and 540 °C.

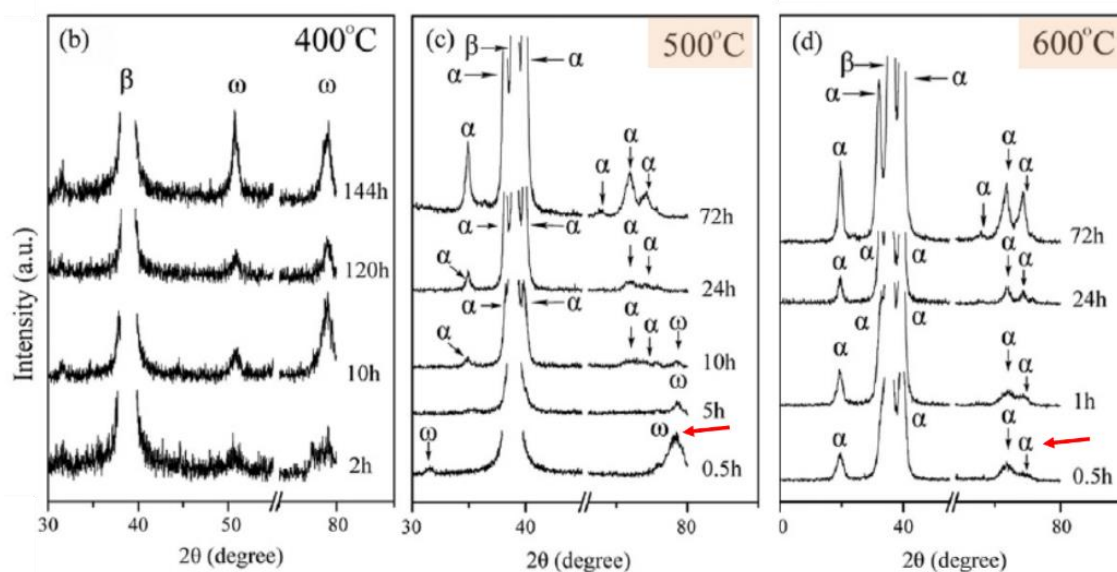


Figure 89. XRD patterns of samples aged for different holding time and temperatures a) 350 °C, b) 400 °C, c) 500 °C, d) 600 °C and e) 650 °C adapted from Yi et al. [32].

Figure 90 summarizes the hardness values after 8 h aging at 400 °C, 500 °C and 540 °C for Ti15Mo and Ti15Mo+EB samples. It also includes hardness values after 24 h aging for Ti15Mo+EB samples with different heating rates (5 K/min and 300 K/min) up to 550 °C and 600 °C. Hardness values after isothermal aging for 8 h at 400 °C, 500 °C and 540 °C showed a similar development compared to samples of continuous heating, where the peak hardness value was reached at 500 °C. As mentioned, the continuous heating experiments at 400 °C, 500 °C and 540 °C showed a formation of ω_{iso} at 500 °C and a dissolution at 540 °C for Ti15Mo+EB. This trend was also observed for Ti15Mo samples with a heating rate of 300 K/min.

Aging for 8 h at 400 °C revealed a hardness increase for Ti15Mo+EB and Ti15Mo, compared to continuous heating at 400 °C. The hardness of Ti15Mo was higher (411 ± 67 HV) compared to Ti15Mo+EB (364 ± 7 HV). Therefore, the microstructure of Ti15Mo showed ellipsoidal ω_{iso} particles with a size between 10 to 20 nm. Li et al. [115] reported a similar hardening effect between 300 °C and 400 °C for a metastable β alloy (Ti – 2 Al – 9.2 Mo – 2 Fe) due to the presence of ω_{iso} (35 nm to 50 nm) and acicular α in a nanoscale (30 nm to 40 nm). The weaker hardening response of Ti15Mo+EB should be related to the inhomogeneous microstructure and the presence of ω_{iso} (20 nm to 60 nm), and α plates with a maximum size of 200 nm, according to Ref. [115], where a weaker hardening was observed with coarse α plates, with a size range of 0.5 μm to 3 μm .

Aging for 8 h at 500 °C revealed the highest hardness values. Therefore, the Ti15Mo+EB sample showed a hardness value of $541 \pm \text{HV}$, which is 103 HV higher compared to aging the Ti15Mo sample ($438 \pm \text{HV}$). The difference in hardness can be related to the cellular dendritic sub-grain structure with compositional pockets of low Mo content left in the β matrix, which affected the α and ω_{iso} phase precipitation. Li et al. [115] mentioned that a high temperature leads to a high diffusion rate for a Ti-2Al-9.3Mo-2Fe metastable titanium alloy, and promotes the growth of larger ω phase, for example 11 – 14 nm for 450 °C and 30 – 40 nm for 500 °C. Therefore, high temperature aging at 500 °C led to a large size for the ω phase (30 – 40 nm) and contributed to a high hardness value, compared to aging at 400 °C. Thus, it can be argued that the microstructure after aging at 500 °C for 8 h consisted not only of plate-like α phase, but also coarse ω_{iso} . To confirm the hardening effect after 8 h isothermal aging at 500 °C, and the difference between Ti15Mo and Ti15Mo+EB, additional TEM investigations would be necessary.

When aged at 540 °C for 8 h, the hardness value decreased to $350 \pm \text{HV}$ and $399 \pm \text{HV}$ for Ti15Mo+EB and Ti15Mo, respectively. The hardness values continued to decrease after aging for 24 h at 550 °C and 600 °C (after different heating rates). The microstructure after aging for 8 h at 540 °C consisted of coarse α plates, which resulted in a poor hardening, or even softening, compared to the initial condition, according to Ref. [113], [115].

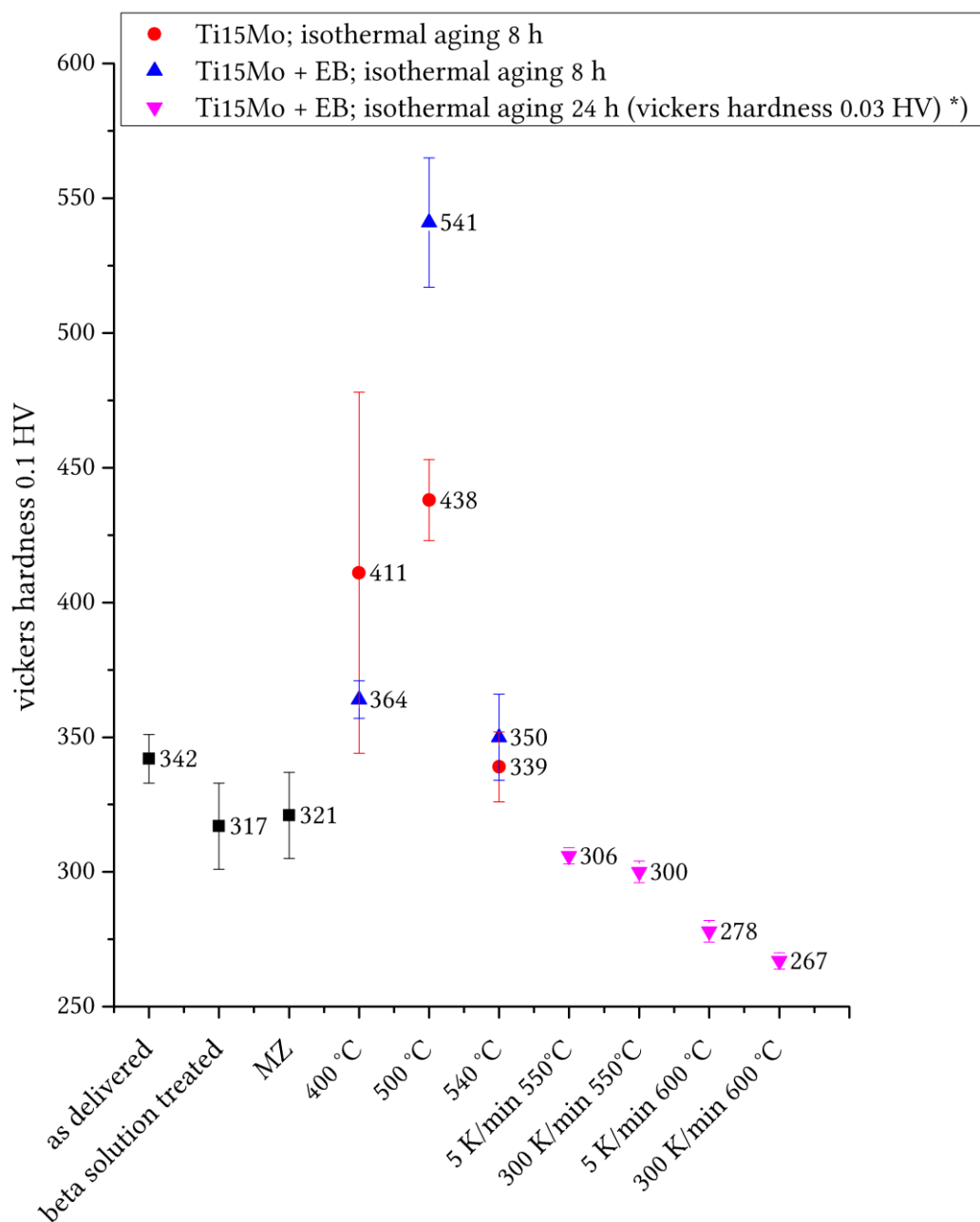


Figure 90. Vickers hardness measurement values for Ti15Mo and Ti15Mo+EB samples after 8 h and 24 h aging. (*) Values adapted from [94].

5.4 Surface structure after EB process for biomedical application

The analysis of the topography in titanium alloys can vary depending not only due to the method of surface modification (e.g. irregular, random or hierarchical surface pattern) but also about the technique of characterization (e.g. ISO standards for 2D and 3D, integral method or wavelets) [3], [51]. Ti alloys after EB structuring revealed a hierarchical multi-scale surface pattern. For example, the surface analysis of Ti15Mo, as shown in Figure 91, indicates an

overall statistical S_a value of $5.1 \mu\text{m}$ ($\lambda = 800 \mu\text{m}$). Meanwhile, the partial description of the groove shape revealed $\Delta z = 6.3 \mu\text{m}$ and $\Delta w = 107.7 \mu\text{m}$ for position 1, and $\Delta z = 2.4 \mu\text{m}$ and $\Delta w = 61.6 \mu\text{m}$ for position 2. This means that the analysis of hierarchical multi-scale topographies is not recommended by robust and stable height-descriptive parameters (e.g. S_a). Surface topography affects the biological response, and height-descriptive parameters can lead to misunderstandings about the real behaviour of biological entities on the surface of the implant material. A geometric description of aperiodic surfaces e.g. sandblasting and etching, is not possible. Therefore, Wennerberg et al. [3] proposed a combination of height-descriptive and geometric parameters for a better understanding.

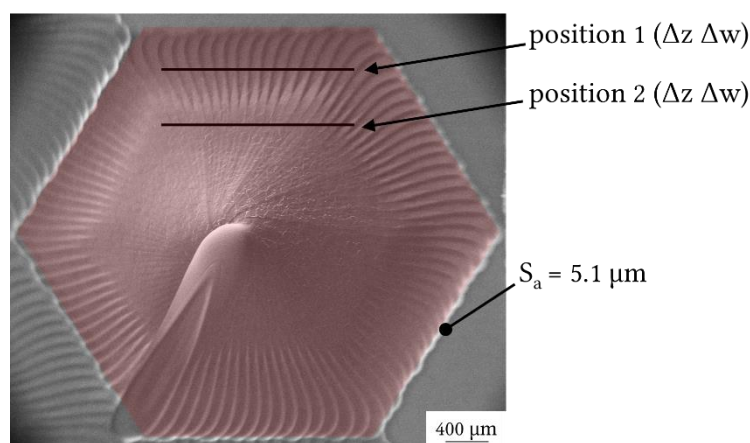


Figure 91. Surface roughness measurements for EB structured Ti15Mo pin array for 2.5 mA and $v = 697 \text{ mm/s}$.

Cellular and bacterial responses are highly variable to micro-structured and nano-structured topographies, and depend on the cell type as well as dimension, surface geometry and organization [116]. The schematic illustration in Figure 92 emphasizes the importance of multi-scale surface topographies. The transmucosal dental implant is in contact with soft tissue at gum level, in hard tissue at bone level and shows some risk of bacterial penetration. Not only the size and shape of the biological entities are different, but they also prefer different surface topographies. Therefore, bacteria preferentially adhere to a rough surface ($R_a > 0.2 \mu\text{m}$), while fibroblasts show adherence to a smooth surface and a sensitivity to contact guidance, with a groove dimension of 35 nm in depth and 100 nm in width. Osteoblastic cells, who are double the size compare to fibroblasts, preferentially adhere to rough surfaces [117], [118]. Ferraris et al. [119] proposed multi-scale topographies (micro - nanoscale roughness) to act at different biological levels. EB structuring enables multi-scale topographies, where the canal shape is related to the energy input, EB figure design and physical properties of the material.

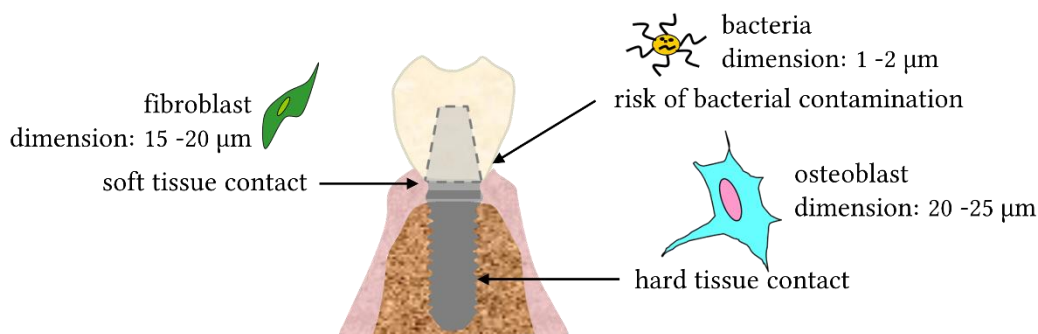


Figure 92. Schematic illustration of a) transmucosal dental implant with different biological entities on implant surface, b) bacteria, c) fibroblast and d) osteoblast. Adapted from [120].

The interlocking capacity is affected also by the surface roughness [121]. Mattila et al. [122] confirmed an increase of interlocking capacity with grooved polymer cylinders (groove depth of 500 μm) in comparison with a smooth surface with in vitro studies. This effect could be correlated to the structured figures obtained with pin height and wall depth, presented in Table 13.

5.5 Biological response on EB structured surfaces

The cell morphology observation of MC 3T3 E1 from 6 h to 48 h cultivation on cp TiGr2, Ti6Al4V and Ti15Mo with different EB structured surfaces revealed an optimum appearance of the cells with polygonal morphology and numerous cellular connections, in accordance with other studies of pre-osteoblastic cells MC 3T3 E1 and MG63 on rougher surfaces [123], [124]. In contrast to previous reports from Citeau et al. [125] and La Guehenec et al. [93], where MC 3T3 E1 cells after 48 h cultivation time were largely spread out (polygonal shape) and large cytoplasmic extensions of the cells appeared on mirror polished, $R_a = 0.17 \mu\text{m}$, Ti6Al4V samples. This was in comparison to surface treated samples with a roughness of between $R_a = 1.88 \mu\text{m}$ and $2.5 \mu\text{m}$. This decrease of the activity on the surface was mainly related to possible contamination during the coating by alumina [93] or biphasic calcium phosphate [93], [125] rather than the roughness produced by the process.

The incubation times up to 12 h did not show any significant effect of surface roughness on the cell spreading area, as shown in Figure 84. The measurements of cell spreading area suggested that the depth of the canal shape (Δz) had a significant influence on cell behaviour after 24 h of culture. There was not a significant increase of cell spreading area up to 24 h, similar to a previous study [47]. After 48 h of cultivation, an enhanced increase in cell spreading area was determined to be around 60 %, compared to 24 h, on a surface with a canal shape of $1.3 \mu\text{m}$. Chikarakara et al. [126] assumed an increase of viable cells, where the metabolic activity of NIH/3T3 fibroblast was increased after 24 h of culture with an average surface roughness between $R_a = 1.39 \mu\text{m}$ and $2.72 \mu\text{m}$. Moreover, EB structuring can be correlated with surface

structuring by laser-texturing [54], where defined grooves with a width between 25 μm and 50 μm on Ti6Al4V indicated the feasibility to control the cell alignment. The difference in methods and evaluations to describe the surface structure can vary, and therefore complicate the comparison of different surface structures [3], [52].

6 Conclusion

A novel surface structuring technique was applied by the EB technique to improve the interaction between the implant and biological environment of titanium alloys for orthopaedic devices. Furthermore, to gain an understanding of microstructural changes and to develop new biomaterials, additional microstructural investigations and heat treatments on a metastable β titanium were carried out.

The results led to the following conclusions:

- Electron beam bead on plate is in accordance to the electron beam welding process. Depth and width of the MZ increased by increasing the energy input. Minimal machine parameters on cp TiGr2, Ti6Al4V and Ti15Mo with fixed voltage of 150 kV were defined as 0.8 mA and 338 mm/s for velocity. Investigations with 0.8 mA showed the greatest deviation of the MZ due to fluctuations of the EB machine.
- Deflection figures to create EB structures were described by coordinate points and could be designed in a discretionary way for all investigated titanium alloys. The produced surface topography was influenced by the physical properties of the material, the deflection figure and the energy input of the EB.
- The structured surface for cp TiGr2, Ti6Al4V and Ti15Mo samples were free from cracks, pores and impurities. Therefore, EB structuring is a promising technique to produce reproducible hierarchical multi-scale surface topographies on titanium biomaterials. In this work, canal shapes were produced in the range of Δz of 1.1 μm to 4.9 μm for the depth and Δw of 78.5 μm to 113.1 μm for width of cp TiGr2, Δz of 1.3 μm to 9 μm for the depth and Δw of 68.6 μm to 119.7 μm for width of Ti6Al4V and Δz of 0.6 μm to 6.3 μm for the depth and Δw of 61.6 μm to 108 μm for width of Ti15Mo.
- The analysis of the hierarchical multi-scale surface roughness by geometric values was proposed, compared to the robust and stable height-descriptive parameters (e.g. Sa).
- The microstructure after EB structuring of cp TiGr2 consisted of columnar, coarse and plate like grains in the MZ, whereas elongated columnar grains were observed for Ti6Al4V and Ti15Mo. For Ti6Al4V, the microstructure in the MZ consist of martensitic α' as a result of rapid cooling. Additional heat treatments revealed a stabilization of the martensitic morphology in the MZ, thus decreasing the hardness. Investigations of Ti15Mo revealed a cellular dendritic substructure within the grain, whereby chemical heterogeneities (Mo content) appeared. Additional investigations of Ti15Mo and Ti15Mo+EB resulted in knowledge of phase transformations after continuous heating and additional isothermal treatment.
- MC3T3-E1 pre-osteoblastic cells demonstrated a polygonal morphology and spread out on the EB structured samples of all investigated Ti alloys after different cultivation time.

-
- An increase of cell spreading area up to 60 % after 48 h was found on EB structured samples with the lowest energy input (0.8 mA and 341 mm/s), compared to samples with higher energy input and control samples.

7 Outlook

In order to close this work, there are still some points open:

- The limitations of the beam focus and the deviation of the beam current when using 0.8 mA could be overcome by utilisation of parameters (e.g. working distance) and enhancement of the EB machine (e.g. decreasing the fluctuation of the beam current by changing the cathode / cathode system). Wherefore, a possible beam focus reduction and a more stable process for lower beam currents could be obtained.
- To gain a better understanding of the metastable condition in the HAZ of Ti6Al4V, first steps to simulate the HAZ by thermal treatments were carried out. Figure 93 (a) displays the HAZ after structuring of Ti6Al4V, and Figure 93 (b) the simulated HAZ by heat treatment. The simulated HAZ for Ti6Al4V was reached using a thermal cycle of heating up to 1200 °C with 659 K/s and quenching by helium gas after 1s of holding time. Further analysis of the microstructure would be needed to understand the effect of element partitioning during rapid treatment and additional heat treatments below T_{β} .

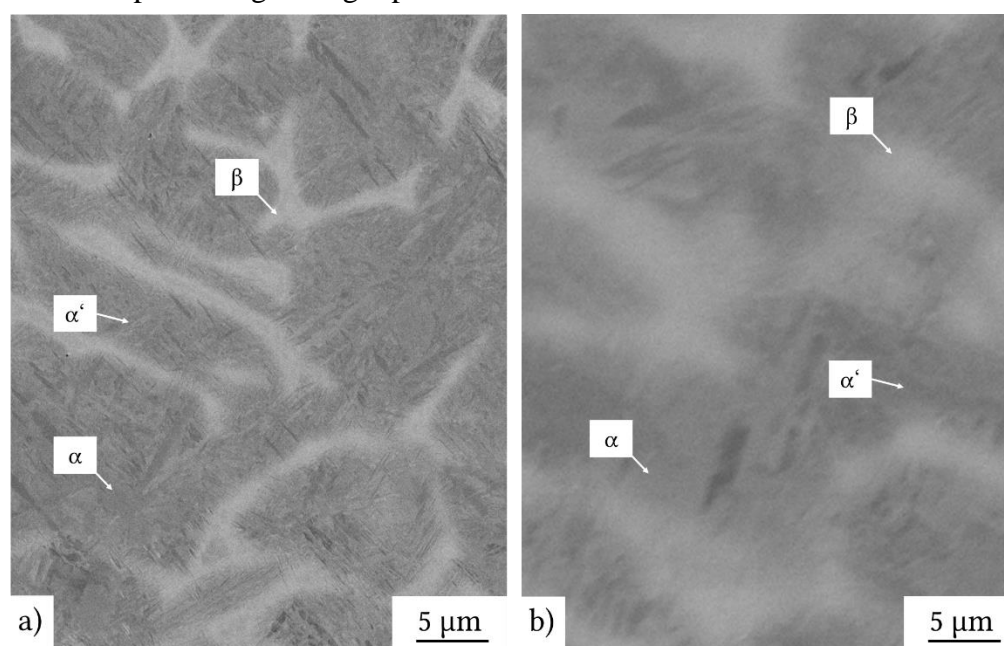


Figure 93. SEM BSE image of EB structured Ti6Al4V for a) HAZ and b) HAZ simulated by dilatometry.

- Further investigations should be carried out to understand the influence of heterogeneous chemical composition after EB structuring of Ti15Mo on the ω_{iso} and α phase formation. Therefore, investigations should be performed by in situ high energy diffraction synchrotron measurements during isothermal and continuous heating. These investigations can provide additional information by dilatometry and microscopy to understand the nucleation and formation of these phases, and their influence on the mechanical properties in this work.

- To clarify the influence of different surface structures on bone osteogenic genes, PrimePCR pathways were used. The gene expression results highlight the positive role of surface structure on murine pre-osteoblastic cells. However, studies need to be extended using different time points to develop a better insight into their specific roles. Figure 94 shows the relative expression of different genes of unstructured and structured surfaces.

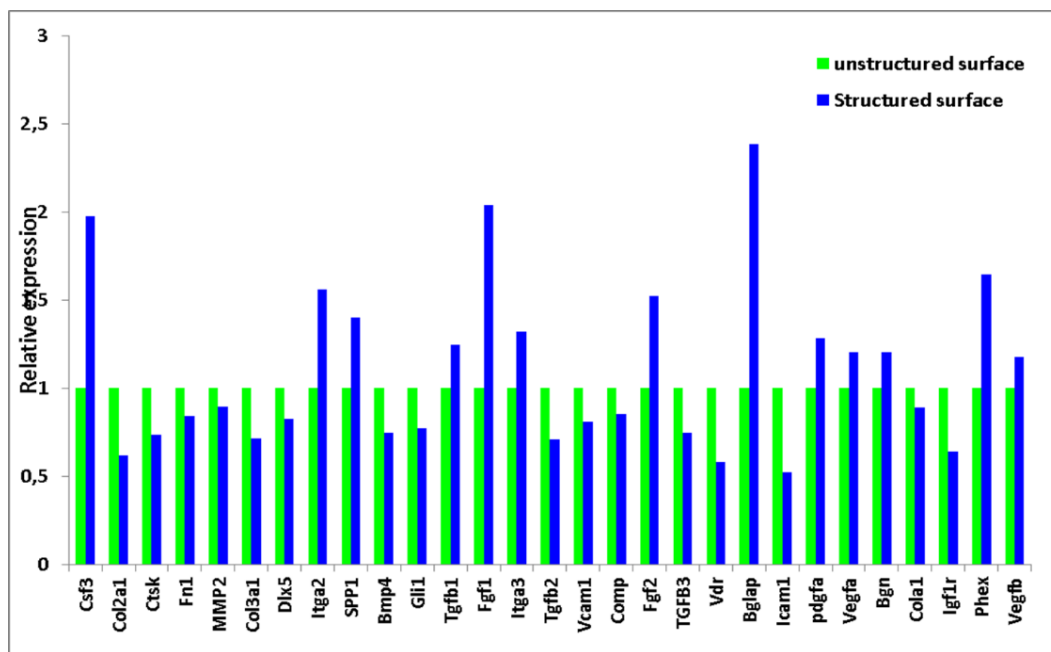


Figure 94. Relative gene expressions on unstructured and structured Ti6Al4V samples after 72h of cultivation time.

After the present work, some open questions and possibilities of research investigations include:

- Due to the fundamental bioinert character of titanium alloys, biopolymer composite coatings can improve the implant-tissue bonding, as well as incorporate biological entities for accelerated bone regeneration. Two different composite coatings, chitosan/n TiO₂ (bioactive glass) and chitosan/drug (Lysozyme), are already investigated in samples of Ti6Al4V with different patterns.
- The composite coating of chitosan / n TiO₂ by electrophoretic deposition showed the feasibility to maintain the 3D topography obtained by EB structuring, and was already published [50]. Further investigations should be carried out to obtain a bioactive surface by the use of different composites (e.g. polymer/bioglass or polymer/drug). These investigations were carried out in cooperation with Prof. Boccaccini, FAU Erlangen Germany in the framework of the KMM VIN network.
- Effect of nano/micro surface structure on bacteria and fibroblasts adhesion linear structuring on titanium alloys should be investigated. Preliminary results with cp TiGr2 showed the possibility to carry out line spacing from 5 µm by controlling the beam

velocity, due to the dwell time of the EB for each coordinate point X/Y (figure point). Figure 95 shows the top view for two different line spacings ($5\ \mu\text{m}$ and $30\ \mu\text{m}$). The very fine topography was used for further experiments with human primary fibroblasts (cytocompatibility and cell orientation) and bacteria adhesion (growth condition, adhesion evaluation and biofilm biomass viability). This work is in progress in cooperation with Prof. Spriano (DISAT Polito Italy) and has already been shown in different seminars/workshops [120], [127].

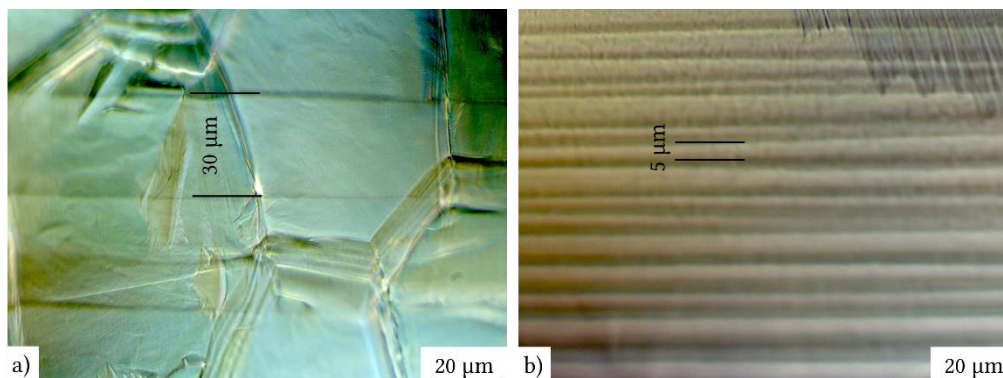


Figure 95. LOM image of EB line structuring on cp TiGr2 for a) line spacing of $30\ \mu\text{m}$ and b) line spacing of $5\ \mu\text{m}$.

8 Bibliography

- [1] S. Bauer, P. Schmuki, K. von der Mark, and J. Park, "Engineering biocompatible implant surfaces. Part I: Materials and surfaces," *Prog. Mater. Sci.*, vol. 58, no. 3, pp. 261–326, 2012.
- [2] T. S. Silva, D. C. Machado, C. Viezzer, A. N. Silva Junior, and M. G. Oliveira, "Effect of titanium surface roughness on human bone marrow cell proliferation and differentiation: an experimental study," *Acta Cir Bras*, vol. 24, no. 3, pp. 200–205, 2009.
- [3] A. Wennerberg and T. Albrektsson, "Effects of titanium surface topography on bone integration: A systematic review," *Clin. Oral Implants Res.*, vol. 20, no. SUPPL. 4, pp. 172–184, 2009.
- [4] D. F. Williams, *Definitions in biomaterials: proceeding of a consensus conference of the European Society for Biomaterials*, vol. volume 4. Chester: Elsevier Science Ltd, 1987.
- [5] M. Navarro, A. Michiardi, O. Castan, and J. A. Planell, "Biomaterials in orthopaedics," no. July, pp. 1137–1158, 2008.
- [6] B. D. Ratner, "A History of Biomaterials," in *Biomaterials Science: An Introduction to Materials: Third Edition*, ISBN 9780080877808, 2013, pp. xli–liii.
- [7] K. S. Katti, "Biomaterials in total joint replacement," *Colloids Surfaces B Biointerfaces*, vol. 39, no. 3, pp. 133–142, 2004.
- [8] A. S. Brydone, D. Meek, and S. Maclaine, "Proceedings of the Institution of Mechanical Engineers , Part H : Journal of Engineering in Medicine," 2010.
- [9] A. Sidky and R. E. Buckley, "Hardware removal after tibial fracture has healed," *Can. J. Surg.*, vol. 51, no. 4, pp. 263–268, 2008.
- [10] L. C. Jones, L. D. Timmie Topoleski, and A. K. Tsao, "Biomaterials in orthopaedic implants," in *Mechanical Testing of Orthopaedic Implants*, E. Friis, Ed. Elsevier Ltd., 2017, pp. 17–32.
- [11] S. Bose and A. Bandyopadhyay, "Introduction to Biomaterials," in *Characterization of Biomaterials*, A. Bandyopadhyay and S. Bose, Eds. Elsevier, 2013, pp. 1–9.
- [12] S. H. Teoh, "Fatigue of biomaterials: A review," *Int. J. Fatigue*, vol. 22, no. 10, pp. 825–837, 2000.
- [13] M. Geetha, A. K. Singh, R. Asokamani, and A. K. Gogia, "Ti based biomaterials, the ultimate choice for orthopaedic implants – A review," *Prog. Mater. Sci.*, vol. 54, no. 3, pp. 397–425, May 2009.
- [14] Q. Chen and G. A. Thouas, "Metallic implant biomaterials," *Mater. Sci. Eng. R Reports*, vol. 87, pp. 1–57, 2015.
- [15] R. Narayan, *ASM Handbook Volume 23 Materials for Medical Devices*, vol. 23. ASM International, 2012.
- [16] M. Niinomi, "Fatigue characteristics of metallic biomaterials," *Int. Journal of Fatigue*, vol. 29, pp. 992–1000, 2007.
- [17] R. Singh and N. B. Dahorte, "Corrosion degradation and prevention by surface modification of biometallic materials," *J. Mater. Sci. Mater. Med.*, pp. 725–751, 2007.
- [18] İ. Çelik, A. Alsarar, and G. Purcek, "Effect of different surface oxidation treatments on

- structural, mechanical and tribological properties of ultrafine-grained titanium,” *Surf. Coatings Technol.*, vol. 258, pp. 842–848, 2014.
- [19] N. Dalili, A. Edrissy, K. Farokhzadeh, J. Li, J. Lo, and A. R. Riahi, “Improving the wear resistance of Ti–6Al–4V/TiC composites through thermal oxidation (TO),” *Wear*, vol. 269, no. 7–8, pp. 590–601, 2010.
- [20] V. K. Balla, J. Soderlind, S. Bose, and A. Bandyopadhyay, “Microstructure, mechanical and wear properties of laser surface melted Ti6Al4V alloy,” *J. Mech. Behav. Biomed. Mater.*, vol. 32, pp. 335–344, 2014.
- [21] M. Niinomi, “Mechanical properties of biomedical titanium alloys,” *Mater. Sci. Eng. A*, vol. 243, no. 1–2, pp. 231–236, Mar. 1998.
- [22] M. Long and H. J. Rack, “Titanium alloys in total joint replacement--a materials science perspective.,” *Biomaterials*, vol. 19, no. 18, pp. 1621–39, Sep. 1998.
- [23] G. Lütjering and J. C. Williams, “Titanium: Engineering Materials and Processes,” in *Springer*, vol. second edi, 2007, pp. 1–442.
- [24] C. Leyens and M. Peters, *Titanium and Titanium Alloys Fundamentals and Application*. WILEY-VCH Verlag GmbH & Co, 2003.
- [25] P. Barriobero-Vila, “Phase transformation kinetics during continuous heating of $\alpha+\beta$ and metastable β titanium alloys,” *PhD Thesis TU Vienna Austria*, p. 2015, 2015.
- [26] ASTM International, “F2066-08: Standard specification for wrought titanium-15 molybdenum alloy for surgical implant applications (UNS R58150),” 2008.
- [27] B. Banerjee and P. Mukhopadhyay, *Phase Transformations Examples from Titanium and Zirconium Alloys*. Elsevier, 2007.
- [28] D. Banerjee and J. C. Williams, “Perspectives on titanium science and technology,” *Acta Mater.*, vol. 61, no. 3, pp. 844–879, 2013.
- [29] T. Ahmed and H. J. Rack, “Phase transformations during cooling in $\alpha+\beta$ titanium alloys,” *Mater. Sci. Eng. A*, vol. 243, no. 1–2, pp. 206–211, 1998.
- [30] M. S. Oh, J.-Y. Lee, and J. K. Park, “Continuous cooling β -to- α transformation behaviors of extra-pure and commercially pure Ti,” *Metall. Mater. Trans. A*, vol. 35, no. 10, pp. 3071–3077, 2004.
- [31] M. J. Blackburn and J. C. Williams, “Phase Transformations in Ti:Mo and Ti:V Alloys,” *Trans. Metall. Soc. AIME*, vol. 2461, p. 2461, 1968.
- [32] R. Yi, H. Liu, D. Yi, W. Wan, B. Wang, Y. Jiang, Q. Yang, D. Wang, Q. Gao, Y. Xu, and Q. Tang, “Precipitation hardening and microstructure evolution of the Ti-7Nb-10Mo alloy during aging,” *Mater. Sci. Eng. C*, vol. 63, pp. 577–586, 2016.
- [33] A. Settefrati, E. Aeby-Gautier, M. Dehmas, G. Geandier, B. Appolaire, S. Audion, and J. Delfosse, “Precipitation in a near Beta Titanium Alloy on Ageing: Influence of Heating Rate and Chemical Composition of the Beta-Metastable Phase,” *Solid State Phenom.*, vol. 172–174, no. June 2011, pp. 760–765, 2011.
- [34] Y. Ohmori, T. Ogo, K. Nakai, and S. Kobayashi, “Effects of omega-phase precipitation on beta--> alpha, alpha’ transformations in a metastable beta titanium alloy,” *Mater. Sci. Eng. A*, vol. 312, no. 1–2, pp. 182–188, 2001.
- [35] F. Prima, P. Vermaut, G. Texier, D. Ansel, and T. Gloriant, “Evidence of alpha-nanophase heterogeneous nucleation from omega particles in a beta-metastable Ti-based

- alloy by high-resolution electron microscopy,” *Scr. Mater.*, vol. 54, no. 4 SPEC. ISS., pp. 645–648, 2006.
- [36] S. Azimzadeh and H. J. Rack, “Phase transformations in Ti-6.8Mo-4.5Fe-1.5Al,” *Metall. Mater. Trans. A*, vol. 29, no. 10, pp. 2455–2467, 1998.
- [37] J. D. C. Teixeira, B. Appolaire, E. Aeby-Gautier, S. Denis, G. Cailletaud, and N. Späth, “Transformation kinetics and microstructures of Ti17 titanium alloy during continuous cooling,” *Mater. Sci. Eng. A*, vol. 448, no. 1–2, pp. 135–145, 2007.
- [38] L. J. Raggatt and N. C. Partridge, “Cellular and molecular mechanisms of bone remodeling,” *J. Biol. Chem.*, vol. 285, no. 33, pp. 25103–25108, 2010.
- [39] A. Schindeler, M. M. McDonald, P. Bokko, and D. G. Little, “Bone remodeling during fracture repair: The cellular picture,” *Semin. Cell Dev. Biol.*, vol. 19, no. 5, pp. 459–466, 2008.
- [40] M. Doblaré, J. M. García, and M. J. Gómez, “Modelling bone tissue fracture and healing: A review,” *Eng. Fract. Mech.*, vol. 71, no. 13–14, pp. 1809–1840, 2004.
- [41] R. Bosco, J. Van Den Beucken, S. Leeuwenburgh, and J. Jansen, “Surface Engineering for Bone Implants: A Trend from Passive to Active Surfaces,” *Coatings*, vol. 2, no. 4, pp. 95–119, 2012.
- [42] E. Wintermantel and S.-W. Ha, *Medizintechnik Life Science Engineering*. Springer Verlag Berlin Heidelberg, 2009.
- [43] M. H. Fathi and A. Doost Mohammadi, “Preparation and characterization of sol-gel bioactive glass coating for improvement of biocompatibility of human body implant,” *Mater. Sci. Eng. A*, vol. 474, no. 1–2, pp. 128–133, 2008.
- [44] Q. Chen, Y. Liu, Q. Q. Yao, S. S. Yu, K. Zheng, M. Pischetsrieder, and A. R. Boccaccini, “Multilayer bioactive composite coatings with drug delivery capability by electrophoretic deposition combined with layer-by-layer deposition,” *Adv. Biomater. Devices Med. I*, pp. 18–27, 2014.
- [45] F. Mussano, T. Genova, E. Verga Falzacappa, P. Scopece, L. Munaron, P. Rivolo, P. Mandracci, A. Benedetti, S. Carossa, and A. Patelli, “In vitro characterization of two different atmospheric plasma jet chemical functionalizations of titanium surfaces,” *Appl. Surf. Sci.*, vol. 409, pp. 314–324, 2017.
- [46] M. Bächle and R. J. Kohal, “A systematic review of the influence of different titanium surfaces on proliferation, differentiation and protein synthesis of osteoblast-like MG63 cells,” *Clin. Oral Implants Res.*, vol. 15, no. 6, pp. 683–692, 2004.
- [47] J. Havlikova, J. Strasky, M. Vandrovцова, P. Hrcuba, M. Mhaede, M. Janecek, and L. Bacakova, “Innovative surface modification of Ti-6Al-4V alloy with a positive effect on osteoblast proliferation and fatigue performance,” *Mater. Sci. Eng. C. Mater. Biol. Appl.*, vol. 39, pp. 371–9, Jun. 2014.
- [48] O. Raimbault, S. Benayoun, K. Anselme, C. Mauclair, T. Bourgade, A. M. Kietzig, P. L. Girard-Lauriault, S. Valette, and C. Donnet, “The effects of femtosecond laser-textured Ti-6Al-4V on wettability and cell response,” *Mater. Sci. Eng. C*, vol. 69, pp. 311–320, 2016.
- [49] E. Gilabert-Chirivella, R. Pérez-Feito, C. Ribeiro, S. Ribeiro, D. M. Correia, M. L. González-Martín, J. M. Manero, S. Lanceros-Méndez, G. G. Ferrer, and J. L. Gómez-Ribelles, “Chitosan patterning on titanium implants,” *Prog. Org. Coatings*, vol. 111, no.

- October, pp. 23–28, 2017.
- [50] C. Ramskogler, L. Cordero, F. Warchomicka, A. R. Boccaccini, and C. Sommitsch, “Biocompatible Ceramic-Biopolymer Coatings Obtained by Electrophoretic Deposition on Electron Beam Structured Titanium Alloy Surfaces,” *Mater. Sci. Forum*, vol. 879, pp. 1552–1557, 2016.
- [51] L. De Chiffre, P. Lonardo, H. Trumpold, D. a. Lucca, G. Goch, C. a. Brown, J. Raja, and H. N. Hansen, “Quantitative Characterisation of Surface Texture,” *CIRP Ann. - Manuf. Technol.*, vol. 49, no. 2, pp. 635–652, 2000.
- [52] R. J. Crawford, H. K. Webb, V. K. Truong, J. Hasan, and E. P. Ivanova, “Surface topographical factors influencing bacterial attachment,” *Adv. Colloid Interface Sci.*, vol. 179–182, pp. 142–149, 2012.
- [53] C. Ramskogler, F. Warchomicka, S. Mostofi, A. Weinberg, and C. Sommitsch, “Innovative surface modification of Ti6Al4V alloy by electron beam technique for biomedical application,” *Mater. Sci. Eng. C*, vol. 78, pp. 105–113, 2017.
- [54] O. Raimbault, S. Benayoun, K. Anselme, C. Mauclair, T. Bourgade, A. M. Kietzig, P. L. Girard-Lauriault, S. Valette, and C. Donnet, “The effects of femtosecond laser-textured Ti-6Al-4V on wettability and cell response,” *Mater. Sci. Eng. C*, vol. 69, pp. 311–320, 2016.
- [55] B. Vrancken, “Study of Residual Stresses in Selective Laser Melting,” *PhD Thesis; KU Leuven Arenb. Dr. Sch. Fac. Eng. Sci.*, no. June, pp. 1–253, 2016.
- [56] V. Adam, U. Clauß, D. v. Dobeneck, K. Thomas, and T. Löwer, *Elektronenstrahlschweißen Grundlagen einer faszinierenden Technik*, Pro-Beam A. .
- [57] Schultz, *Electron beam welding*. Abington Publishing Cambridge England, 2004.
- [58] B. G. I. Dance and A. Buxton, “An Introductuion to Surfı-Sculpt Technology - New Opportunities, New Challenges,” in *In Proceedings of the 7th International Conference on Beam Technology*, 2007, pp. 75–84.
- [59] M. Ziolkowski and H. Brauer, “Modelling of Seebeck effect in electron beam deep welding of dissimilar metals,” *COMPEL Int. J. Comput. Math. Electr. Electron. Eng.*, vol. 28, no. 1, pp. 140–153, 2009.
- [60] M. Stütz, “Master Thesis; Surface Structuring of Biodegradable Mg-alloys by Electron Beam Technique,” *Master Thesis, IMAT TU Graz, Austria*, no. September, 2014.
- [61] C. Earl, P. Hilton, and B. O’Neill, “Parameter Influence on Surfı-Sculpt Processing Efficiency,” *Phys. Procedia*, vol. 39, pp. 327–335, 2012.
- [62] J. Blackburn and P. Hilton, “Producing surface features with a 200 W Yb-fibre laser and the Surfı-Sculpt® process,” *Phys. Procedia*, vol. 12, no. PART 1, pp. 529–536, 2011.
- [63] X. Wang, J. Ahn, Q. Bai, W. Lu, and J. Lin, “Effect of forming parameters on electron beam Surfı-Sculpt protrusion for Ti-6Al-4V,” *Mater. Des.*, vol. 76, pp. 202–206, 2015.
- [64] J. Taendl and N. Enzinger, “Electron beam surface structuring of AA6016 aluminium alloy,” *Weld. World*, 2014.
- [65] T. DebRoy, H. L. Wei, J. S. Zuback, T. Mukherjee, J. W. Elmer, J. O. Milewski, A. M. Beese, A. Wilson-Heid, A. De, and W. Zhang, “Additive manufacturing of metallic components – Process, structure and properties,” *Prog. Mater. Sci.*, vol. 92, pp. 112–224, 2018.

- [66] G. Schulze, *Die Metallurgie des Schweißens Eisenwerkstoffe - Nichteisenmetallische Werkstoffe*. 2010.
- [67] G. J. Davies and J. G. Garland, "Solidification Structures and Properties of Fusion Welds," *Int. Mater. Rev.*, vol. 20, no. 1, pp. 83–108, 1975.
- [68] S. A. David, S. S. Babu, and J. M. Vitek, "Welding : Solidification and Microstructure," *JOM*, no. June, 2003.
- [69] F. Karimzadeh, M. Heidarbeigy, and A. Saatchi, "Effect of heat treatment on corrosion behavior of Ti-6Al-4V alloy weldments," *J. Mater. Process. Technol.*, vol. 206, no. 1–3, pp. 388–394, 2008.
- [70] C. J. Tsai and L. M. Wang, "Improved mechanical properties of Ti-6Al-4V alloy by electron beam welding process plus annealing treatments and its microstructural evolution," *Mater. Des.*, vol. 60, pp. 587–598, 2014.
- [71] S. S. Al-Bermani, M. L. Blackmore, W. Zhang, and I. Todd, "The origin of microstructural diversity, texture, and mechanical properties in electron beam melted Ti-6Al-4V," *Metall. Mater. Trans. A Phys. Metall. Mater. Sci.*, vol. 41, no. 13, pp. 3422–3434, 2010.
- [72] M. Wu, R. Xin, Y. Wang, Y. Zhou, K. Wang, and Q. Liu, "Microstructure , texture and mechanical properties of commercial high- purity thick titanium plates jointed by electron beam welding," *Mater. Sci. Eng. A*, vol. 677, pp. 50–57, 2016.
- [73] E. Akman, A. Demir, T. Canel, and T. Sinmazc, "Laser welding of Ti6Al4V titanium alloys," *J. Mater. Process. Technol.*, vol. 9, pp. 3705–3713, 2009.
- [74] H. Schwab, F. Palm, U. Kühn, and J. Eckert, "Microstructure and mechanical properties of the near-beta titanium alloy Ti-5553 processed by selective laser melting," *Mater. Des.*, vol. 105, pp. 75–80, 2016.
- [75] K. Yamanaka, W. Saito, M. Mori, H. Matsumoto, and A. Chiba, "Preparation of weak-textured commercially pure titanium by electron beam melting," *Addit. Manuf.*, vol. 8, pp. 105–109, 2015.
- [76] T. Vilaro, C. Colin, and J. D. Bartout, "As-Fabricated and Heat-Treated Microstructures of the Ti-6Al-4V Alloy Processed by Selective Laser Melting," *Metall. Mater. Trans. A*, vol. 42A, pp. 3190–3199, 2011.
- [77] I. Yadroitsev, P. Krakhmalev, and I. Yadroitsava, "Selective laser melting of Ti6Al4V alloy for biomedical applications: Temperature monitoring and microstructural evolution," *J. Alloys Compd.*, vol. 583, pp. 404–409, 2014.
- [78] B. Vrancken, L. Thijs, J. P. Kruth, and J. Van Humbeeck, "Microstructure and mechanical properties of a novel β titanium metallic composite by selective laser melting," *Acta Mater.*, vol. 68, pp. 150–158, 2014.
- [79] H. Attar, S. Ehtemam-Haghighi, D. Kent, X. Wu, and M. S. Dargusch, "Comparative study of commercially pure titanium produced by laser engineered net shaping, selective laser melting and casting processes," *Mater. Sci. Eng. A*, vol. 705, no. August, pp. 385–393, 2017.
- [80] D. Gu, Y. C. Hagedorn, W. Meiners, G. Meng, R. J. S. Batista, K. Wissenbach, and R. Poprawe, "Densification behavior, microstructure evolution, and wear performance of selective laser melting processed commercially pure titanium," *Acta Mater.*, vol. 60, no. 9, pp. 3849–3860, 2012.

- [81] K. G. Prashanth and J. Eckert, "Formation of metastable cellular microstructures in selective laser melted alloys," *J. Alloys Compd.*, vol. 707, pp. 27–34, 2017.
- [82] "Certificate Report TiGr2 by Baoji Titanium Industry Co," *G, Provid. by Co. Hempel Co Erze und Met.*, 2013.
- [83] E. C. Rodney Boyer, Gerhard Welsch, *Materials Properties Handbook Titanium Alloys*, ISBN-13:97. ASM International, 2007.
- [84] M. P. Christoph Leyens, *Titanium and Titanium Alloys Fundamentals and Applications*. WILEY-VCH Verlag GmbH & Co, 2003.
- [85] K. Adamus, Z. Kucharczyk, K. Wojsyk, and K. Kudla, "Numerical analysis of electron beam welding of different grade titanium," *Comput. Mater. Sci.*, vol. 77, pp. 286–294, 2013.
- [86] "Certificate Report, VSMOP-AVISMA Corporation, Heatnumber: 8-33-5303," *Provid. by Böhler Schmiedetechnik GmbH Co KG*, 2008.
- [87] "Inspection Certificate of Quality Western Superconducting Technologies Co., LTD," *G, Provid. by Co. Hempel Co Erze und Met.*, 2013.
- [88] "ATI Technical Data Sheet: ATI 15Mo Titanium Alloy," 2014.
- [89] "<https://www.makeitfrom.com/material-properties/UNS-R58150-Titanium-Ti-15Mo/>, 02.11, 2017. .
- [90] J. Disegi, "Implant Materials, Wrought Titanium 15% Molydenum," 2009.
- [91] G. S. H. J. Bargel, *Werkstoffkunde*. Berlin: Springer, 2005.
- [92] A. Citeau, J. Guicheux, C. Vinatier, P. Layrolle, T. P. Nguyen, P. Pilet, and G. Daculsi, "In vitro biological effects of titanium rough surface obtained by calcium phosphate grid blasting," *Biomaterials*, vol. 26, no. 2, pp. 157–165, 2005.
- [93] L. Le Guehenec, M.-A. Lopez-Heredia, B. Enkel, P. Weiss, Y. Amouriq, and P. Layrolle, "Osteoblastic cell behaviour on different titanium implant surfaces.," *Acta Biomater.*, vol. 4, no. 3, pp. 535–43, May 2008.
- [94] M. Gabernig, "Surface structuring and microstructure development of a metastable beta-titanium alloy for biomedical application prepared by an electron-beam technique," *Master Thesis, IMAT TU Graz, Austria*, no. June, 2016.
- [95] S. Nag, R. Banerjee, R. Srinivasan, J. Y. Hwang, M. Harper, and H. L. Fraser, "Omega-Assisted nucleation and growth of alpha precipitates in the Ti-5Al-5Mo-5V-3Cr-0.5Fe beta titanium alloy," *Acta Mater.*, vol. 57, no. 7, pp. 2136–2147, 2009.
- [96] B. K. C. Ganesh, W. Sha, N. Ramanaiah, and a. Krishnaiah, "Effect of shotpeening on sliding wear and tensile behavior of titanium implant alloys," *Mater. Des.*, vol. 56, pp. 480–486, 2014.
- [97] S. Bauer, P. Schmuki, K. von der Mark, and J. Park, "Engineering biocompatible implant Part I: Materials and surfaces," *Prog. Mater. Sci.*, vol. 58, no. 3, pp. 261–326, Apr. 2013.
- [98] R. Palanivel, I. Dinaharan, and R. F. Laubscher, "Microstructure evolution and mechanical characterization of Nd:YAG laser beam welded titanium tubes," *Mater. Charact.*, vol. 134, no. September, pp. 225–235, 2017.
- [99] H. Liu, K. Nakata, J. X. Zhang, N. Yamamoto, and J. Liao, "Microstructural evolution of fusion zone in laser beam welds of pure titanium," *Mater. Charact.*, vol. 65, pp. 1–7,

- 2012.
- [100] B. Vrancken, L. Thijs, J. Kruth, and J. Van Humbeeck, "Heat treatment of Ti6Al4V produced by Selective Laser Melting: Microstructure and mechanical properties," *J. Alloys Compd.*, vol. 541, pp. 177–185, 2012.
- [101] P. A. Kobryn and S. L. Semiatin, "Microstructure and texture evolution during solidification processing of Ti–6Al–4V," *J. Mater. Process. Technol.*, vol. 135, pp. 330–339, 2003.
- [102] L. Qian, J. Mei, J. Liang, and X. Wu, "Influence of position and laser power on thermal history and microstructure of direct laser fabricated Ti–6Al–4V samples," *Mater. Sci. Technol.*, vol. 21, no. 5, pp. 597–605, 2005.
- [103] W. Lu, Y. Shi, Y. Lei, and X. Li, "Effect of electron beam welding on the microstructures and mechanical properties of thick TC4-DT alloy," *Mater. Des.*, vol. 34, pp. 509–515, 2012.
- [104] L. Thijs, F. Verhaeghe, T. Craeghs, J. Van Humbeeck, and J. P. Kruth, "A study of the microstructural evolution during selective laser melting of Ti–6Al–4V," *Acta Mater.*, vol. 58, no. 9, pp. 3303–3312, 2010.
- [105] L. Thijs, F. Verhaeghe, T. Craeghs, J. Van Humbeeck, and J. Kruth, "A study of the microstructural evolution during selective laser melting of Ti – 6Al – 4V," *Acta Mater.*, vol. 58, no. 9, pp. 3303–3312, 2010.
- [106] Y. Han, W. Lu, T. Jarvis, J. Shurvinton, and X. Wu, "Investigation on the Microstructure of Direct Laser Additive Manufactured Ti6Al4V Alloy," *Mater. Res.*, vol. 18, pp. 24–28, 2015.
- [107] L. Thijs, K. Kempen, J. P. Kruth, and J. Van Humbeeck, "Fine-structured aluminium products with controllable texture by selective laser melting of pre-alloyed AlSi10Mg powder," *Acta Mater.*, vol. 61, no. 5, pp. 1809–1819, 2013.
- [108] D. A. Hughes and N. Hansen, "High angle boundaries formed by grain subdivision mechanisms," *Acta Mater.*, vol. 45, no. 9, pp. 3871–3886, 1997.
- [109] P. Barriobero-Vila, G. Requena, F. Warchomicka, A. Stark, N. Schell, and T. Buslaps, "Phase transformation kinetics during continuous heating of a β -quenched Ti–10V–2Fe–3Al alloy," *J. Mater. Sci.*, vol. 50, no. 3, pp. 1412–1426, 2015.
- [110] P. Zháňal, P. Hrcuba, M. Hájek, B. Smola, J. Stráský, J. Šmilauerová, J. Veselý, and M. Janeček, "Evolution of ω phase during heating of metastable β titanium alloy Ti–15Mo," *J. Mater. Sci.*, vol. 53, no. 1, pp. 837–845, 2018.
- [111] W.-F. Ho, "Effect of omega phase on mechanical properties of Ti-15Mo alloys for biomedical applications," *J. Med. Biol. Eng.*, vol. 28, pp. 47–51.
- [112] W. Wan, H. Liu, Y. Jiang, D. Yi, R. Yi, Q. Gao, D. Wang, and Q. Yang, "Microstructure characterization and property tailoring of a biomedical Ti-19Nb-1.5Mo-4Zr-8Sn alloy," *Mater. Sci. Eng. A*, vol. 637, pp. 130–138, 2015.
- [113] D. Kent, G. Wang, W. Wang, and M. S. Dargusch, "Influence of ageing temperature and heating rate on the properties and microstructure of beta Ti alloy, Ti-6Cr-5Mo-5V-4Al," *Mater. Sci. Eng. A*, vol. 531, pp. 98–106, 2012.
- [114] S. Azimzadeh and H. J. Rack, "Phase Transformations in Ti-6.8Mo-4.5Fe-1.5Al," vol. 29, no. October, pp. 2455–2467, 1998.

- [115] C.-L. Li, X.-J. Mi, W. Ye, S.-X. Hui, D.-G. Lee, and Y.-T. Lee, "Microstructural evolution and age hardening behavior of a new metastable beta Ti-2Al-9.2Mo-2Fe alloy," *Mater. Sci. Eng. A*, vol. 645, pp. 225–231, 2015.
- [116] S. A. Skoog, "In vitro biocompatibility assessment of microstructured and nanostructured surfaces for medical device applications," *PhD Thesis Raleigh North Carolina USA*, 2015.
- [117] D. M. Brunette, P. Tengvall, M. Textor, and P. Thomsen, *Titanium in Medicine*, vol. 216, no. 3. Springer-Verlag Berlin Heidelberg GmbH, 2002.
- [118] S. Ferraris, F. Truffa Giachet, M. Miola, E. Bertone, A. Varesano, C. Vineis, A. Cochis, R. Sorrentino, L. Rimondini, and S. Spriano, "Nanogrooves and keratin nanofibers on titanium surfaces aimed at driving gingival fibroblasts alignment and proliferation without increasing bacterial adhesion," *Mater. Sci. Eng. C*, vol. 76, pp. 1–12, 2017.
- [119] S. Ferraris, A. Bobbio, M. Miola, and S. Spriano, "Surface & Coatings Technology Micro- and nano-textured , hydrophilic and bioactive titanium dental implants," *Surf. Coat. Technol.*, vol. 276, pp. 374–383, 2015.
- [120] S. Ferraris, F. Truffa Giachet, A. Varesano, C. Vineis, A. Cochis, R. Sorrentino, V. Guarino, I. C. Maya, L. Ambrosio, F. G. Warchomicka, C. Ramskogler, L. Rimondini, and S. Spriano, "Controlling soft tissue adhesion on titanium surfaces by nanogrooves and keratin nanofibres," in *Presentation "Congresso nazionale Societa Italiana Biomateriali SIB,"* 2017.
- [121] J. Fu, Y. Hu, Z. Guo, Y. Zhang, Y. Hao, and S. Li, "Effect of surface micro-topography of titanium material on the behaviors of rabbit osteoblast in vitro," *Appl. Surf. Sci.*, vol. 255, no. 2, pp. 286–289, Nov. 2008.
- [122] R. H. Mattila, M. a. Puska, L. V. J. Lassila, and P. K. Vallittu, "Fibre-reinforced composite implant: in vitro mechanical interlocking with bone model material and residual monomer analysis," *J. Mater. Sci.*, vol. 41, no. 13, pp. 4321–4326, Apr. 2006.
- [123] K. Anselme, P. Linez, M. Bigerelle, D. Le Maguer, A. Le Maguer, P. Hardouin, H. F. Hildebrand, A. Iost, and J. M. Leroy, "The relative influence of the topography and chemistry of TiAl6V4 surfaces on osteoblastic cell behaviour," *Biomaterials*, vol. 21, no. 15, pp. 1567–1577, 2000.
- [124] B. D. Kieswetter, K., Schwartz, Z., Hummert, T. W., Dochran, D. L., Simpson, J., Dean, D. D., Boyan, "Surface roughness modulates the local production of growth factors and cytokines by osteoblast-like MG-63 cells," *J. Biomech. Mater. Reseach*, vol. 32, pp. 55–63, 1996.
- [125] A. Citeau, J. Guicheux, C. Vinatier, P. Layrolle, T. P. Nguyen, P. Pilet, and G. Daculsi, "In vitro biological effects of titanium rough surface obtained by calcium phosphate grid blasting," *Biomaterials*, vol. 26, no. 2, pp. 157–65, Jan. 2005.
- [126] E. Chikarakara, P. Fitzpatrick, E. Moore, T. Levingstone, L. Grehan, C. Higginbotham, M. Vázquez, K. Bagga, S. Naher, and D. Brabazon, "In vitro fibroblast and pre-osteoblastic cellular responses on laser surface modified Ti-6Al-4V.," *Biomed. Mater.*, vol. 10, 2015.
- [127] S. Spriano, S. S. Ferraris, C. C. Vineis, A. A. Varesano, A. A. Cochis, and L. L. Rimondini, "Surface modifications at the nanoscale for a better integration of titanium implants to the hard and soft tissues," *7th KMM-VIN Ind. Work. Biomater. key Technol. better Heal. Erlangen, Ger.*, pp. 2–3, 2017.

„...alles Weitere im nächsten Leben dann...“

Fernando Warchomicka 2017